Multi-wavelength Observations of Pulsar Wind Nebulae and Composite Supernova Remnants

A THESIS

SUBMITTED TO THE FACULTY OF THE GRADUATE SCHOOL

OF THE UNIVERSITY OF MINNESOTA

BY

Tea Temim

IN PARTIAL FULFILLMENT OF THE REQUIREMENTS

FOR THE DEGREE OF

DOCTOR OF PHILOSOPHY

Charles E. Woodward and Robert D. Gehrz, Advisor

September 2009

Acknowledgements

I would most of all like to thank my family for making this thesis possible. I couldn't have done any of this without the love and support of my parents, Akaid and Ana Temim, and my sister Maja. I also thank my friends in Minneapolis and Boston for keeping me sane during this time. I thank George for years of support and patience, and Mladen for being there and encouraging me during the last year.

This thesis would also not be possible without my CfA thesis advisor, Pat Slane, who has been extremely supportive and who provided encouragement and mentorship during the last two years, and my advisors Chick Woodward and Bob Gehrz who offered guidance and introduced me to astronomy research in the first place. I would also like to thank my collaborators, in particular Larry Rudnick, John Raymond, Steve Reynolds, and Kazik Borkowski, the members of my predoctoral research review committee, my thesis defense committee, and especially my friends in the IR lab (Martha, Mike, Andrew, Dale, and Gerry), and my fellow graduate students and astronomy faculty in Minnesota. I would not be where I am today without their support.

This thesis is dedicated to my parents and to the memory of my uncle, Ahzur Temim, a brilliant thinker and innovator who has been an inspiration since I've been young.

Za mamu i tatu... i adzu Ahzura.

Multi-wavelength Observations of Pulsar Wind Nebulae and Composite Supernova Remnants

by Tea Temim

Under the supervision of Charles E. Woodward and Robert D. Gehrz at the University of Minnesota, and Patrick O. Slane at the Harvard-Smithsonian Center for Astrophysics

ABSTRACT

Multi-wavelength studies of pulsar wind nebulae (PWNe) and supernova remnants (SNRs) lead to a better understanding of their evolutionary development, the interaction of supernovae (SNe) and pulsar winds with their surroundings, and nucleosynthesis and production and processing of dust grains by SNe. PWNe and composite supernova remnants, in particular, are unique laboratories for the study of the energetic pulsar winds, particle injection processes, and the impact of PWNe on the evolving SNR. They provide information on SNR shock properties, densities and temperatures, and the chemical composition and the ionization state of the material ejected by SNe. SNRs also serve as laboratories for the study of dust production and processing in SNe. While X-ray observations yield important information about the SN progenitor, hot gas properties, SN explosion energy, and the surrounding interstellar medium (ISM), the IR can provide crucial information about the faint non-thermal emission, continuum emission from dust, and forbidden line emission from SN ejecta. Combining observations at a wide range of wavelengths provides a more complete picture of the SNR development and helps better constrain current models describing a SNR's evolution and its impact on the surrounding medium. This thesis focuses on a multi-wavelength study of

PWNe in various stages of their evolution and investigates their interaction with the expanding SN ejecta and dust and the SNR reverse shock. The study of these interactions can provide important information on the SNR properties that may otherwise be unobservable.

The work in this thesis has been carried out under the supervision of Patrick Slane at the Harvard-Smithsonian Center for Astrophysics, and Charles E. Woodward and Rebert D. Gehrz at the University of Minnesota. The first part of the thesis summarizes the evolution and observational properties of SNRs and PWNe, with a focus on the evolution of young PWNe that are sweeping up inner SN ejecta. Two cases studies of such systems are discussed; infrared observations of the Crab Nebula; and X-ray and IR observations of G54.1+0.3. The second part of the thesis concentrates on the late stages of PWN evolution in which the PWN interacts with the SNR reverse shock. The final case study describes the X-ray observations of G327.1-1.1, a composite SNR in a late stage of its evolution. The thesis concludes with a summary of the results and proposed future work.

Table of Contents

List of Tables

List of Figures

Chapter 1

Supernova Remnants and Pulsar Wind Nebulae

1.1 Introduction

SN explosions are among the most energetic events in the universe, releasing approximately 10^{51} erg of energy into the ISM. They significantly affect the distribution of gas and dust in the Galaxy, the chemical content of the ISM, and can even trigger star formation in the disturbed interstellar clouds. Heavy elements are produced by rapid neutron capture in the expanding ejecta. These ejecta eventually merge with the ISM and enrich the chemical content of the interstellar clouds from which new stars continually form. SNe results from two different types of explosion mechanisms; an explosion resulting from the deflegration or detonation of a carbon-oxygen white dwarf as it accretes mass from a companion and approaches the Chandrasekhar mass limit; or from the collapse of iron cores of massive stars with masses above $\sim 8\ M_{\odot}$. The former type of SN explosions are referred to as Type Ia SNe and their released energy originates from the burning of carbon and oxygen into iron an nickel. The energy released from core-collapse SNe is gravitational energy liberated in the collapse, and these explosions

can be classified as Type II, Ib, or Ic. The classification of SNe is purely observational is based on their lightcurves and optical spectra. The main difference between Type I and Type II SNe is the presence of hydrogen absorption in their spectra; Type I SNe do not show hydrogen lines, while Type II SNe do show evidence for hydrogen. The lack of hydrogen in Type Ib and Ic spectra is likely due to the loss of the hydrogen envelopes through stellar winds of massive stars (Harkness & Wheeler 1990).

This thesis focuses on core-collapse SN explosions from massive stars. When the core of the star collapses, the outer layers are blown off into space, producing a SNR. One of the main distinctions between the SNRs of core-collaps and Type Ia SNe are their different chemical abundances. SNRs produced by the collapse of massive stars typically show a large oxygen abundance, while Type Ia SNRs contain a lot of iron. In core-collapse SNRs, the core collapses to form a neutron star, pulsar, or a black hole, while the ejecta expand into the surrounding ISM. The study of SNRs at multiple wavelengths provides important information about the properties of the material produced in SN explosions, including its composition, distribution, and ionization state. Multi-wavelength studies also tell us about the dynamic evolution of these objects and how they impact their surroundings.

There are two main types of SNRs; shell-type remnants and Crab-like remnants, or PWNe. In a shell-type remnant, an expanding supernova blast wave is a source of radio, visible, and x-ray emission, while a PWN has a central young pulsar that produces a wind of energetic particles that emits synchrotron radiation and interacts with the surrounding medium. There are approximately 60 known PWNe, and they are distinguished from shell-like remnants based on a number of properties, including their morphology, a flat power-law radio spectrum, high radio polarization, a power-law X-ray spectrum, and commonly a detection of a central pulsar (Bandiera 2002). Composite SNRs are those for which we observe an expanding PWN in addition to a thermal shell. This chapter outlines the evolution and observational properties of

shell-type SNRs and PWNe, while the evolution of composite remnants is discussed in more detail in Chapter 4.

1.2 Shell-type Supernova Remnants

Shell-type SNRs originate when the fast-moving SN ejecta drive a shock into the surrounding ISM, heating the gas to temperatures approaching 10^8 K. The heated gas emits thermal X-ray emission, while the acceleration of electrons by the shock produces synchrotron emission at radio wavelengths. The explosions release approximately 10^{53} erg of energy, most of which is in the form of neutrinos. About 10^{51} erg of this energy is in the form of thermal and kinetic energy that drives the expanding remnant. Initially, the supernova ejecta is in free expansion and is bounded by a forward shock that sweeps up the surrounding ISM. A reverse shock forms when the pressure in the freely expanding ejecta is lower than the pressure of the gas heated by the forward shock (McKee 1974). SNR shocks are collisionless shocks in which the material is not heated by two particle Coulomb interactions, but another mechanism acting on the particles behind the shock. The equilibration of the electron-ion temperature in SNRs occurs at a shorter time scale than expected from Coulomb interactions, which also indicates the presence of an additional heating and equilibration mechanism in SNRs (e.g. Hamilton & Sarazin 1984).

After the reverse shock propagates back to the interior of the SNR and heats the inner ejecta, the outer blast wave continues to expand until it eventually merges with the surrounding ISM. Examples of shell-type SNRs are shown in Figure 1.1. As summarized by Woltjer (1972), the dynamical evolution of SNRs can be divided into the following stages; the free expansion stage; the adiabatic or Sedov-Taylor stage; and the snowplow or radiative stage (Woltjer 1972; Chevalier 1982). The properties of each evolutionary stage are outlined below.

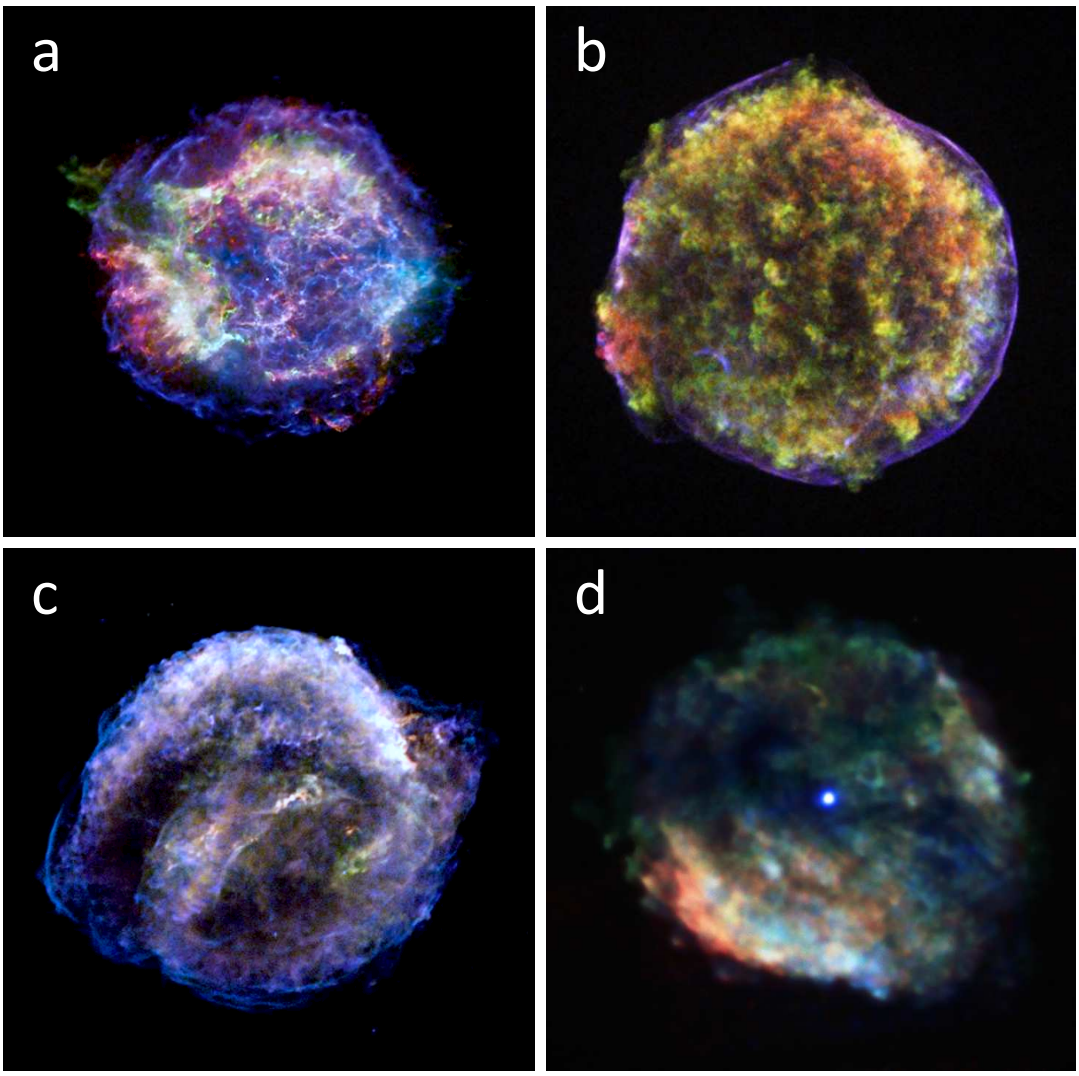

Figure 1.1 Examples of shell-type SNRs: a. Cassiopeia A (NASA/CXC/MIT/UMass Amherst/M.D.Stage et al.), b. Tycho's SNR (NASA/CXC/Rutgers/J.Warren & J.Hughes et al.), c. Kepler's SNR (NASA/CXC/NCSU/S.Reynolds et al.), and d. RCW 103 (NASA/CXC/Penn State/G.Garmire et al). Tycho and Kepler are SNRs that resulted from Type Ia SNe, while Cas A and RCW 102 resulted from core-collapse events.

1.2.1 The Free Expansion Stage

The free expansion stage of SNR evolution is governed by the explosion energy E_0, which is mostly converted into kinetic energy that drives the expansion of the ejecta. In this stage, the mass of the expanding ejecta is much greater than the mass of the swept-up ISM, and therefore the velocity of the expansion depends entirely on the kinetic energy and the ejected mass M_{ej}. The velocity and radius (R_{SNR}) of the SNR in the free expansion stage are given by

$$v_{SNR} = \sqrt{\frac{2E_0}{M_{ej}}} \tag{1.1}$$

and

$$R_{SNR} = \frac{v_{SNR}}{t} \tag{1.2}$$

where t is the age of the remnant. In the free expansion stage, the ejecta velocity is roughly constant with typical values on the order of $10^4\,\mathrm{km\,s^{-1}}$ for Type Ia SNe and $5000\,\mathrm{km\,s^{-1}}$ for core-collapse (Reynolds 2008).

1.2.2 The Sedov-Taylor Stage

The Sedov-Taylor stage begins when the mass of the swept-up ISM exceeds the mass ejected by the SN and the dynamics become governed by the total expanding gas and the initial explosion energy. The expanding SNR blast wave is decelerated and the reverse shock is driven into the inner ejecta, heating it to temperatures as high as 10^7 K. Since radiative losses are still negligible in this phase of evolution, the total energy of the remnant is conserved and is given by

$$E_{SNR} = \frac{1}{2}Mu^2 + \frac{4\pi}{3}R_{SNR}^3\frac{P}{(\gamma-1)}, \tag{1.3}$$

where u is the velocity of the post-shock gas, P is the pressure, and γ is the adiabatic index. The first term in the above equation is the kinetic energy of the shell, and the second term is thermal energy of the system. The velocity behind the shock u is given by

$$u = \frac{2}{\gamma + 1} \frac{dR_{SNR}}{dt}. \tag{1.4}$$

Assuming that the adiabatic heat index $\gamma = \frac{5}{3}$ and that there is a pressure equilibrium between the interior of the remnant and the shocked ISM, the radius and velocity of the SNR are given by

$$R_{SNR} = 1.15 \left(\frac{E_0 t^2}{\rho_0} \right)^{\frac{1}{5}} \tag{1.5}$$

and

$$v_{SNR} = \frac{2}{5} \frac{R_{SNR}}{t}, \tag{1.6}$$

where ρ_0 is the initial density of the ambient medium (Sedov 1959; Woltjer 1972; Truelove & McKee 1999). The Sedov-Taylor stage of SNR evolution ends when the outer blast wave decelerates enough for radiative cooling to become important.

1.2.3 The Radiative Stage

When radiative cooling becomes significant and the total energy contained in the SNR is no longer conserved, the SNR enters the radiative stage of evolution. The transition time, radius and swept-up mass at which the evolution becomes radiative are given by Blondin et al. (1998);

$$t_{cr} = 2.9 \times 10^4 E_{51}^{\frac{4}{17}} n_0^{-\frac{9}{17}} \; year, \tag{1.7}$$

$$R_{tr} = 19 E_{51}^{\frac{5}{17}} n_0^{-\frac{7}{17}} \; pc, \tag{1.8}$$

$$M_{tr} = 10^3 E_{51}^{\frac{15}{17}} n_0^{-\frac{4}{17}} \; M_\odot, \tag{1.9}$$

where $E_{51} = E_0/(10^{51}\text{erg})$ and the ambient medium is assumed to be uniform (Reynolds 2008, and references therein). At times longer than the transition time to the radiative phase, the momentum of the shell is conserved and $M(t)V_{SNR}(t) = constant$. At this time, the radius of the SNR is proportional to $t^{1/4}$. When the expansion velocity becomes subsonic, the SNR is dispersed by random motions in the ISM and it merges with the surrounding medium.

1.3 Pulsar Wind Nebulae

PWNe have been observed extensively at radio and X-ray wavelengths. Observations from *Chandra*, *Australia Telescope Compact Array* (ATCA) and the *Very Large Array* (VLA) have significantly improved our understanding of these systems. While all PWNe are characterized by synchrotron radiation from a pulsar wind, their observational properties can differ greatly. The factors that cause the variations in their physical properties include the evolutionary history of the pulsar's spin-down energy and injection of particles, the evolutionary stage of the SN ejecta, the pulsar's space velocity and inclination angle, and the PWN's interaction with the surrounding medium. The most famous examples of PWNe include the Crab Nebula and 3C 58, shown in Figure 1.2.

Observations of PWNe at various ages have led to a basic picture of their evolutionary development (Goldreich & Julian 1969; Kennel & Coroniti 1984; Reynolds & Chevalier 1984; van der Swaluw et al. 2004; Gelfand et al. 2009). Gaensler & Slane (2006) summarized the current understanding of the evolutionary phases that determine the general observational properties of PWNe. The PWN initially expands into unshocked SN ejecta and appears as a symmetric wind of particles, surrounded by an expanding SNR. In this thesis, the term "unshocked ejecta" refers to the inner SN ejecta that have not yet been reached by the SNR's reverse shock. These inner ejecta, however, have previously been shocked during the SN explosion and by the SNRs forward shock

(Isensee et al. 2009). The interaction between the expanding PWN and the SN ejecta may produce Rayleigh-Taylow instabilities that cause the system to take on a complex filamentary morphology, as in the Crab Nebula. The Rayleigh-Taylor instabilities may also form as a result of the interaction between the reverse shock and the expanding PWN. This occurs when the SNR reaches the Sedov-Taylor phase of evolution that begins when the ejecta have swept up a comparable mass of the ISM. If enough time has passed for the pulsar to have crossed a significant distance through the SNR, we may observe a bow shock as the pulsar interacts with the SN ejecta or the surrounding ISM (Gaensler & Slane 2006). In this section, the basic properties of PWNe and their early evolution are outlined. The evolution of composite remnants in which the PWN interacts with the expanding SNR and the reverse shock is outlined in Chapter 4.

1.3.1 Pulsar Properties

Emission from PWNe is powered by the rotational spin-down energy of the central pulsar, a rapidly rotating neutron star with a high magnetic field. The rate at which this energy is dissipated is given by (Gaensler & Slane 2006)

$$\dot{E} = 4\pi^2 I \frac{\dot{P}}{P^3} \tag{1.10}$$

where P and $\dot{P}$ are the pulsar's period and spin-down rate, and I is the neutron star's moment of inertia, typically assumed to be 10^{45} g cm^{-2} for a 1.4 $M_\odot$ sphere with a radius of 10 km. This rate of loss of the rotational energy is known as the spin-down luminosity and typical values of $\dot{E}$ for pulsars that produce PWNe are on the order of 10^{37} erg s^{-1}. If the pulsar's initial spin period is P_0, then the age of the pulsar is given by (Manchester & Taylor 1977)

$$\tau = \frac{P}{(n-1)\dot{P}} \left[1 - \left(\frac{P_0}{P} \right)^{n-1} \right] \tag{1.11}$$

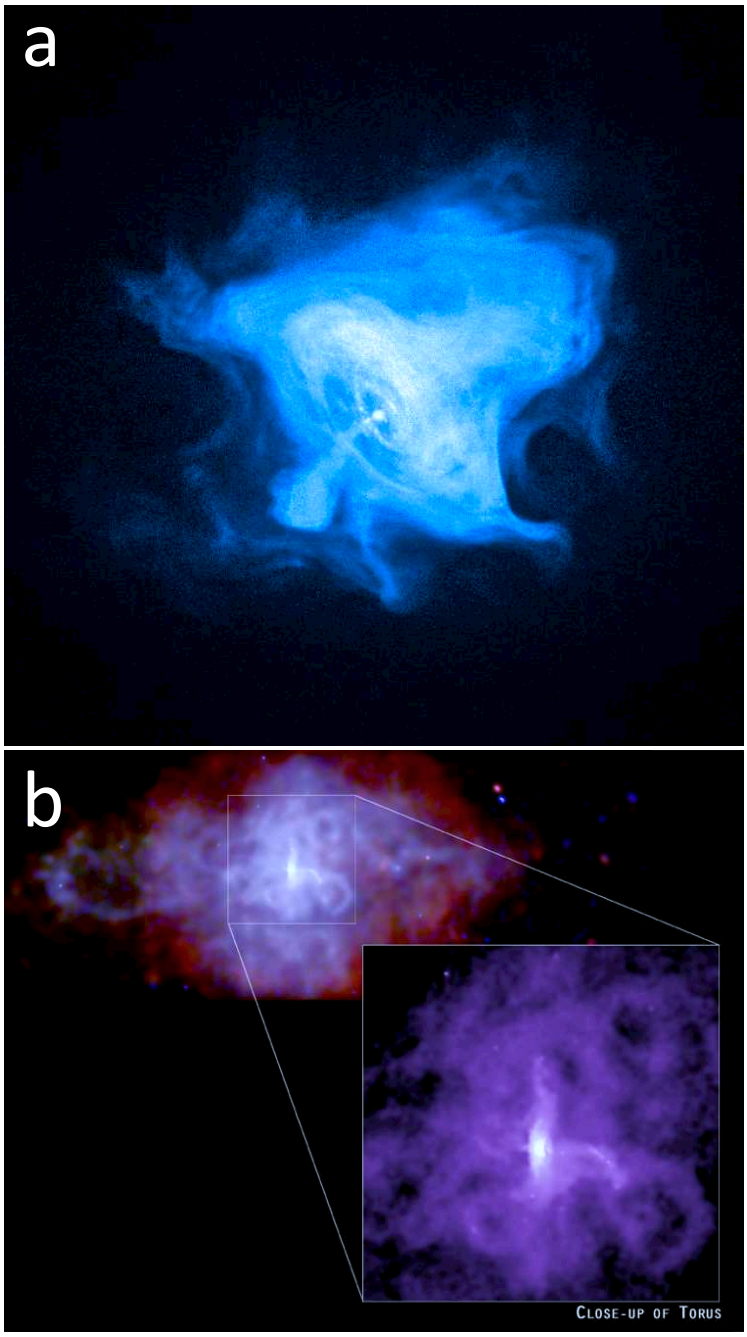

Figure 1.2 Examples of PWNe: a. Crab Nebula (NASA/CXC/SAO/F.Seward et al.), and b. 3C 58 (NASA/CXC/SAO/P.Slane et al.)

where n is the braking index in the expression $\dot{\Omega} \propto \Omega^n$ with $\Omega = 2\pi/P$. The braking index for magnetic dipole radiation is $n = 3$, but the measured values of the braking index are typically between 2 and 3 (e.g. Livingstone et al. 2007). In the case where the braking index n=3 and $\dot{P} \ll P$, the age of the pulsar τ reduces to

$$\tau = \frac{P}{2\dot{P}}, \tag{1.12}$$

known as the characteristic age. While the expression for the characteristic age can be used to estimate the age of the pulsar, it underestimates the actual age if P_0 is comparable to the current period P (Pacini & Salvati 1973; Gaensler & Slane 2006, and references therein). Assuming a constant braking index n, the expression for the evolution of the pulsar's spin-down luminosity with time is

$$\dot{E} = \dot{E}_0 \left(1 + \frac{t}{\tau_0}\right)^{-\frac{(n+1)}{(n-1)}}, \tag{1.13}$$

where $\dot{E}_0$ is the initial spin-down luminosity (Pacini & Salvati 1973).

1.3.2 Early Evolution of PWNe

The spin-down energy of the rotating pulsar generates a wind of particles that are accelerated in the pulsar's magnetic field, and that emit synchrotron radiation across the electromagnetic spectrum. The basic properties of PWNe were described by Rees & Gunn (1974) and Kennel & Coroniti (1984). Figure 1.3, taken from Slane (2005), illustrates their basic structure. As the pulsar wind expands into its surroundings, a termination shock forms at the location where the ram pressure of the wind balances the internal pressure of the nebula. The radius of this termination shock for a spherical

wind is given by (Gaensler & Slane 2006)

$$R_{TS} = \left(\frac{\dot{E}}{4\pi c P_{PWN}} \right)^{\frac{1}{2}}, \tag{1.14}$$

where P_{PWN} is the PWN pressure. At the termination shock, the particles are re-accelerated and they produce synchrotron radiation as they flow downstream of the shock (Kennel & Coroniti 1984; Emmering & Chevalier 1987). The outer regions of the PWN are confined by the surrounding material, typically the expanding SN ejecta. In the early stages of PWN evolution, the unshocked SN ejecta are in free expansion and the sound speed in the interior of the SNR is lower than the expansion velocity of the PWN. The PWN expands supersonically and drives a shock into the expanding ejecta. The confining radius of the PWN is given by

$$R_{PWN}(t) = C \left(\frac{\dot{E}_0 t^3}{\rho(t)} \right)^{\frac{1}{5}}, \tag{1.15}$$

where C is a constant on the order of unity and $\rho(t)$ is the density of the ambient medium in which the PWN expands (van der Swaluw et al. 2001). If the inner SNR density is expressed as

$$\rho(t) = \frac{3 M_{ej}}{4\pi R_{SNR}^3(t)}, \tag{1.16}$$

where M_{ej} is the total ejected mass, then the outer PWN radius can be expressed as

$$R_{PWN}(t) = C \left(\frac{\dot{E}_0 t}{E_0} \right)^{\frac{1}{5}} R_{SNR}(t). \tag{1.17}$$

Young PWNe typically have a toroidal morphology and are elongated along the pulsar's spin axis. The collimation of the flow along the pulsar's spin axis produces jets of emission that have been observed for many PWNe, including the Crab Nebula and G54.1+0.3, discussed in Chapters 2 and 3. As the PWN expands into the inner SN

ejecta, Rayleigh-Taylor instabilities may form and produce a complex filamentary morphology, as observed in the Crab Nebula (Hester 2008). Multi-wavelength observations of PWNe in early stages of their evolution can reveal important information about the pulsar progenitor, PWN properties and evolution, composition of the SN ejecta, and even freshly formed SN dust. Examples of these system are presented in two case studies in Chapters 2 and 3. Late evolution of PWNe is discussed in Chapters 4 and 5.

1.4 Observational Properties of SNRs and PWNe

1.4.1 Non-thermal Emission

Emission mechanism responsible for non-thermal emission in SNRs are synchrotron radiation, non-thermal bremsstrahlung resulting from a non-thermal electron distribution, and inverse Compton emission resulting from scattering of photons by relativistic electrons (e.g. Longair 1994). Synchrotron spectra of PWNe are characterized by a broken power law distribution, in which the flux follows the form $F_\nu \propto \nu^{-\alpha}$, where α is called the spectral index. Radio observations of PWNe show an amorphous morphology, and a flat spectrum with a spectral index α ranging from 0.0-0.3. X-ray observations often show a toroidal morphology with jets and a much steeper spectrum, with α ranging from 0.5-0.9 (Kaspi et al. 2006; Gaensler & Slane 2006). In X-ray images, the PWN usually has a much smaller spatial extent, since the particles that radiate at high frequencies have shorter lifetimes and radiate their energy before they can reach large distances. In order to account for the change in spectral index from radio to X-ray wavelengths, one or more spectral breaks are required. The spectral breaks may either be due to breaks in the initial distribution of injected particles or the evolution of the remnant over time. We expect to see at least two different regions in the spectrum with different spectral indices that are separated by a break frequency. Other factors can affect the shape of the integrated spectrum over time, including the change in the

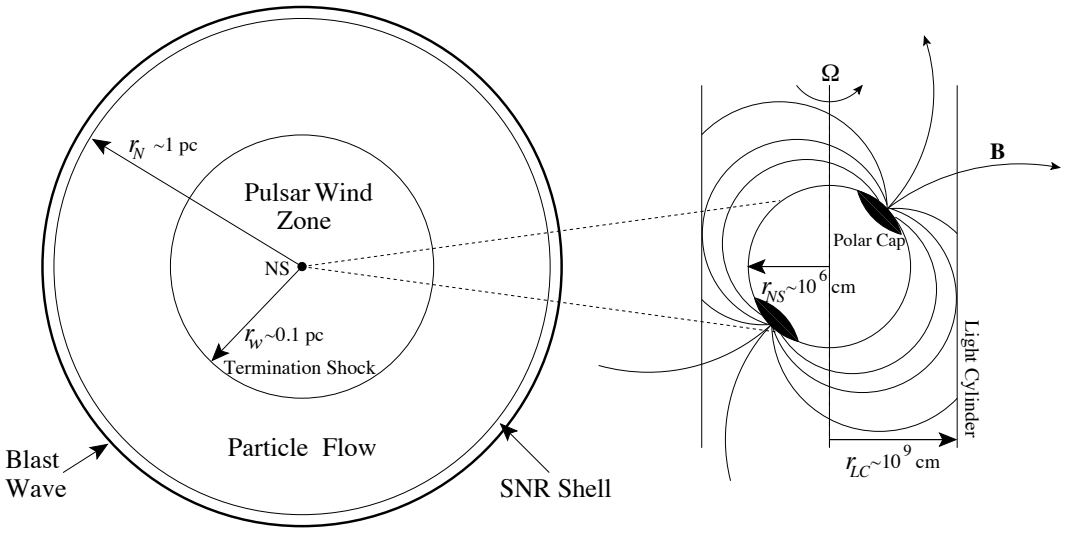

Figure 1.3 Schematic diagram of the basic structure of a PWN from Slane (2005). The radius of the wind termination shock and the radius of the outer PWN boundary are labeled by r_w and r_N, respectively.

energy input of the pulsar, conversion efficiency of spin-down energy into synchrotron radiation, acceleration of particles in different locations in the nebula, SNR expansion, changes in the magnetic field, and the interaction between the pulsar wind and the SN ejecta and the ISM (Bandiera 2002). The spectral index can also vary spatially across the remnant, since particles of different ages are being sampled, and the overall index usually represents a spatial average over the entire nebula. This section summarizes the basic observational properties of the emission from pulsar winds and gives an overview of the models that describe their spectral evolution.

Synchrotron Spectra

PWNe are strong sources of synchrotron emission that originates from the magnetic fields and relativistic electrons and positrons in the remnant. In order to explain the synchrotron emission observed from these remnants, a continuous supply of relativistic electrons and magnetic flux is required. The study of this emission and the analysis of synchrotron spectra provide important information on the characteristics of the particles injected into the nebula and the injection processes that take place in SNRs.

The two basic equations needed to explain the synchrotron spectra are the radiated power of an electron that follows (Longair 1994)

$$\frac{-dE}{dt} \propto B^2 E^2 \tag{1.18}$$

and the critical frequency at which the spectrum of an electron sharply peaks;

$$\nu_{crit} \propto BE^2, \tag{1.19}$$

where E is electron energy and B is the magnetic field. There is an additional dependence on the pitch angle, but here we assume an isotropic distribution, averaged over all pitch angles. We assume that a power-law distribution of electrons is contributing

to the observed synchrotron spectrum and that it has the form $N(E)dE \propto E^{-p}dE$, where $N(E)dE$ is the number of electrons in a unit volume in a specific energy range, and p is the power-law index. The synchrotron spectrum can then be expressed by

$$L_\nu d\nu = \left(\frac{-dE}{dt}\right) N(E)dE. \tag{1.20}$$

Integration of this equation over a desired frequency range leads to a luminosity of the form

$$L_\nu \propto B^{(p+1)/2}\nu^{-(p-1)/2}. \tag{1.21}$$

If the magnetic field strength is kept constant then for a source with luminosity L_ν, the spectrum of the synchrotron radiation will follow a power law of the form $L_\nu \propto \nu^{-\alpha}$, where α is the spectral index equal to $(p-1)/2$ (e.g. Longair 1994). All changes in the slope of the luminosity are caused by breaks in the present electron distribution. These breaks may either be due to breaks in the initial distribution of injected particles or to the evolution of the remnant over time (Bandiera 2002).

In order to uncover the spectrum of the injected particles, one needs to correct for the evolution of the particles over the lifetime of the remnant. The two processes that are responsible for the evolutionary changes in the spectrum are synchrotron losses and adiabatic losses. The adiabatic losses are dominant for lower energy particles and do not change the shape of the particle distribution. The synchrotron losses are dominant for high energy particles and they cause the particle distribution to steepen over time. In the synchrotron spectrum of SNRs, we expect to see at least two different regions with different spectral indices separated by a *break frequency*, corresponding to a *break energy*. This energy is given by

$$E_{break} \propto \frac{1}{B^2 t}, \tag{1.22}$$

where t is the time that has passed since the electrons had a power law distribution for all energies (Bandiera 2002).

If no other effects are included, as the remnant evolves, the break frequency and energy will decrease over time, but the general shape of the synchrotron spectrum will remain unchanged. However, other factors can affect the shape of the spectrum of SNRs over time, including variations in the magnetic field, and the acceleration of particles in the nebula. Higher energy electrons and electrons with higher pitch angles lose energy faster, and therefore synchrotron losses will cause the observed spectrum to steepen at frequencies larger than the break frequency. Acceleration of particles through adiabatic processes can increase the energy of the electrons so that the higher energy electrons are repopulated. This will cause the shape of the spectrum to change because the slope will once again flatten at higher frequencies.

Several models have been proposed for the evolution of synchrotron emission in PWNe (Kardashev 1962; Jaffe & Perola 1973; Reynolds & Chevalier 1984; Bandiera 2002; Gelfand et al. 2009). Bandiera (2002) outlines the basic processes and parameters that the evolution of the synchrotron emission depends on. These processes include; the change in the energy input of the central pulsar over time that depends on the spin-down of the pulsar, the fraction of power that goes into injected particles, the expansion of the SNR, the effects due to changes in the magnetic field, and the effects of adiabatic and synchrotron losses on the evolution of particles.

Classical models that have been developed are based on the model by Kardashev (1962), who considers a single injection of particles into the nebula with no further scattering in pitch angle over time. A model by Jaffe & Perola (1973) includes pitch angle scattering. If particles are scattered to higher pitch angles they will radiate faster, which would cause the spectral index to steepen faster at higher frequencies. There are also models that assume a constant injection of electrons with power-law spectra. One such model is proposed by Pacini & Salvati (1973) and it assumes that the central pulsar continuously injects magnetic energy and relativistic electrons into the remnant. More sophisticated models include models by Reynolds & Chevalier (1984) and Gelfand

et al. (2009).

The models described above can be directly tested with observations of SNRs. Since the spectral breaks occur somewhere between the radio and X-ray wavelengths, observations at intermediate wavelengths, such as optical and IR, are required for determining the general shape of the spectrum. The locations and magnitudes of the spectral breaks allow comparisons between the observed spectral shape and the current models, which can disentangle the various evolutionary processes that cause changes in the spectrum. The globally averaged spectral index in the Crab Nebula changes by 0.5 from radio to optical wavelengths which agrees with the prediction of the Kardashev model. However, other breaks in the spectrum of the nebula cannot be explained by any single model without assuming that the breaks were present in the initial injected electron distribution. Recent observations of the Crab Nebula at X-ray wavelengths, and observations in the IR by the *Spitzer* Space Telescope suggest that combinations of developed models are required to explain the overall spectral shape. This analysis is outlined in Chapter 2.

1.4.2 Thermal Emission

Thermal emission from SNRs is usually associated with a shell component from a SN blast wave and is dominated by emission from hot gas and dust, and atomic line emission. Composite systems, which contain a PWN along with a thermal shell, are perfect laboratories for the study of the interaction between pulsar winds and SN ejecta and ISM. Observations of X-ray thermal emission can be used to derive hot gas temperatures, ionization state, the energy of the SN explosion, the density of the surrounding ISM, and the evolutionary state of the system. X-ray thermal emission from SNRs originates from hot gas associated with the SN ejecta or the heated ISM. Radiation mechanisms that produce the continuum emission are thermal bremsstrahlung resulting from acceleration of free electrons in the vicinity of ions, free-bound emission resulting

from radiative recombination, and two photon emission resulting from deexcitation by a simultaneous emission of two photons. Spectral line emission at X-ray wavelengths originates from highly ionized atomic species.

Each of the emission mechanisms contributes to the spectrum of the thermal plasma emission in SNRs. Bremsstrahlung is the dominant emission mechanism for kT $\gg$ 1 keV, while free-bound emission dominates for temperatures much less than 0.1 keV. Two-photon emission is important in the temperature range between 0.5 – 5 keV (Kaastra et al. 2008). Due to the relatively short lifetime of SNRs, ionization equilibrium is often not achieved in the low density gas, and the thermal plasma can be modeled with non-equlibrium ionization (NEI) models that provide information about the ionization state of the gas.

IR thermal emission from SNRs can originate from atomic and molecular line emission and continuum emission from dust. IR observations of SNRs yield information about the SN ejecta that may not be available at X-ray wavelengths. Spectroscopy at mid-IR wavelengths contains ionic lines that can be used as diagnostics of the elemental abundances, gas temperatures and densities. Expansion and shock velocities can be extracted from the structure of the observed emission lines, as will be shown in Chapters 2 and 3. As PWNe interact with the inner SN ejecta and dust, they can illuminate material that would otherwise be unobservable in SNRs. The contribution of dust that SNe make to the ISM is still not well understood, and systems in which the PWNe interacts with freshly formed SN dust can shed light on the composition and mass of dust produced in SN explosions.

1.4.3 Dust Emission

Since SNe are capable of producing large quantities of carbon and other condensible elements, it is speculated that they are also capable of producing large quantities of dust (Clayton 1982; Gehrz & Ney 1987; Dwek 1988; Gehrz 1988). In fact, SNe were

thought to be major suppliers of interstellar dust and one of the main contributors to the total dust content of the ISM. Shortly after the SN explosion, as the ejected material cools, small dust particles condense out of the gas of heavier elements inside the ejected material. Dust grains are collisionally heated by energetic particles inside the remnant and are warmed enough for their radiation to be emitted mostly at IR wavelengths. However, recent IR studies of SNRs have found no evidence for large quantities of dust particles and some have yielded dust masses a hundred times lower than theories predict (e.g. Douvion et al. 2001; Dwek 2004; Green et al. 2004; Borkowski et al. 2006; Temim et al. 2006). These puzzling results and the question of just how much dust supernovae create and inject into the ISM are still not very well understood. PWNe and their interaction with dusty ejecta can improve our understanding of dust production in SNe.

The existing results on the formation and evolution of dust in core-collapse SN have recently been reviewed by Kozasa et al. (2009). The amount and type of dust that is injected into the ISM by SNe depends on the available abundances of condensable elements ejected by the SN, environmental conditions, such as the gas temperature and density, and the degree to which the dust grains are destroyed by the SNR shocks. Theoretical models based on abundances of SN ejecta show that the dust formed in SNRs can have a range of different compositions, with the most abundant dust grains being those of $MgSiO_3$, SiO_2, Mg_2SiO_4, Si, and C. The total predicted masses of dust produced in SNe range between 0.1–0.7 $M_\odot$ (Kozasa et al. 2009). However, a large fraction of the produced dust may be destroyed by erosion and sputtering in the region between the forward and reverse shocks, so the total mass of surviving dust is 0.04–0.2 $M_\odot$ (e.g. Dwek et al. 2008; Kozasa et al. 2009).

In recent years, the sensitivity and resolution of the *Spitzer* Space Telescope has enabled mass estimates of freshly formed dust for several SNRs (e.g. Temim et al. 2006). Rho et al. (2009) estimated the total dust mass in Cas A and other SNRs for

which the dust emission traces the spatial distribution of SN ejecta. The mass of freshly formed dust in these objects is in the 0.02–0.05 $M_{\odot}$, an order of magnitude smaller than models predict. The shape of the IR spectrum and the presence of various emission features are clues that can help determine the composition of dust grains in a particular environment. Based on the IR spectra and the observed emission features, Rho et al. (2009) find that dust grains formed in SNRs are mainly composed of SiO_2, $MgSiO_3$, Si, SiC, Al_2O_3, and Fe. However, the IR spectra also show emission features that are not well described by these compositions, and additional observations and modeling are required to fully understand the compositions and masses of this freshly formed dust. Since young PWNe expand into inner SN ejecta that has not yet been reached by the reverse shock, they provide a unique laboratory in which the freshly formed SN dust can be investigated before it is mixed with swept-up ISM dust. Studies of two PWNe interacting with dusty ejecta, the Crab and G54.1+0.3, are presented in Chapters 2 and 3.

Chapter 2

IR Imaging and Spectroscopy of the Crab Nebula

ABSTRACT

Spitzer Space Telescope 3.6, 4.5, 5.8, 8.0, 24, and 70 μm images of the Crab Nebula obtained with IRAC and MIPS cameras, Low- and High-resolution *Spitzer* IRS spectra of selected positions within the nebula, and a near-IR ground-based image made in the light of [Fe II] 1.644 μm are presented in this work. The 8.0 μm image, made with a bandpass that includes [Ar II] 7.0 μm, resembles the general morphology of visible Hα and near-IR [Fe II] line emission, while the 3.6 and 4.5 μm images are dominated by continuum synchrotron emission. The 24 μm and 70 μm images show enhanced emission that may be due to line emission or the presence of a small amount of warm dust in the nebula on the order of less than 1% of a solar mass. The ratio of the 3.6 and 4.5 μm images reveals a spatial variation in the synchrotron power law index ranging from approximately 0.3 to 0.8 across the nebula. Combining this information with optical and X-ray synchrotron images, a broadband spectrum that reflects the superposition of the flatter spectrum jet and torus with the steeper diffuse nebula is derived, along with

suggestions of the expected pileup of relativistic electrons just before the exponential cutoff in the X-ray. The pulsar, and the associated equatorial toroid and polar jet structures seen in *Chandra* and *Hubble* Space Telescope (HST) images (Hester et al. 2002) can be identified in all of the IRAC images. The IR photometry of the pulsar is presented. The forbidden lines identified in the high resolution IR spectra are all double due to Doppler shifts from the front and back of the expanding nebula and give an expansion velocity of $1264\,\mathrm{km\,s^{-1}}$.

A large portion of this work has been published in the October 2006 issue of the Astronomical Journal (Temim et al. 2006) and has been reproduced here by permission of the AAS (American Astronomical Society). This work was produced in collaboration with Charles E. Woodward (University of Minnesota), Robert D. Gehrz (University of Minnesota), Thomas L. Roellig (NASA Ames Research Center), Nathan Smith (University of Colorado), Lawrence R. Rudnick (University of Minnesota), Elisha F. Polomski (University of Minnesota), Kris Davidson (University of Minnesota), Lunming Yuen (Technosciences Corp., Moffett Field, CA), and Takashi Onaka (University of Tokyo).

2.1 Introduction

The Crab Nebula, formed by a Type II, core collapse, SN explosion in 1054 AD, is one of the youngest known Galactic SNRs and one of the most studied objects in the Galaxy. The quantity and high quality of observations of the Crab across the electromagnetic spectrum have allowed detailed studies of its complex structure and evolution. Hester (2008) recently summarized our current understanding of the Crab and synthesized the available data and theories into a single physical interpretation. The Crab is a classical example of a PWN in early stages of its evolution. It is powered by a 33 ms pulsar, at a distance of $\sim 2\,\mathrm{kpc}$. The pulsar has a spin-down luminosity of $5 \times 10^{38}\mathrm{erg\,s^{-1}}$, a large fraction of which goes into producing a pulsar wind that expands into the inner SN ejecta. A torus of synchrotron emission from the shocked wind is observable from X-ray

to IR wavelengths. At the outer boundary, the nebula is confined by the surrounding SN ejecta that is being shocked and accelerated by the pulsar wind. The complex morphology of the Crab Nebula's thermal filaments is shown in Figure 2.1. They are composed of $\sim 2-5\,M_{\odot}$ of SN ejecta that is swept-up by the PWN. The finger-like structures are produced by Rayleigh-Taylor instabilities that form when the lighter synchrotron plasma encounters the denser ejecta material. The gas in the filaments is photoionized by the synchrotron nebula, and it shows expansion velocities that range from $700-1800\,\mathrm{km\,s^{-1}}$. Dust is observed in the Crab in the form of an IR excess above the synchrotron spectrum and in extinction against the synchrotron background. The outer SNR still remains undetected. It is thought that the Crab is expanding inside a cavity, so that the outer blast wave has still not interacted with enough material to be observable. The current consensus appears to be that the Crab is a PWN that is expanding inside a much larger, free-expanding SNR (Hester 2008, and references therein). A summary of the Crab Nebula's structure, as described above, is illustrated in Figure 2.2, from Hester (2008).

In the last two decades, the wealth of observational and theoretical work on the Crab have led to a basic understanding of its evolutionary stage and structure. However, a lot of work remains to be done before we can fully understand the details of the Crab's morphology and the involved physical processes. This Chapter presents a study of the highest-quality IR observations of the Crab Nebula, obtained with the *Spitzer* Space Telescope, that provide new spatial and spectral information on the non-thermal emission, line emission from filaments, and dusty ejecta.

The IR is an ideal spectral region in which to test the theories of dust formation in SNRs, because dust grains emit strongly in the IR as do forbidden emission lines from condensable metals that remain in the gas phase. Previous IR studies have failed to reveal evidence for any large amount of dust in SNRs have provided us with somewhat of a mystery (Gehrz & Ney 1990; Arendt et al. 1999; Douvion et al. 2001; Dwek 2004;

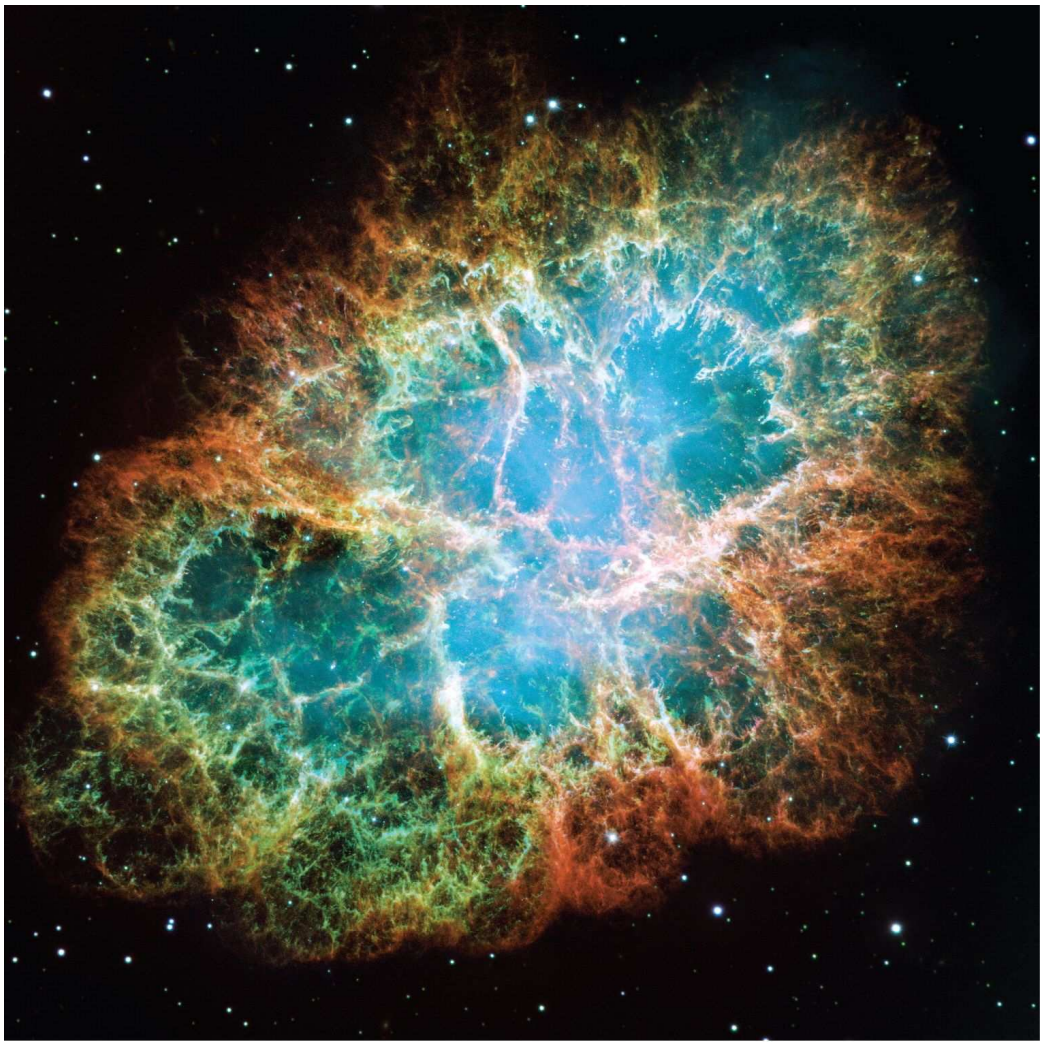

Figure 2.1 Composite Hubble Space Telescope image of the Crab Nebula from Hester (2008). The synchrotron emission from the PWN is shown in blue and the filaments formed from the swept-up SN ejecta are shown in the optical lines of [O III] in red, [S II] in green, and [O I] in blue.

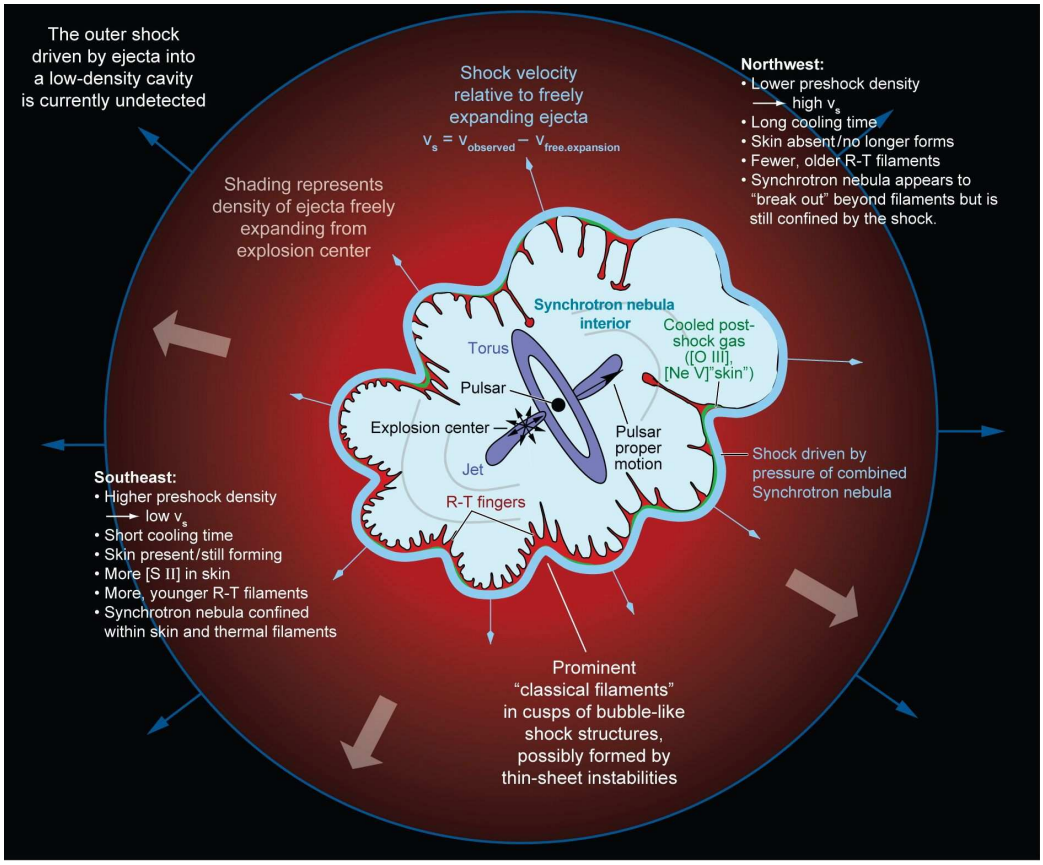

Figure 2.2 The cartoon from Hester (2008) summarizes the basic structure of the Crab Nebula.The central pulsar forms a PWN that is confined by the freely expanding SN ejecta. Rayleigh-Taylor instabilities form at the interface between the PWN and the denser ejecta, producing a finger-like morphology.

Green et al. 2004). Guaranteed Observation Time (GTO) on NASA's *Spitzer* Space Telescope (Werner et al. 2004; Gehrz et al. 2007) was used to obtain IR images and spectroscopy of the Crab Nebula. Previous IR observations have indicated that there is a paucity of dust in the Crab. Infrared Astronomical Satellite (IRAS) observations revealed an IR excess at wavelengths longer than 12 μm that was attributed to thermal emission from 0.005-0.03 $M_{\odot}$ of dust (Marsden et al. 1984). Further evidence for dust in the Crab Nebula was found in the form of optical extinction in the filaments (Hester et al. 1990; Fesen & Blair 1990; Blair et al. 1997; Sankrit et al. 1998). Studies using the Infrared Space Observatory (ISO), Douvion et al. (2001) report no evidence of spectral features from dust emission in the ISOCAM spectra, while Green et al. (2004) calculate an upper limit of 0.02 $M_{\odot}$ of warm dust from the far-IR excess seen by ISOPHOT.

The Crab Nebula is one of the brightest synchrotron sources in the Galaxy. It is a prototype of a class of SNRs called the pulsar wind nebulae that are powered by a central pulsar. A large fraction of the Crab pulsar's spin down luminosity is converted into the nebular synchrotron luminosity, from radio through gamma-rays. The details of this conversion are quite uncertain. The Kennel & Coroniti (1984) steady-state spherical magnetohydrodynamic (MHD) model still provides the best description of the optical and X-ray profiles, but cannot tie them together with the radio synchrotron emission.

The unprecedented sensitivity of the IR imagers and spectrometers of *Spitzer* present an unparalleled opportunity to search for dust and forbidden line emission in the Crab Nebula and study in detail the spatial variations of synchrotron emission across the remnant. This chapter presents 3.6, 4.5, 5.8, 8.0, 24, and 70 μm images of the Crab Nebula obtained with the *Spitzer* IRAC and MIPS cameras, IRS spectra of selected positions within the nebula, and a near-IR ground-based image made in the light of [Fe II]1.644 μm.

2.2 Observations and Data Reduction

Observations of the Crab Nebula were made using the Infrared Array Camera (IRAC) aboard the *Spitzer* (Werner et al. 2004) at 3.6, 4.5, 5.8 and 8.0 μm and the Multiband Imaging Photometer for *Spitzer* (MIPS) at 24 and 70 μm as part of the Gehrz Guaranteed Time Observing Program (GGTOP, Program ID: 130). High and low resolution *Spitzer* 5-40 μm spectra of selected regions of the Crab Nebula were made using the Infrared Spectrometer (IRS) under the Roellig Guaranteed Time Observing Program (RGTOP, Program ID: 24).

2.2.1 IRAC Images

The IRAC (Fazio et al. 2004) observations were made on 2004 March 6, under the AORKey 6588928, using 12 second exposures and the High Dynamic Range (HDR) mode at 4 dither positions obtained in a cycling dither pattern. The Basic Calibrated Data (BCD) products from the *Spitzer* Science Center (SSC) pipeline version S11.0.2, calibrated in units of MJy per steradian, were used in our post pipeline processing.

Post BCD processing was conducted using the 101504 version of the SSC's Mosaicker and Point Source Extractor (MOPEX) software. The reduction with MOPEX consisted of three steps: Cosmetic Fix, Background Matching, and Mosaicker. The field of view of the final mosaics is approximately $6.0' \times 6.0'$with a final pixel scale of $0.86''$ per pixel.

2.2.2 MIPS Images

The MIPS (Rieke et al. 2004) 24 μm and 70 μm observations of the Crab Nebula were carried out on 2004 March 14, under the AORKey 6588672, using an exposure time of 3 seconds and 10 seconds, respectively. The data was processed with the SSC pipeline version S11.4.0. The 24 μm BCD data was corrected for image distortions caused by

Table 2.1 Crab Nebula: IRAC and MIPS Data

				Nebula Flux Density		Pulsar Flux Density	
Wavelength		Exp. Time	Pixel Scale	Raw	Extinction Corrected	Raw	Extinction Corrected
(μm)		(s)	($''$/pix)	(Jy)	(Jy)	(mJy)	(mJy)
IRAC	3.6	12	0.86	11.65 ± 0.03	12.63 ± 0.22	2.45 ± 0.16	2.66 ± 0.19
	4.5	12	0.86	13.81 ± 0.02	14.35 ± 0.26	2.34 ± 0.17	2.42 ± 0.18
	5.8	12	0.86	16.31 ± 0.06	16.77 ± 0.13	2.12 ± 0.19	2.18 ± 0.19
	8.0	12	0.86	17.74 ± 0.04	18.33 ± 0.13	1.85 ± 0.18	1.91 ± 0.19
MIPS	24.0	3	2.5	59.8 ± 0.4			
	70.0	10	4.0	157 ± 2			

the focal plane and mosaicked with Image Reduction and Analysis Facility (IRAF)[1]. The 70 μm images were mosaicked with MOPEX and have a pixel scale of 4.0$''$ per pixel. The pixel scale of the final MIPS 24 μm mosaic is 2.5$''$ per pixel. The summary of the IRAC and MIPS data is listed in Table 2.1.

2.2.3 IRS Spectra

Observations of the Crab nebula were obtained with all four modules of the IRS instrument (Houck et al. 2004) on 2004 March 5, under the AORKey 3857664. The IRS observations were taken in staring mode centered at the position RA 5h34m31.02s, Dec 22d01$'$10.1$''$(J2000). This position, designated as IRS-Tgt-Cntr in the discussions below, is located in the center of the nebula, near but not coincident with the pulsar position located at RA 5h34m31.97s, Dec 22d00$'$52.1$''$(J2000). Since the four IRS modules all have different slit sizes and orientations, this position in the nebula was the only one in common to all the modules. For the two low-resolution IRS modules the long slits allowed sampling of other regions of the nebula, as shown in Figure 2.3. Integration

[1]IRAF is distributed by the National Optical Astronomy Observatories, which are operated by the Association of Universities for Research in Astronomy, Inc., under cooperative agreement with the National Science Foundation

times, wavelength coverage, and the spectral resolution for each IRS module is given in Table 2.2. Data from other locations in the nebula sampled by the long slits in the low-resolution modules is also reported. Since the IRS staring mode involves nodding between two positions in each slit, some of these regions have the same integration times as those reported above, while others have half the time. Further explanation of how nodding along the slits is implemented in the IRS staring mode can be found in the relevant section of the *Spitzer* Observers Manual[2].

The IRS data were reduced using the Spectroscopic Modeling, Analysis and Reduction Tool (SMART) data reduction package described in Higdon et al. (2004). Due to the large spatial extent of the Crab nebula with respect to the IRS slit dimensions there was no blank sky available for zodiacal light subtraction. In this region of the sky the zodiacal sky background levels are roughly one-fourth of the combined emission from the Crab Nebula and zodiacal light at the worst-case wavelengths around 15 μm. As a result, the data reported here have a small contribution from the Zodiacal background that must be accounted for. The observed spectra from each of the IRS modules for the IRS-Tgt-Cntr position are shown in Figure 2.4. In these spectra the high-resolution module extractions were both full-aperture, while for the low-resolution module's long slits the extractions were performed in 5 pixel wide sub-slits centered at the location of IRS-Tgt-Cntr. The effects of the different slit widths and extraction aperture sizes are immediately noticeable in the relative strengths of the emission baselines in the spectra in Figure 2.4.

2.2.4 Near-IR Imaging

Since [Fe II] 25.99 μm emission may contribute to the emission morphology at 24 μm (see below), it will be useful to compare MIPS to a ground-based image of the [Fe II]

[2]See http://ssc.spitzer.caltech.edu/documents/SOM / for the most current version of the Spitzer Observers Manual

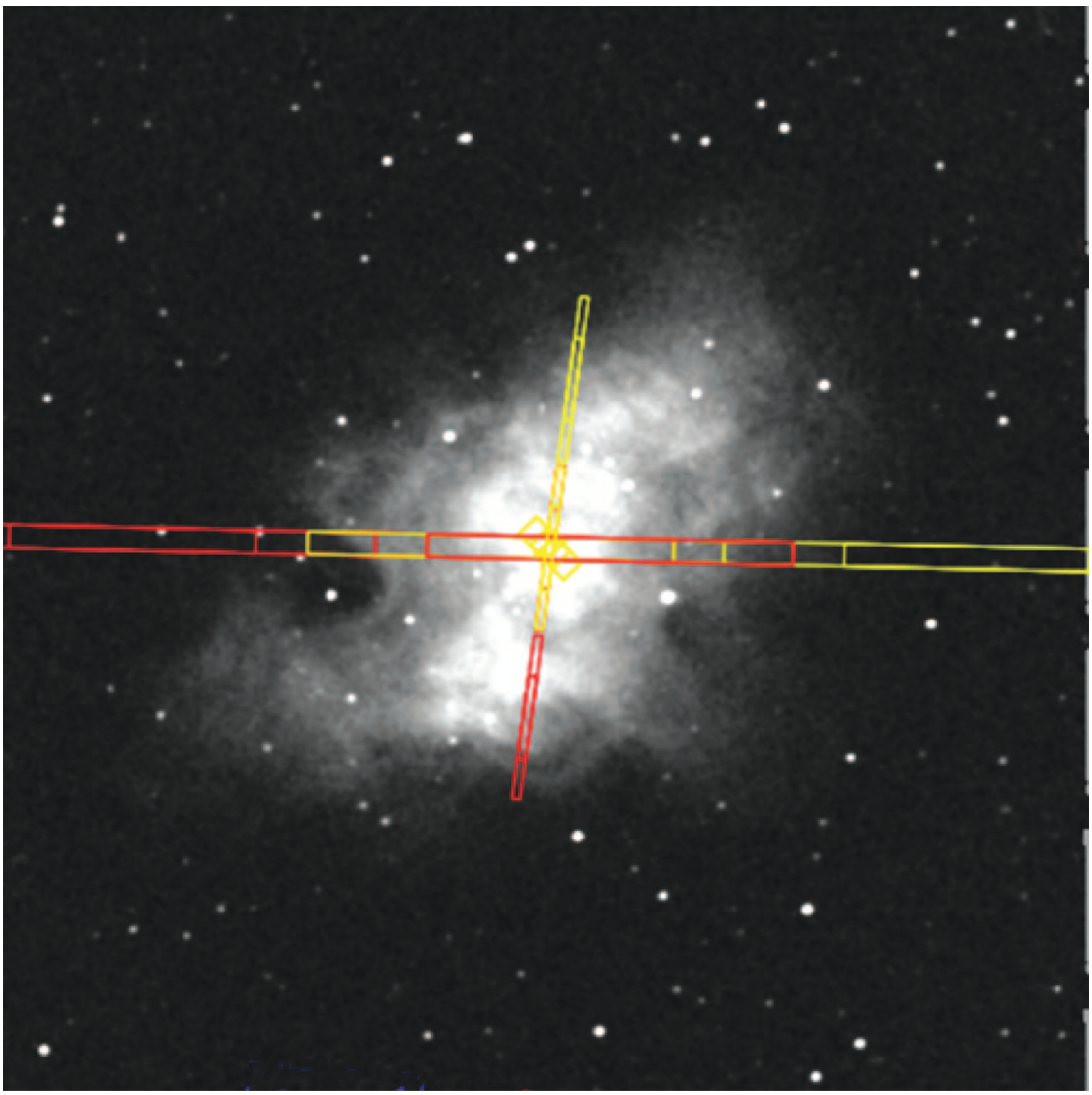

Figure 2.3 A 2MASS K-band image (Skrutskie et al. 2006) of the Crab nebula, with the IRS slits overlaid at the time of the observations reported here. This figure was produced by the SPOT software at the *Spitzer* Science Center and shows each IRS module's aperture orientation in the two nod positions along the slits. The long and wide aperture running horizontally belongs to the Long-Low module, while the much thinner aperture running more vertically belongs to the Short-Low aperture. The high-resolution modules' apertures are much shorted and only the Long-High aperture is readily visible in this figure.

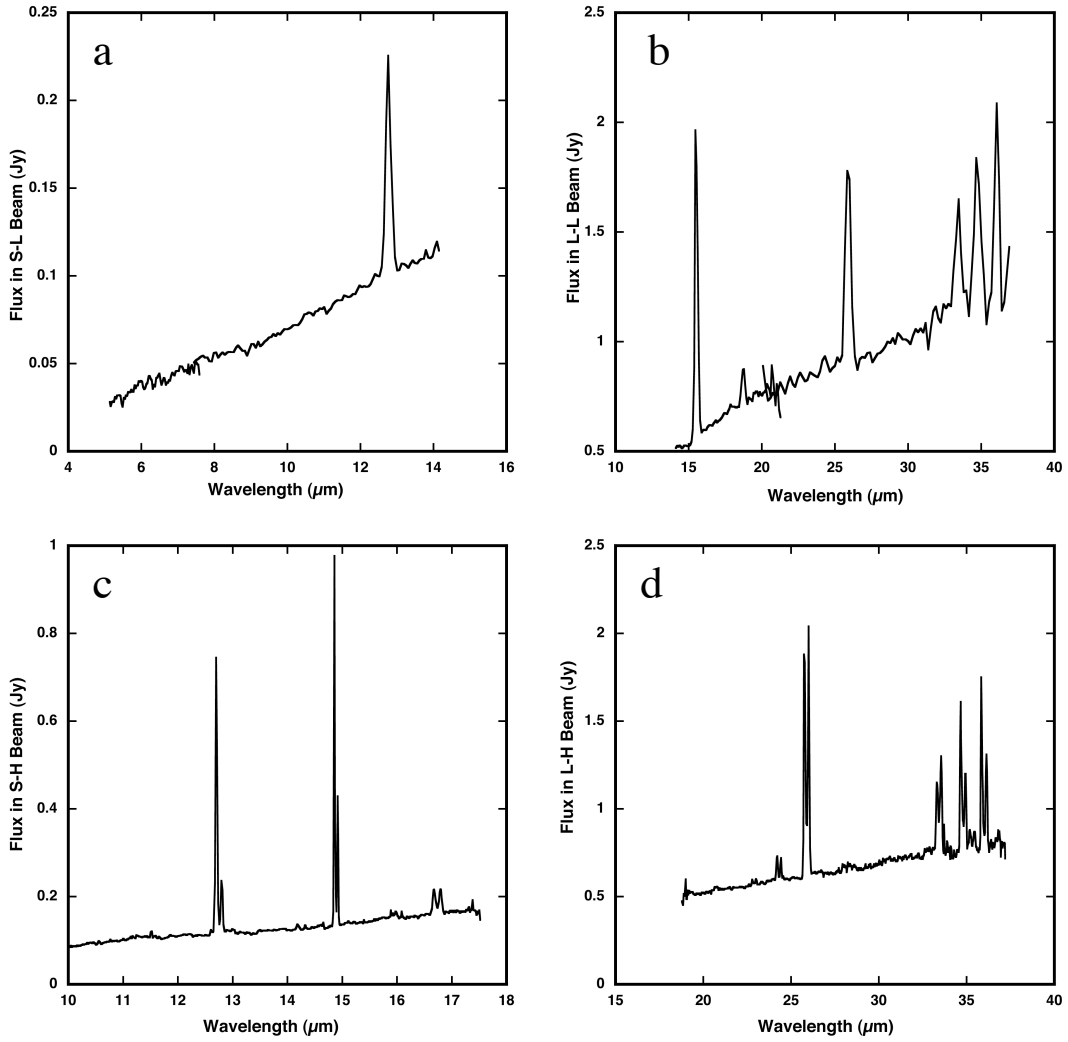

Figure 2.4 *Spitzer* IRS spectra of the Crab nebula, taken at the IRS-Tgt-Cntr position. Panel (a): Short-Low module with a 3.6″x 9.0″extracted beam size; (b) Long-Low module with a 10.5″x 25.5″extracted beam size; (c) Short-High module with a 4.7″x 11.3″extracted beam size, and (d): Long-High module with a 11.1″x 22.3″extracted beam size. Identifications of the numerous emission lines are given in Tables 2.3 and 2.4.

Table 2.2 Crab Nebula: IRS Observations

IRS Module Name	Spectral Range (μm)	Spectral Resolution ($\lambda/\Delta\lambda$)	Integration Time at IRS-Tgt-Cntr (sec)
Short-Low (SL)	5.2 - 14.3	64 - 128	928
Long-Low (LL)	14.1 - 38.0	64 - 128	488
Short-High (SH)	9.9 - 19.6	$\sim$ 600	1768
Long-High (LH)	18.9 - 37.2	$\sim$ 600	1936

1.644 μm emission line. Images of the Crab Nebula were obtained on 2001 March 9 using the Ohio State IR Imaging Spectrometer (OSIRIS)[3] mounted on the NOAO Cerro Tololo Inter-American Observatory (CTIO) 1.5 m telescope (see panel (a) of Figure 2.13). OSIRIS has a 1024×1024 NICMOS3 array, with a pixel scale of $1\farcs153$ arcsec using the f/2.8 camera. Only a portion of the array is illuminated, yielding a field of view of $11'$. We used a narrow ($\Delta\lambda/\lambda \simeq 1\%$) filter to image the extended [Fe II] 1.644 μm line emission from the Crab. Six individual exposures of 120 s each were sky subtracted using a median of similar images centered at a position $10'$ south of the Crab (with slight positional offsets between each), and then shifted and co-added.

H-band fluxes from the 2MASS point source catalog for several stars in the field were used to flux calibrate the resulting [Fe II] image. The H-band image from the 2MASS survey was also used to subtract the continuum emission from the synchrotron nebula that is included in the [Fe II] filter, in order to produce a true image of the line emission. While the H-band image is not a pure continuum image (the [Fe II] 1.644 μm line is included in the H band), the broadband image is dominated by synchrotron continuum and the thermal filaments are barely seen; based on the flux of the [Fe II]

[3]OSIRIS is a collaborative project between the Ohio State University and Cerro Tololo Inter-American Observatory (CTIO) and was developed through NSF grants AST 90-16112 and AST 92-18449. CTIO is part of the National Optical Astronomy Observatory (NOAO), based in La Serena, Chile. NOAO is operated by the Association of Universities for Research in Astronomy (AURA), Inc. under cooperative agreement with the National Science Foundation

line, we estimate that it contributes only 2–3% of the total flux in the broad H-band filter.

2.3 Multi-Wavelength Morphology

2.3.1 IRAC and MIPS morphology

IRAC and MIPS images of the Crab Nebula are displayed in Figure 2.5. Panel (a) is a three color visual press release image reproduced courtesy of the European Southern Observatory, showing the Hα filaments that trace out regions of strong hydrogen recombination line emission. The smooth blue background is due to synchrotron radiation from relativistic electrons ejected by the neutron star central engine. Panels (b), (c), and (d) of Figure 2.5 show IRAC 3.6 μm, 4.5 μm, and 5.8 μm images whose emission is dominated by synchrotron emission. Panel (e) of Figure 2.5 shows the IRAC 8.0 μm image, and panels (f) and (g) are MIPS 24 μm and 70 μm images. Images in panels (e), (f), and (g) all show filamentary structure that is dominated by strong forbidden line emission and correlates very strongly with the recombination line filaments traced out in the visual Hα image of panel (a). The NRAO 5 GHz radio image (Bietenholz et al. 2001) is displayed in panel (h) for comparison and it shows both the smooth synchrotron component and the thermal bremsstrahlung in the filaments. The IRAC and MIPS three-color composite image is displayed in Figure 2.6. Blue represents the IRAC 3.6 μm morphology that traces out the synchrotron emission, while the green (8.0 μm) and red (24 μm) map out the [Ar II] 7.0 μm and [O IV] 26 μm emission respectively and trace the filamentary structure seen in Hα. While the south filament is bright in both green and red, the equatorial filament is dominated by MIPS 24 μm emission which may suggest the presence of large dust grains.

The IRAC and MIPS integrated flux densities of the Crab Nebula are displayed in Figure 2.7 and listed in Table 2.1. Uncertainties in the table do not reflect IRAC and

MIPS calibration uncertainties. Extended emission correction was applied to the IRAC integrated flux densities of the nebula based on Reach et al. (2005). Figure 2.7 also includes fluxes in the visible and near IR wavelengths for comparison (Veron-Cetty & Woltjer 1993; Grasdalen 1979; Green et al. 2004). It can be seen from the plot that the IRAC and MIPS fluxes agree well with previous data. The IRAC points trace the synchrotron continuum with a spectral index of 0.5, as derived by Douvion et al. (2001). The excess radiation seen at 24-100 μm above the synchrotron continuum may indicate the presence of a small amount of warm dust in the form of relatively large grains. The excess at 24 μm may also partly be due to forbidden line emission from [O IV]. Some of the excess in the MIPS 70 μm filter may be due to [O I] 63 μm, [O III] 52 μm and [O III] 88 μm (Green et al. 2004).

2.3.2 Central Nebula and the Crab Pulsar

Close up IRAC images of the central part of the Crab Nebula are shown in Figure 2.8. Panel (a) is the *Chandra* X-ray Observatory ACIS-S image (Hester et al. 2002), panel (b) is the HST optical image (Hester et al. 1995), and panels (c) through (f) are IRAC images in order of increasing wavelength. The equatorial torus and polar jets of the X-ray image are clearly visible at all IRAC wavelengths. The position of the point source in the center of IRAC images is coincident with the position of the Crab pulsar in the HST image. The pulsar is not detected in the MIPS images. Additional features identified in the HST image by Hester et al. (1995) are also visible at IRAC wavelengths, including the knot located $3\farcs8$ southeast of the pulsar, aligned with the jet, and the bright arcs (wisps) located $7\farcs3$ northwest of the pulsar.

The spectral energy distribution (SED) of the pulsar is shown in Figure 2.9. The aperture photometry was performed on *Spitzer* images using an aperture radius of $3.6''$, a background annulus of 3.6–$8.4''$, and median sky subtraction. The appropriate aperture correction was applied to the resulting fluxes (see The Spitzer Observers Manual).

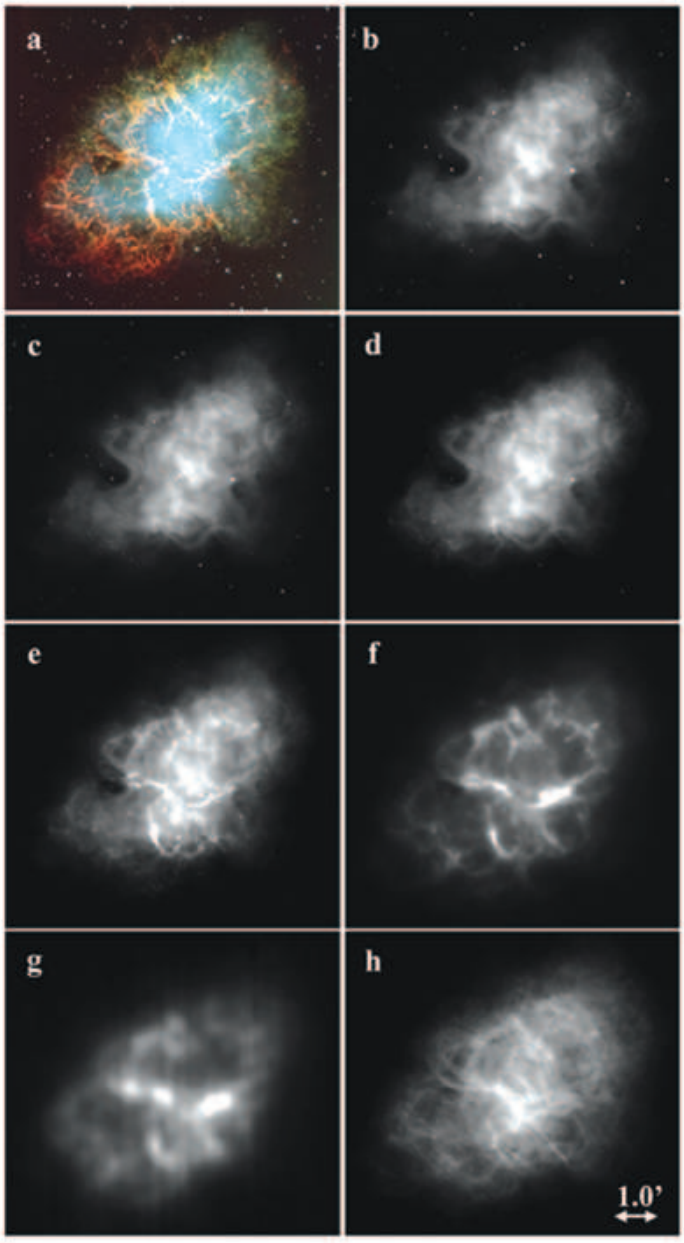

Figure 2.5 A comparison of *Spitzer* IR images of the Crab Nebula with optical and radio images showing that the smooth synchrotron component and the filamentary component dominate the emission at different wavelengths. Panel (a) is a 3 color visual press release image reproduced courtesy of the European Southern Observatory. Panels (b), (c), and (d) show IRAC 3.6 μm, 4.5 μm, and 5.8 μm images that trace out the synchrotron component. Panels (e), (f), and (g) show IRAC 8.0 μm and MIPS 24 μm and 70 μm images that show filamentary structures dominated by strong forbidden line emission. Panel (h) shows that the 5 GHz radio image traces out both the smooth synchrotron component and thermal bremsstrahlung in the filaments (image reproduced courtesy of NRAO/AUI and Bietenholz et al. 2001)

Figure 2.6 *Spitzer* IRAC/MIPS three-color composite image. Blue (3.6 μm) emission maps out the synchrotron component, green (8.0 μm) maps out [Ar II] 7.0 μm emission, and red (24 μm) maps out [O IV] 25.9 μm emission. The color tables are linearly proportional to intensity.

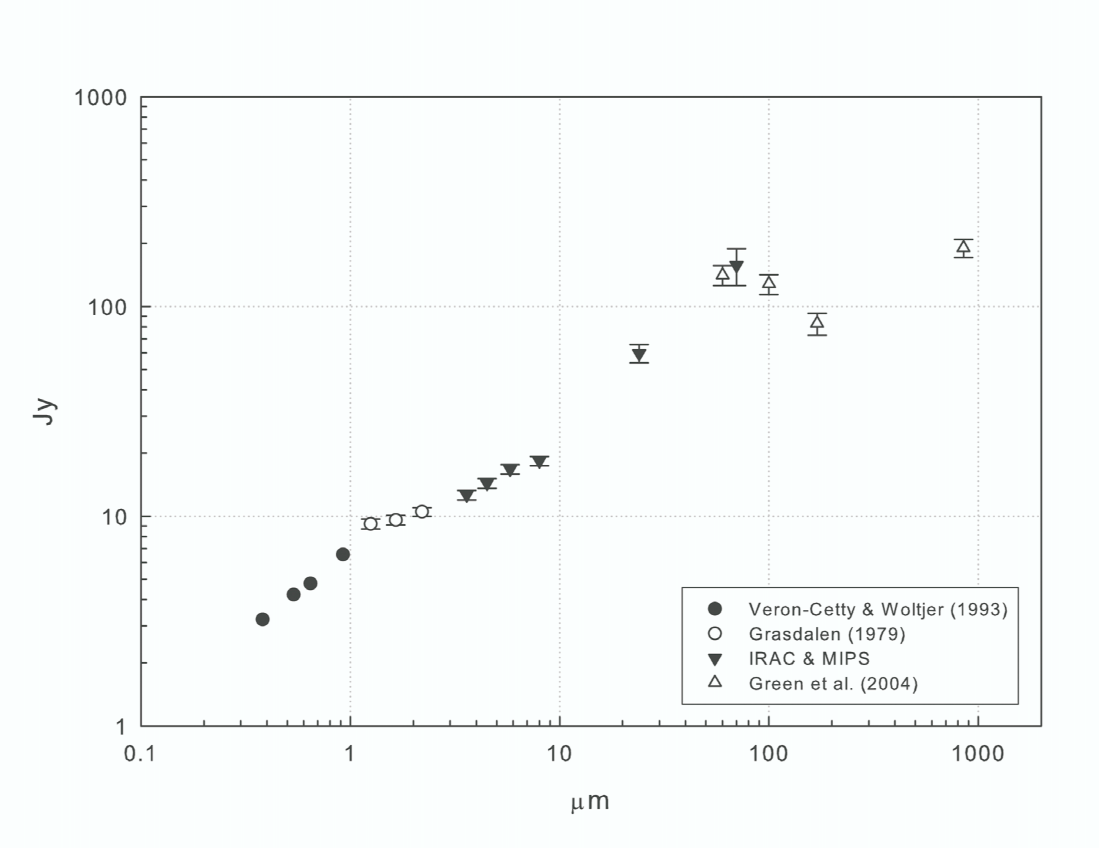

Figure 2.7 Integrated flux density of the Crab Nebula. IRAC wavelengths are corrected for extinction using A_V of 1.5 and the extinction values from Rieke & Lebofsky (1985). Extended emission correction was also applied to the IRAC fluxes (Reach et al. 2005). IRAC and MIPS errors are dominated by flux calibrations uncertainties. The error bars include calibration uncertainties of 5% for IRAC wavelengths, 10% for MIPS 24 μm, and 20% for MIPS 70 μm.

The fluxes likely have additional uncertainties due to high nebular emission around the pulsar, including the IR knot located 0.″6 from the pulsar identified by Hester et al. (1995) and discussed by Sollerman (2003). Visible and near IR points from Table 5 of Eikenberry et al. (1997), in which the visible data comes from Percival et al. (1993), are included in Figure 2.9 for comparison. Table 2.1 summarized the pulsar measurements and does not include calibration uncertainties of roughly 5% at each IRAC wavelength.

2.3.3 IRS/IRAC morphology comparisons

With the long IRS slits in the low-resolution modules it is possible to observe variations in the emission line strengths over the different regions within the nebula sampled by the slits. In general, the IRS long-slit spectra show a relatively spatially smooth synchrotron continuum with much more pronounced spatial structure in the emission line fluxes. These line emission spatial variations can be quite strong and are shown in Figures 2.10 and 2.11, which show the correlation between the emission line strength and the observed IRAC 8 μm spatial structure. It is tempting to infer that the IRAC 8 μm image spatial structure is due to the 7.0 μm [ArII] line emission. As can be seen in the figures, there definitely is some spatial correlation, but compared to the integrated synchrotron emission within the IRAC band the flux in the [ArII] line is relatively low and the variation in the line intensity by itself would not be enough to account for all the observed 8 μm structure. Emission lines at other wavelengths are not necessarily correlated with the structure observed by IRAC. For example Figure 2.11 shows that although the 12.8 μm [NeII] line emission has a peak in the region of strong IRAC 8 μm emission, it also rises in strength in an 8 μm "hole". In addition, the region of strongest IRAC emission corresponds to the lowest [NeII] emission.

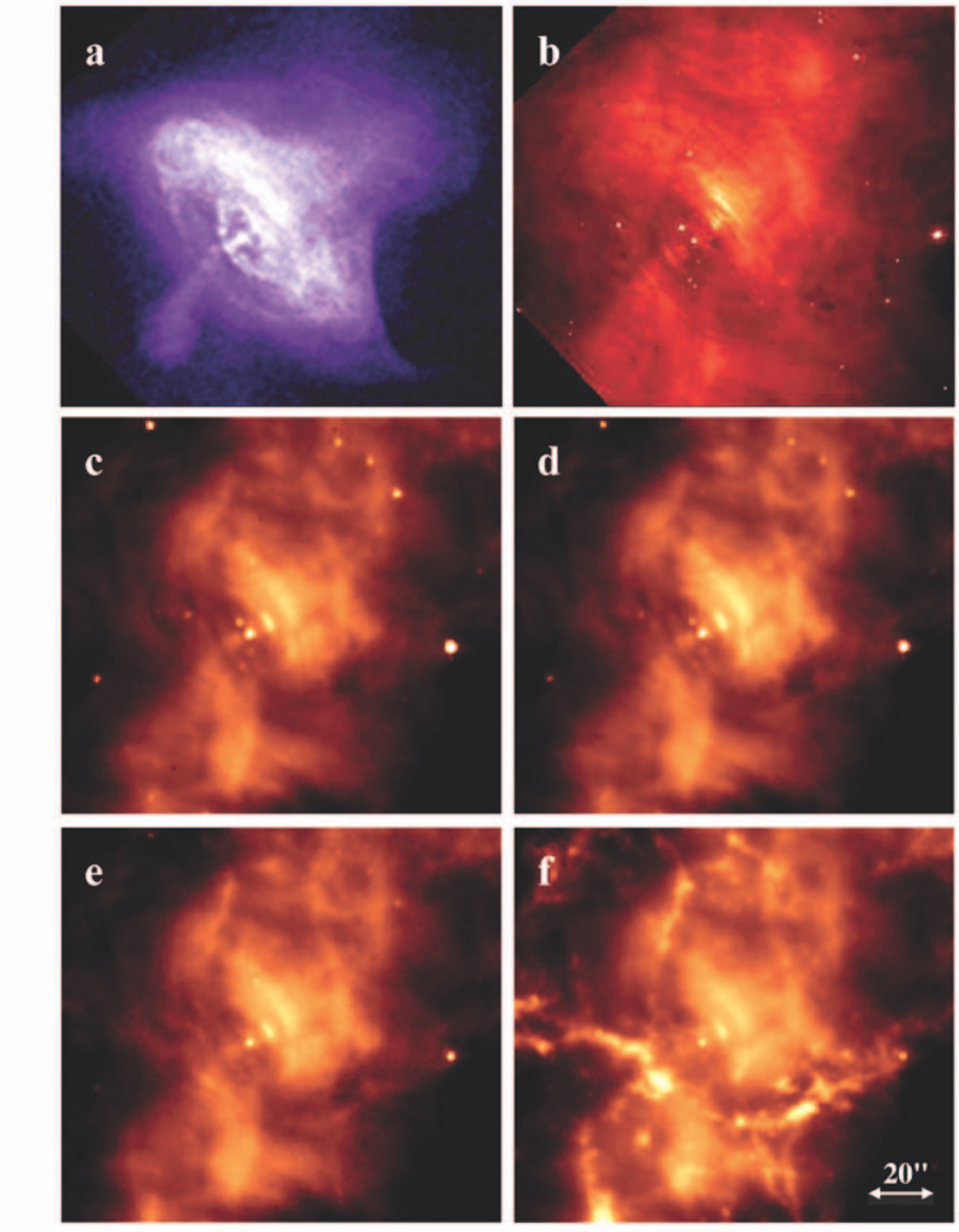

Figure 2.8 Detail of the pulsar central engine and its equatorial torus and polar jets as seen at six wavelengths. The CHANDRA X-ray ACIS-S and HST optical images are reproduced in panels (a) and (b) (Hester et al. 2002). Panels (c), (d), (e), and (f) show the 3.6 μm, 4.5 μm , 5.8 μm, and 8.0 μm IRAC images.

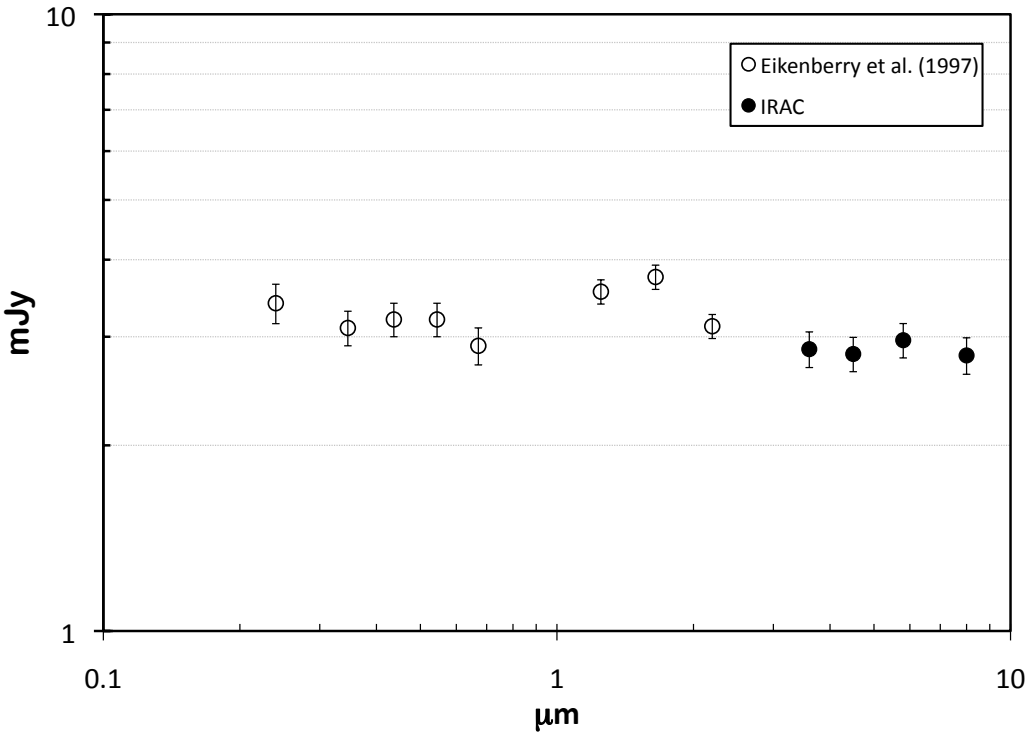

Figure 2.9 The extinction corrected spectral energy distribution of the Crab Pulsar. Extinction correction was computed using Rieke & Lebofsky (1985) and an A_V value of 1.5. The fluxes have been calculated using an aperture size of 3.6″ and a sky background annulus from 3.6″ to 8.4″. The aperture corrections of 1.124, 1.127, 1.143, and 1.234 were applied for IRAC channels 1 through 4, respectively. The IRAC error bars include calibration uncertainties of roughly 5%, but flux values in this plot likely have additional uncertainties due to nebular emission around the pulsar. The near IR and visible data are from Table 5 of Eikenberry et al. (1997), where the visible data come from Percival et al. (1993).

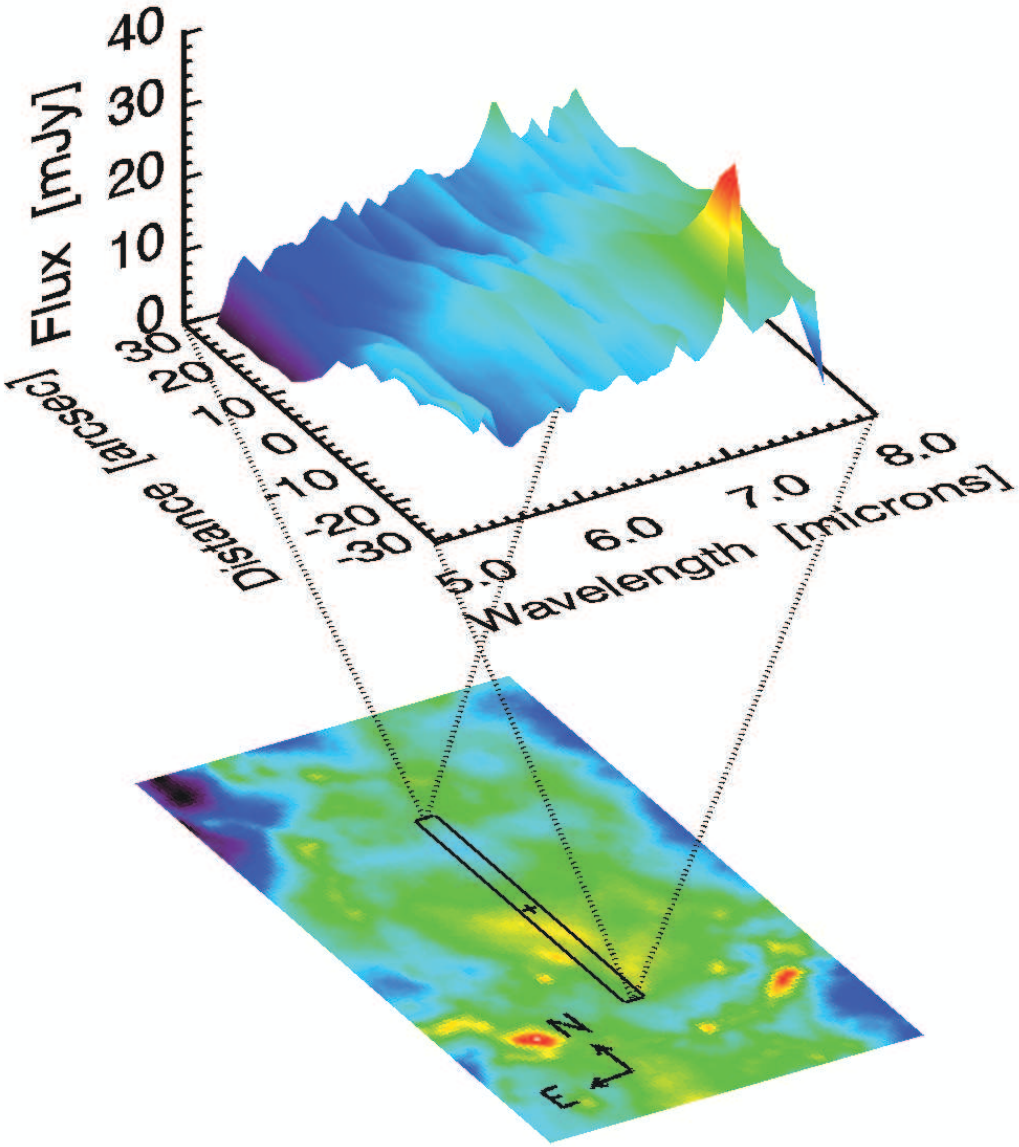

Figure 2.10 The IRS Short-Low second-order spectrum and the IRAC 8 μm image. In this figure the location of the IRS Short-Low second-order aperture is indicated on the IRAC image in the lower part of the figure, with the location of the IRS-Tgt-Cntr position is indicated by a small cross. The spectral dispersion of this spatial cut through the image is shown in the upper part of the figure. The poor correlation of the [ArII] line at 7.0 μm with the IRAC structure is immediately obvious.

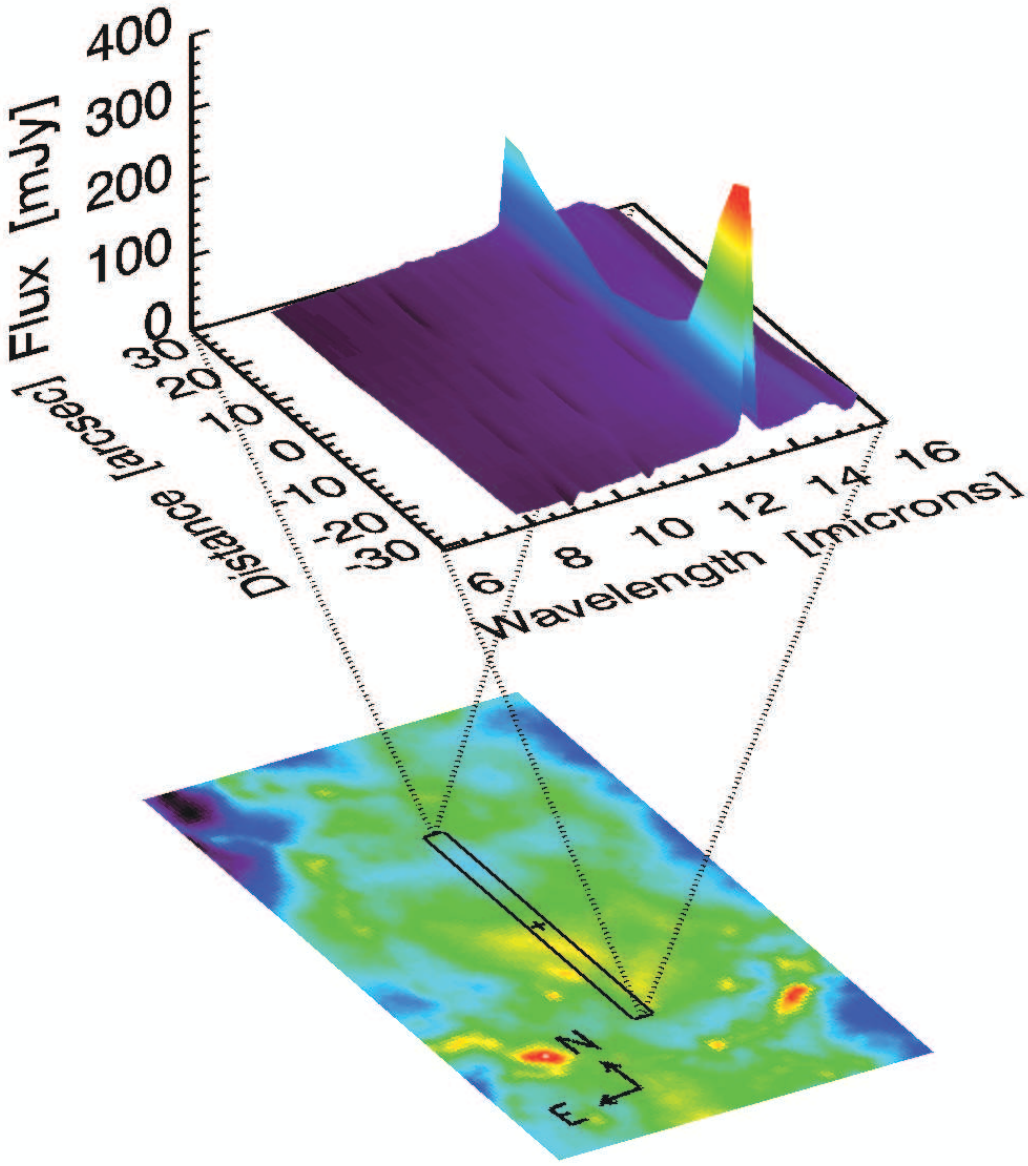

Figure 2.11 The IRS Short-Low first-order spectrum and the IRAC 8 μm image. This figure is the same as Figure 2.10, except that it displays the IRS first-order spectrum. The slit location on the IRAC image is the same for both Short-Low orders. In this case the strong line of [NeII] at 12.8 μm is obvious.

2.4 IRS Spectroscopy

The IRS modules' slits are of different sizes and had different orientations on the Crab (see Fig. 2.3). In order to compare the spectra for the different IRS modules, the smoothness of the synchrotron continuum emission as observed in the IRAC images was used to calculate scaling factors – in the analysis below the IRS observed data were scaled so that their synchrotron continua were in agreement with the levels seen from the Short-Low module. The scaling factors that were employed to achieve this agreement were 0.24 for the Long-Low module, 1.0 for the Short-High module, and 0.33 for the Long-High module. These scaling factors are all larger by approximately a factor of two compared to the ratio of the beam sizes, which indicates that the nebular emission is not completely smooth over these spatial dimensions. Figure 2.12 shows the low and high-resolution spectra after this scaling, with the short and long modules' data combined. The reasons for the slight difference between the synchrotron continuum slopes in the high and low-resolution modules is due to residual uncorrected diffraction effects. The IRS data from the SSC data pipeline is flux-calibrated with point sources. Although corrections have been applied to account for the relatively uniform extent of the synchrotron emission compared to the point-source calibrators, this correction is not perfect.

The fine structure lines observed with the IRS high-resolution modules were fit with Gaussian curves and converted into line strengths. The resultant line identifications, line heights, and line fluxes are given in Tables 2.3 and 2.4. As mentioned above, the synchrotron baseline was used to re-normalize the Long-High module line strengths to correspond to the Short-High module.

The observed spectra show a steadily-rising continuum due primarily to synchrotron emission, and to a lesser extent to the zodiacal background, with various fine-structure emission lines superimposed. As was discussed above, the strength of the fine structure emission lines varies strongly with position within the nebula – for example, the

spectrum at the IRS-Tgt-Cntr position does not show the 7.0 μm [ArII] emission line that is seen strongly in other positions in the nebula. In the high-resolution spectra the emission lines are observed to be split due to Doppler shifts in the front and back sides of the expansion envelope. The average $\Delta\lambda/\lambda$ difference between the front and back shell emission line wavelengths is 0.00843, which corresponds to a shell expansion velocity of 1264 km s^{-1}.

The IRS fine structure emission lines show evidence of high excitation that may be caused by photoionization by synchrotron radiation. For example, we observe emission from [NeV] which has an ionization energy of 97 eV. Given the violence of the Crab expansion, shocks sufficient to excite forbidden lines are also not unexpected. With the large number of fine structure emission lines observed by the IRS, it should be possible in principle to derive electron temperatures and densities from the line ratios. Unfortunately, for all of the lines coming from the same ion, the line pairs appear in different IRS modules. Modules' different aperture sizes, different slit position angles, coupled with the observed spatial structure in the emission line emission regions, result in line ratios that have large and unquantifiable uncertainties. For example, in comparing the measured 15.5 μm/36 μm line ratio for [NeIII], we find ratios of 3.3 $\pm$0.3 for the red-shifted lines, and 5.6 $\pm$0.3 for the blue-shifted lines. For temperatures around 10,000K the predicted ratio for these lines ranges from 11 to 38 for electron number densities ranging from 10 to 10^7 cm^{-3}. Similarly for the 18.7 μm/ 33.4 μm line ratio for [SIII], the measured values for both the red and blue lines are less than the predicted level even for the lowest electron densities. This indicates that there is more line flux entering the Long-High IRS aperture than is expected, even after normalization using the synchrotron continuum baseline. Given the spatial structure that can be seen in the images of the IRS high-resolution module slits this is not surprising – the larger Long-High slit must contain more bright emission knots than does the Short-High slit.

Table 2.3 Crab Nebula: IRS Short-High Data

Line	Wavelength (μm)	Measured Wavelength (μm)	Line Fit Height (Jy)	Line Flux (W/cm^2/μm)
[NeII]	12.8135	12.763 ± 0.001	0.6850 ± 0.0044	4.386 ± 0.043E-20
		12.862 ± 0.001	0.1252 ± 0.0038	8.930 ± 0.048E-21
[NeV]	14.3217	14.261 ± 0.007	0.0123 ± 0.0035	9.325 ± 3.311E-22
		14.404 ± 0.008	0.0099 ± 0.0035	7.851 ± 4.603E-22
[NeIII]	15.5551	15.493 ± 0.001	0.9434 ± 0.0556	4.692 ± 0.039E-20
		15.621 ± 0.001	0.2982 ± 0.0038	1.900 ± 0.039E-20
[SIII]	18.7130	18.648 ± 0.001	0.0475 ± 0.0025	2.533 ± 0.201E-21
		18.777 ± 0.002	0.0483 ± 0.0025	2.452 ± 0.197E-21

Table 2.4 Crab Nebula: IRS Long-High Data

Line	Wave-length (μm)	Measured Wavelength (μm)	Line Fit Height (Jy)	Line Flux (W/cm^2/μm)	Scaled Flux[1] (W/cm^2/μm)
[FeIII]	22.9250	22.801 ± 0.021	0.030 ± 0.009	1.28 ± 0.6 e-21	4.2 ± 1.9 e-22
		23.004 ± 0.024	0.028 ± 0.007	1.73 ± 0.7 e-21	5.7 ± 2.2 e-22
[NeV]	24.3175	24.210 ± 0.005	0.140 ± 0.007	9.33 ± 0.7 e-21	3.1 ± 0.2 e-21
		24.420 ± 0.006	0.114 ± 0.007	6.26 ± 0.6 e-21	2.1 ± 0.2 e-21
[OIV]+	25.8903	25.772 ± 0.006	1.372 ± 0.007	9.13 ± 0.07 e-20	3.08 ± 0.02 e-20
$[FeII]$		25.999 ± 0.006	1.342 ± 0.007	8.28 ± 0.06 e-20	2.73 ± 0.02 e-20
[SIII]	33.4810	33.326 ± 0.002	0.376 ± 0.025	2.07 ± 0.2 e-20	6.8 ± 0.7 e-21
		33.547 ± 0.001	0.479 ± 0.028	2.40 ± 0.2 e-20	7.9 ± 0.8 e-21
[SiII]	34.8152	34.675 ± 0.001	0.780 ± 0.032	3.24 ± 0.2 e-20	1.07 ± 0.07 e-20
		34.934 ± 0.002	0.383 ± 0.033	1.30 ± 0.2 e-20	4.3 ± 0.6 e-21
[FeII]	35.3487	35.194 ± 0.007	Same as below		
		35.455 ± 0.009	0.093 ± 0.015	3.71 ± 2.1 e-21	1.2 ± 0.7 e-21
[NeIII]	36.0135	35.852 ± 0.001	0.865 ± 0.034	2.50 ± 0.2 e-20	8.2 ± 0.6 e-21
		36.138 ± 0.001	0.513 ± 0.031	1.74 ± 0.2 e-20	5.8 ± 0.6 e-21

[1]The uncertainties in the displayed scaled line fluxes are statistical only. There are additional large systematic uncertainties in the scale factor – see the text for details.

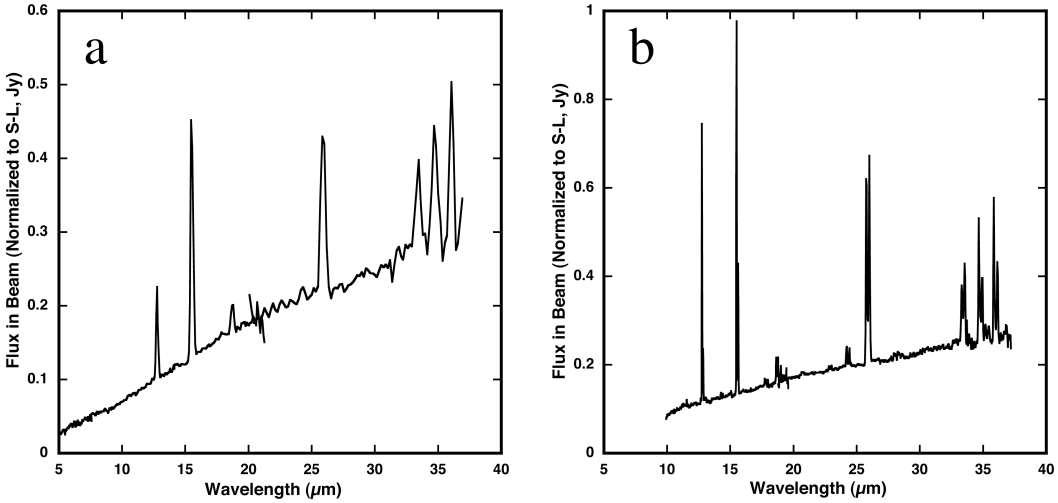

Figure 2.12 The complete low and high resolution spectra of the Crab Nebula at the IRS-Tgt-Cntr location. The fluxes were scaled to the Short-Low module data as described in the text to correct for the different aperture dimensions (§2.4).

2.5 Dust in the Crab Nebula

2.5.1 Line emission or Dust in the MIPS 24 μm Image?

IRS spectra of the Crab discussed above show that a bright emission feature — either [Fe II] 25.99 μm or [O IV] 25.89 μm — contributes significantly to the MIPS 24 μm image. Both lines have been observed in young SNRs and the Crab (e.g., Arendt et al. 1999; Oliva et al. 1999; Green et al. 2004). Figure 2.13 shows the comparison between the MIPS 24 μm image to the ground-based near-IR image of the Crab taken through a narrow filter that isolates [Fe II] $a^4F_{9/2} - a^4D_{7/2}$ at 1.644 μm, with continuum emission subtracted. The major difference between the two images in Figure 2.13 is in the filaments that run east to west across the middle of the remnant; while these filaments appear thin and rather faint compared to some of the brighter [Fe II] 1.644 μm filaments in the north and south of the remnant in Figure 2.13*a*, they are by far the brightest emission features in the 24 μm MIPS image in Figure 2.13*b*. Why are these filaments so much brighter in the MIPS 24 μm image?

An issue of potential concern is whether the narrow bandpass of the 1.644 μm filter cuts-out some of the emission from fast moving filaments that may be Doppler shifted to extreme velocities, because this could cause spurious differences between the MIPS image and the [Fe II] 1.644 μm emission map. However, the observed velocities from the brightest filaments are actually at relatively low velocities in the pinched waist of the Crab. The Doppler shifts are in the range of $\pm$500 to 1200 km s^{-1}, with most filaments moving at $\pm$800 to 900 km s^{-1} (Smith 2003). These velocities are well within the 1% ($\pm$1500 km s^{-1}) FWHM bandpass of the [Fe II] filter. Even if some of the fainter and faster filaments are lost due to their Doppler shifts, it is reassuring that the relative brightness distribution of the filaments is similar to that in previous [Fe II] and other IR emission-line images of the Crab (e.g., Hester et al. 1990; Graham et al. 1990).

Thus, the striking differences in brightness between the various filaments of the Crab

in the [Fe II] 1.644 μm and 24 μm MIPS image are real, and are due either to 1) extreme differences in physical conditions that cause very different relative strengths of [Fe II] 25.99μm and 1.644 μm in certain filaments, 2) differences in ionization level or chemical abundances that cause stronger [O IV] 25.89 μm or weaker [Fe II] emission there, or 3) substantially more warm dust in those filaments.

The flux ratio of [Fe II] 1.644 μm/25.99 μm depends on both electron density and temperature, in the sense that the ratio tends to be larger for higher densities and especially for higher temperatures. The relative strengths of IR lines of [Fe II] can be predicted by quantitative models like those described by Hartigan et al. (2004). In the Crab's filaments, typical electron densities and temperatures derived from optical wavelength diagnostics are $n_e \simeq 1300$ cm^{-3} and $T_e \simeq 11,000 - 18,000$ K (e.g., Fesen & Kirshner 1982; MacAlpine et al. 1989; Davidson & Fesen 1985). Under these conditions, one would expect [Fe II] 1.644 μm to be roughly 3–4 times stronger than the 25.99 μm line. From our flux-calibrated narrow-band image, we measure a total [Fe II] 1.644 μm flux for the whole Crab Nebula of $6.3(\pm1.5)\times10^{-11}$ ergs s^{-1} cm^{-2}. If the average physical conditions quoted above dominate throughout the filaments, the total 25.99 μm flux should be only 1.5–2$\times10^{-11}$ ergs s^{-1} cm^{-2}. The total observed MIPS 24 μm flux density is about 60 Jy ($\sim3\times10^{-10}$ erg s^{-1} cm^{-2} μm^{-1}), and is clearly dominated by emission from the filaments, not the synchrotron continuum (Fig. 2.13*b*). Integrated over the MIPS filter bandpass, the total flux included in the 24 μm filter is then $\sim1.5\times10^{-9}$ erg s^{-1} cm^{-2}. Thus, [Fe II] 25.99 μm should not make much of a contribution to the MIPS 24 μm image (only about 1% of the total flux included in that filter).

On the other hand, if the filaments have cores that are shielded from the UV radiation field of the synchrotron nebula, then the prevailing electron temperatures traced by visual-wavelength diagnostics might not apply, and the expected [Fe II]

1.644 μm/25.99 μm ratio could be very different. For example, if the electron temperature were as low as 1,000–2,000 K in the cores of some filaments, then at the same density of $\sim$1000 cm^{-3} the 25.99 μm line could be more than 1000 times stronger than [Fe II] 1.644 μm. However, under these same conditions, [Fe II] 5.430 μm would be roughly 800 times brighter than [Fe II] 1.644 μm, and almost as strong as the 25.99 μm line. Based on the rather weak 5.34 μm line seen in IRS spectra, and the fact that the "equatorial" filaments are not conspicuous in the IRAC 5.8 μm image, it would seem that the filaments do not contain shielded cool cores at very low temperatures, and therefore, that the majority of the MIPS 24 μm emission is not [Fe II].

Instead, the bright emission feature in the MIPS 24 μm filter is most likely dominated by the [O IV] 25.89 μm line. This agrees with the analysis of the IRS spectra, suggesting that those conclusions are valid across the remnant in areas not covered by the IRS aperture. In visual wavelength spectra, the [O III] λ5007 line is particularly bright in the equatorial filaments, compared to other emission lines (Smith 2003; MacAlpine et al. 1989). Thus, it stands to reason that the much brighter emission from equatorial filaments in the MIPS 24 μm image is due to enhanced [O IV] there as well, either because of higher ionization or enhanced oxygen abundances compared to the other filaments in the Crab Nebula.

Another possibility is that emission from large dust grains in the filaments contributes to the excess equatorial emission seen by MIPS. Green et al. (2004) found that the gas:dust mass ratio in the Crab was comparable to the normal interstellar value, with an upper limit to the dust mass of $\sim$0.2 M$_\odot$. However, the presence of strong line emission in the MIPS 24 μm image makes it difficult to put reliable constraints on the amount of dust, if any, in the Crab Nebula. The MIPS 70 μm image also shows enhanced emission from the same equatorial filaments, which once again, could result from a contribution of either warm dust or [O III] 88.36 μm emission. However, Green

et al. (2004) found that the ISO/LWS spectrum of the Crab was dominated by continuum from dust and synchrotron, not line emission. Thus, the apparent excess far-IR emission above the synchrotron continuum level in the integrated flux density of the Crab (Fig. 2.7) may be due to either dust or line emission.

Whether the bright MIPS emission is caused by excess dust or by stronger high-excitation emission lines, the comparison of the [Fe II] 1.644 μm image and the MIPS 24 μm image reinforces the long-held notion that there is something very different about the "equatorial" filaments that run east–west across the middle of the Crab Nebula. These are the same filaments that are known to have different chemical abundances than the rest of the Crab – most notably a higher He/H abundance (e.g. Uomoto & MacAlpine 1987; Fesen & Kirshner 1982). One hypothesis is that the SN exploded into a pre-existing circumstellar ring, much like the ring around SN 1987A (Sugerman et al. 2002) or the ring that is thought to have been swept up by the Crab-like SNR 0540-69.3 in the LMC (Morse 2006). Indeed, the filaments that bisect the Crab seem to connect the dark bays of the synchrotron nebula, which were presumably formed as the expanding PWN was pinched by an equatorial disk or ring (Fesen et al. 1992). Additionally, the global kinematics of the Crab's shell, traced best in [O III] emission, seem to be bipolar, with a pinched waist coinciding with these "equatorial" filaments (MacAlpine et al. 1989; Smith 2003). Finally, the mysterious northern "jet" or "chimney" (Chevalier & Gull 1975; Gull & Fesen 1982) runs along an axis perpendicular to this putative equatorial ring. Taken together, these clues may suggest that the Crab's progenitor star had a rotation axis oriented roughly north/south, and that the axis changed dramatically during the SN explosion to match the currently-observed axis of the pulsar's jet at about –45°.

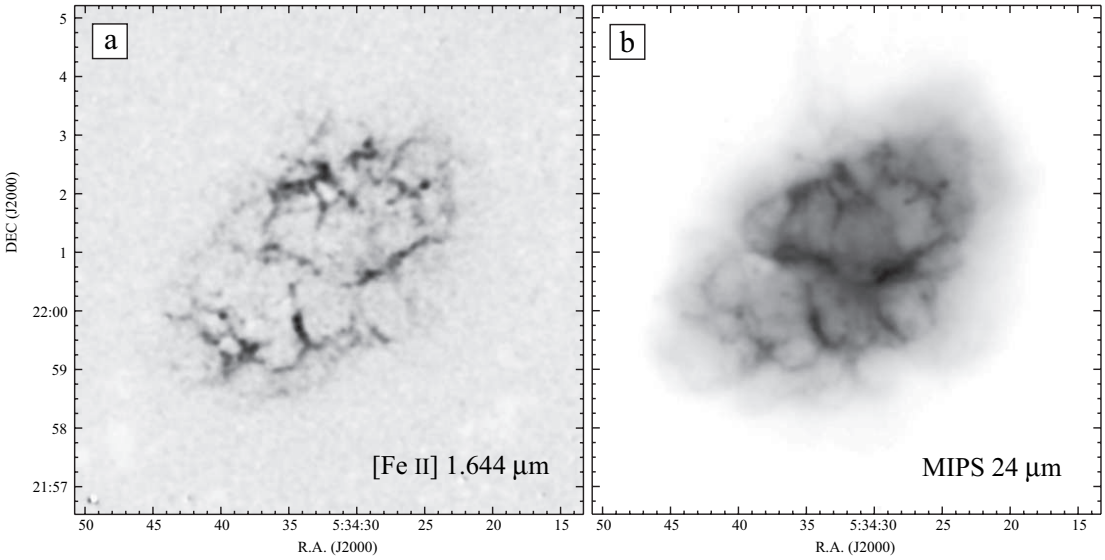

Figure 2.13 Comparison of the optical image made in the light of [Fe II] in panel (a) with MIPS 24 μm image in panel (b).

2.5.2 Estimate of Dust Mass

The presence of the bump between 24 μm and 100 μm in the integrated flux density of the Crab Nebula may suggest that there is a small amount of dust present in the nebula (see Figure 2.7). In order to estimate a rough upper limit on the dust mass that may account for this IR excess, an estimate of the contributions from line emission and synchrotron continuum was removed from the total flux.

Green et al. (2004) found that the excess in the ISOPHOT fluxes between 60 μm and 100 μm can be explained by a small amount of warm dust corresponding to 0.01–0.07 $M_\odot$ of silicates at 45 K or 0.003–0.02 $M_\odot$ of graphite at 50 K. Following the method of Green et al. (2004), the extrapolated synchrotron continuum was subtracted from the MIPS 24 μm and 70 μm fluxes based on the synchrotron power law $25.9(\nu/18.7 \text{ Thz})^{-0.5}$ given by Green et al. (2004) and derived by Douvion et al. (2001) from the ISOCAM mid-IR spectro-imaging observations. Based on the ISO spectra, Green et al. (2004) also found that the line emission contribution to the 60 and 100 μm fluxes is 8 % and 7 %, respectively. Since ISO spectra show no additional emission lines centered at 70 μm, the upper limit on the contribution from line emission to the 70 μm integrated flux is on the order of 7 %, corresponding to $\sim$ 11 Jy. The main difficulty arises in estimating the contribution from line emission to the 24 μm flux. After integrating the IRS spectrum over the MIPS 24 μm bandpass, the contribution from line emission to the total flux in the beam is found to be approximately 5 %. For the purpose of estimating a rough upper limit on the dust mass, this ratio was applied to the total integrated flux at 24 μm, which gives a line contribution of $\sim$ 2.8 Jy. Since the strength of line emission in the Crab has a strong spatial dependence and peaks along the filaments, this assumption most likely significantly underestimates the amount of line emission at 24 μm. The IRS spectrum used for the estimate is centered on a region near the center of the nebula that does not include any filaments.

After subtracting the synchrotron continuum and line emission from the MIPS 24

μm and 70 μm data, and ISOPHOT 60 μm and 100 μm data from Green et al. (2004), a blackbody distribution was fitted to the residual flux densities. The resulting blackbody distribution peaks at a temperature of $\sim$ 74 K, with $(\lambda F_\lambda)_{max} \sim 6.28\times10^{-9}$ erg s^{-1} cm^{-2}. We expect that these values are highly uncertain due to the sensitivity of the blackbody fit to the 24 μm data point. A dust mass was calculated using the following relation

$$M_d = \frac{1.36(\lambda F_\lambda)_{max} a \rho 4\pi d^2}{3\sigma T_d^4} \tag{2.1}$$

where a is the grain size, ρ is the grain density, d is the distance to the Crab Nebula, and T_d is the dust temperature (Gehrz et al. 1998). Assuming a grain size of 10 μm, graphite grains ($\rho = 2.25$ gm cm^{-3}), and a distance of 2.1 kpc, a dust mass of $\sim$ 0.001 M$_\odot$ was derived. Due to the unknown line contribution to the 24 μm flux, this number is only a rough estimate of the dust mass. If one assumes that the excess emission at 24 μm is dominated by line emission and that the blackbody peaks at the 70 μm data point, the total dust mass is 0.004–0.010 M$_\odot$ for graphite grains and 0.006–0.015 M$_\odot$ for silicates.

2.6 Synchrotron Spectra of the Crab Nebula

IRAC 3.6 μm and 4.5 μm images are dominated, for the Crab, by the synchrotron emission that has been observed from radio through X-ray frequencies, with only little evidence for the filamentary line emission seen, e.g., in IRAC 8 μm or in the MIPS 24 μm images. The very hard (flat) radio spectra in PWNe (i.e., filled-center SNRs) like the Crab imply correspondingly hard relativistic electron distributions; the origins of these are still unknown (Nodes et al. 2004). Studies of the variation of the spectral index, $\alpha_\lambda(RA, Dec)$ i.e., the local slope of the synchrotron spectrum, as a function of both frequency and position in the remnant, provide the key data necessary to understand

both relativistic particle acceleration and loss processes.

The spectral index as a function of position was examined using IRAC 3.6 μm and 4.5 μm images, as shown in Figure 2.14. Note that the emission associated with the jet and torus is flat (red) and extends far from the pulsar with little or no steepening visible. The underlying nebular emission progressively steepens with distance. This steepening away from the jet and torus is also seen in the power law indices derived by Willingale et al. (2001) from XMM-Newton observations around 2 keV. At present, it is not possible to determine whether this steepening is with distance from the pulsar or distance from the jet; this distinction is physically important for understanding the acceleration and transport of relativistic particles. The absolute values of the spectral indices would be uncertain by approximately ± 0.3 if we estimate that the calibration uncertainties in each of the IRAC bands are approximately 5%. However, the integrated fluxes between 3.6 μm and 4.5 μm yield a spectral index similar to the derived value of 0.5 by Douvion et al. (2001), and therefore the calibration errors are not included in the discussion below. Any uncertainties in the overall spectral index do not affect the spatial variations in the indices as seen in Figure 2.14.

The overall shape of the synchrotron spectrum was examined by mapping it into "color-color" space, using the technique described by Katz-Stone et al. (1993). In this method, information at optical wavelengths was added, and then $\alpha_{IR}(RA, Dec)$ vs. $\alpha_{opt}(RA, Dec)$ plotted for all positions in the Crab. This plot is then compared to various fiducial spectral shapes to determine the underlying broadband shape of the synchrotron spectrum. This method provides a powerful way to map out the synchrotron spectrum in detail, although measurements are available at only a small number of wavelengths. It is based on the *ansatz* that the *shape* of the relativistic electron distribution is constant throughout the nebula; spatial variations in magnetic field strength and in the degree of adiabatic and radiative losses then lead to spatial variations in the observed spectral index.

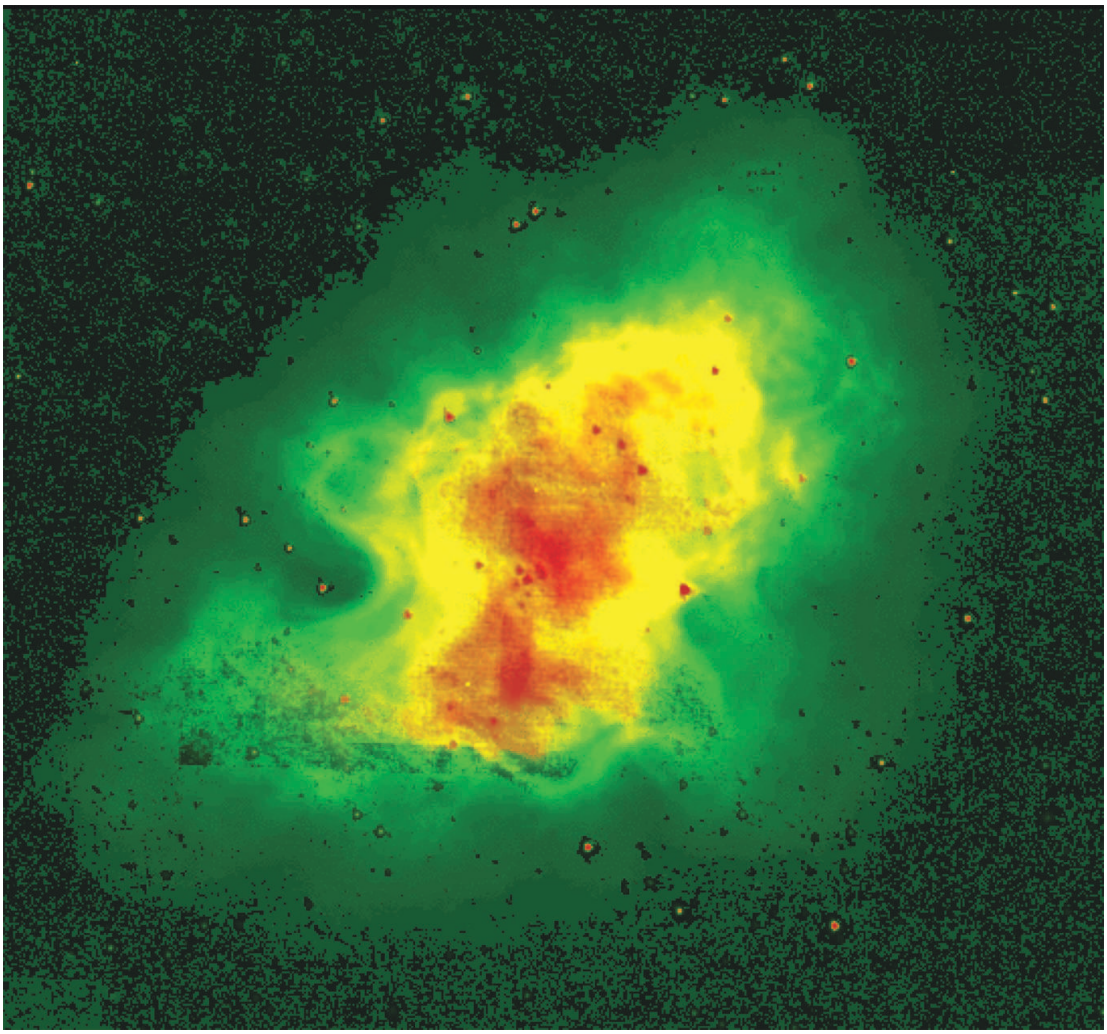

Figure 2.14 The synchrotron spectral index distribution is shown in color, with the local intensity from the IRAC 3.6 μm image. Note the flat spectrum emission from the torus and jets extends far from the pulsar. Red (green) corresponds to spectral indices of 0.3 (0.8).

The first *color-color* diagram is shown in Figure 2.15, which uses the visual spectral indices from Veron-Cetty & Woltjer (1993), who calculated the mean spectral index in 10″ boxes between 9241 Å and 5364 Å to compare with equivalent 10″ box spectra calculated from IRAC 3.6 μm and 4.5 μm images. The IRAC fluxes were corrected for extinction using the interstellar extinction values from Rieke & Lebofsky (1985) and an adopted value for A_V of 1.5. The combination of statistical errors of approximately 1% in each band and variations in inhomogeneities between different lines of sight together are responsible for the scatter of the data around the best fit spectral shape.

Comparison of the color-color data with fiducial homogeneous spectral models shows that these models are not adequate in describing the data. Two standard spectral shapes are shown for comparison – the JP (Jaffe & Perola 1973) model in which relativistic electrons are continuously isotropized in pitch angle, leading to an exponentially cutoff spectrum at high energies, and the KP (Kardashev 1962) model where losses lead to an anisotropic pitch angle distribution, and a high frequency power law. Each spectral model is anchored to the 0.3 spectral index observed throughout the nebula at radio frequencies (Swinbank 1980). Here, it can be seen that both the JP exponential cutoff, and KP spectral shapes are ruled out by the relationship between the optical and IR fluxes. This conclusion is not affected by the calibration errors discussed above; these simply result in a uniform translation of the data in the color-color plane, and would still not agree with the models.

Although a completely new relativistic electron distribution could be derived to fit the data, a much simpler alternative is to explore simple combinations of the standard spectra. We show one such combination in Figure 2.15, a *hybrid* model representing the presence of two KP spectra at each position. The two spectra shown here have cutoff frequencies (low frequency brightnesses) in the ratios of $3 : 1 (1 : 1.8)$. These particulars are not relevant, since there are a variety of spectral combinations, with different numbers of components, cutoff frequencies, normalizations, etc., that could

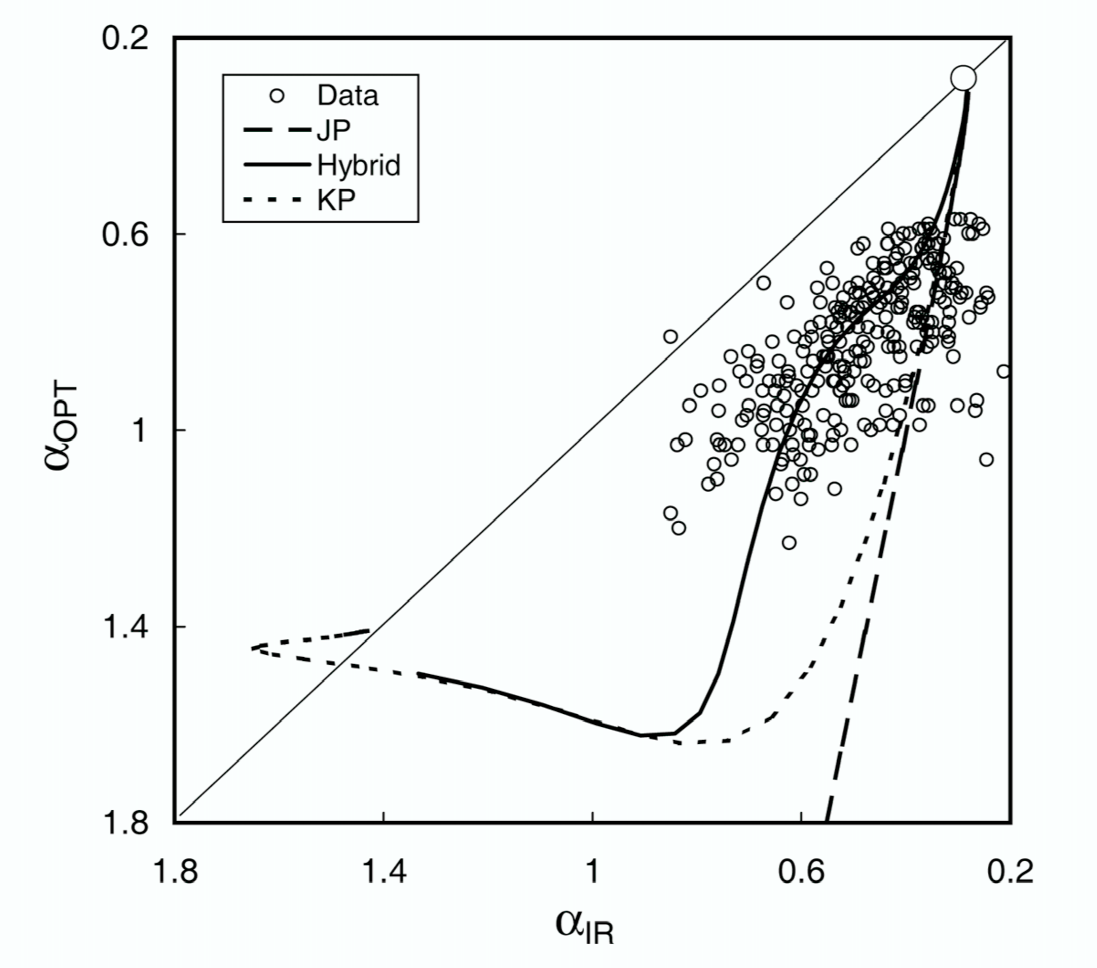

Figure 2.15 Color-color diagram, representing spectral indices in 10″boxes in the IR, and between the IR and optical, as discussed in the text (§2.6).

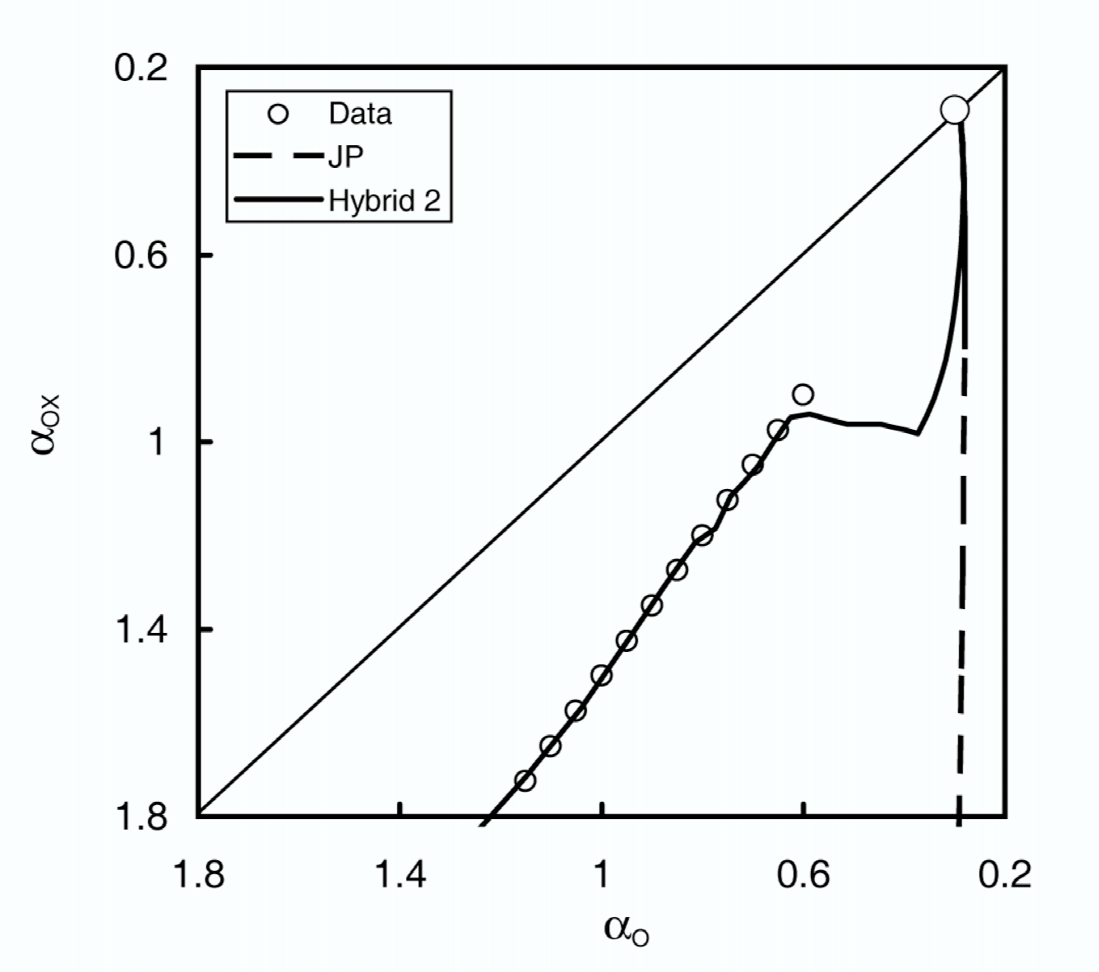

Figure 2.16 Color-color diagram comparing the optical spectral indices to those in the X-ray, as described in the text (§2.6).

equally well fit the data. However, they all point to some inhomogeneities along the line of sight which smear out the spectrum (reduce its curvature) in the optical-IR regime.

In the Crab, the inhomogeneity indicated by the spectral shape likely arises from the superposition of the jet and torus onto the larger nebula. This can be be seen by subtracting IRAC 3.6 μm image from the 5.8 μm image, with the resulting emission seen in Figure 2.18. The most striking thing in this image is the absence of the torus and jet regions that dominate the emission in both bands. This is due to the flatter nature of those regions, which extend over large distances in the nebula. Thus, the data are consistent with emission that shows little or no spectral steepening with distance from the pulsar, superposed on the rest of the nebula, which does steepen. The existence of these two components was suggested by Bandiera et al. (2002) in their comparison between 20 cm and 1.3 mm images. Green et al. (2004) disagreed with these conclusions based on their SCUBA 850 μm images, but their data also show excess flattening due to superposed components. The fact that the torus and jet remain flat to higher frequencies than the rest of the nebula makes them much more prominent in IR, optical and X-ray images, compared to those in the radio (Bietenholz et al. 2004). It also means that sophisticated models will be necessary to understand the acceleration and transport of relativistic particles throughout the nebula.

To explore the higher energy end of the spectrum, a second color-color diagram was used, now relating the optical spectral indices to those between the optical and X-ray, as presented by Bandiera et al. (1998). For the data, the trend line between $0.8 < \alpha_{opt-X} < 1.75$ was used which can be represented as $\alpha_{opt-X} = 1.5 \times \alpha_{opt}$. The very weak X-ray data with $\alpha_{opt-X} > 1.75$ (above line (c) in their Figure 3) was considered to be unreliable because it shows no correlation with the optical spectral indices. Note that the detectable X-ray synchrotron nebula is considerably smaller than at lower frequencies. The α_{opt} vs. α_{opt-X} data line (represented by a series of open

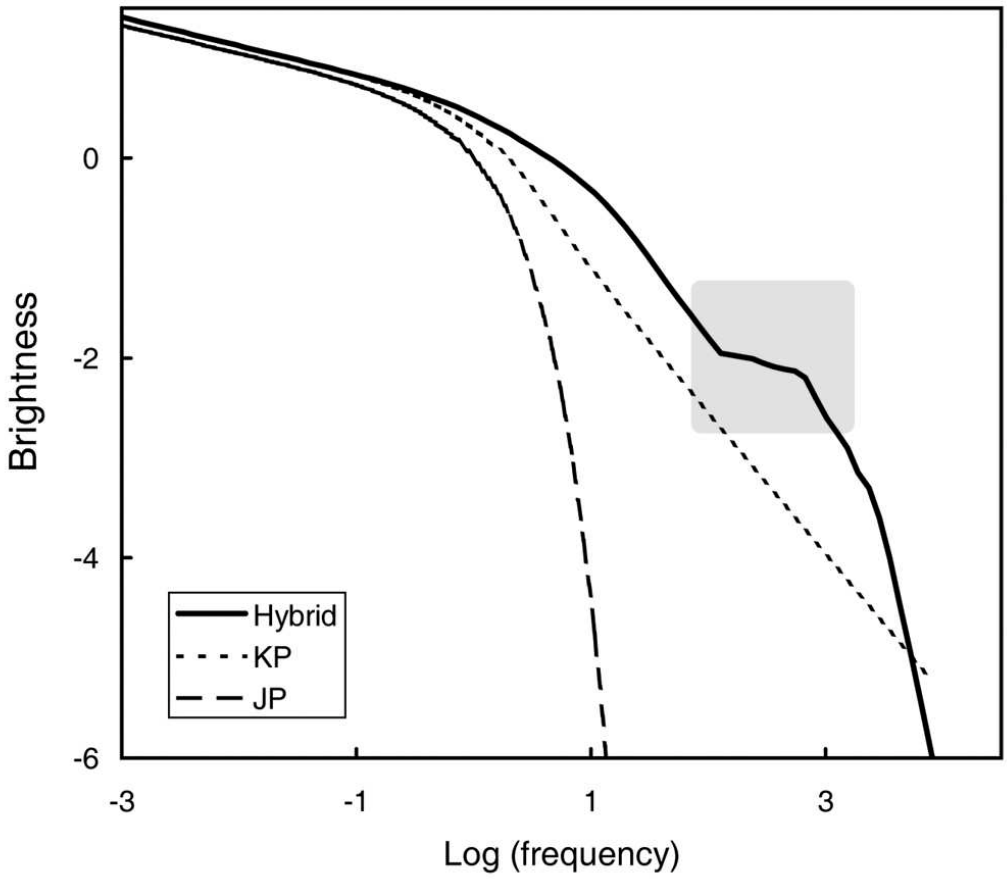

Figure 2.17 The derived shape for the broadband synchrotron spectrum of the Crab, as shown in color-color space in the previous two figures. The shaded box indicates where the details of the shape are not determined.

circles) and spectral shape models are shown in Figure 2.16.

Neither the JP or KP models, nor the hybrid model developed above can explain this shorter wavelength data. The basic problem is that an exponential cutoff is needed, but it cannot follow a standard JP shape, because any spectral steepening seen in the IR would predict X-ray fluxes orders of magnitude lower than observed. So the exponential cutoff must somehow be pushed out to shorter wavelengths than expected. Such a model was empirically constructed by modifying the optical/IR *hybrid* to introduce a *bump* just below the X-rays, followed by an exponential cutoff. This empirical model is labeled as hybrid 2 and shown both in color-color space (Figure 2.16) and in normal log(brightness) *vs* log(frequency) space in Figure 2.17. It starts at long wavelengths (low energies) with the radio spectral index and fits the variations in the IR-optical and optical-X-ray spectral indices.

Although this model is not unique, it has two characteristics that must be present in any model that fits the data. First, the spectra cut off very rapidly (possibly exponentially) in the X-ray regime, indicative of strong radiative losses. Second, there needs to be a *bump* in the spectrum somewhere in the ultraviolet. The shaded box in Figure 2.17 shows the region of uncertainty from our analysis; no direct measurements are available here. However, without some fairly abrupt offset to the smooth spectral shape, models including X-ray data would fail as badly as the JP and KP models shown in Figure 2.16. Such an offset or bump in the spectrum is expected due to the pileup of relativistic electrons that result from energy losses at higher energies (e.g. Reynolds 2003), when the low frequency spectral index is flatter than 0.5, as is true for the Crab. To our knowledge, there has not been any previous observational evidence for this pileup.

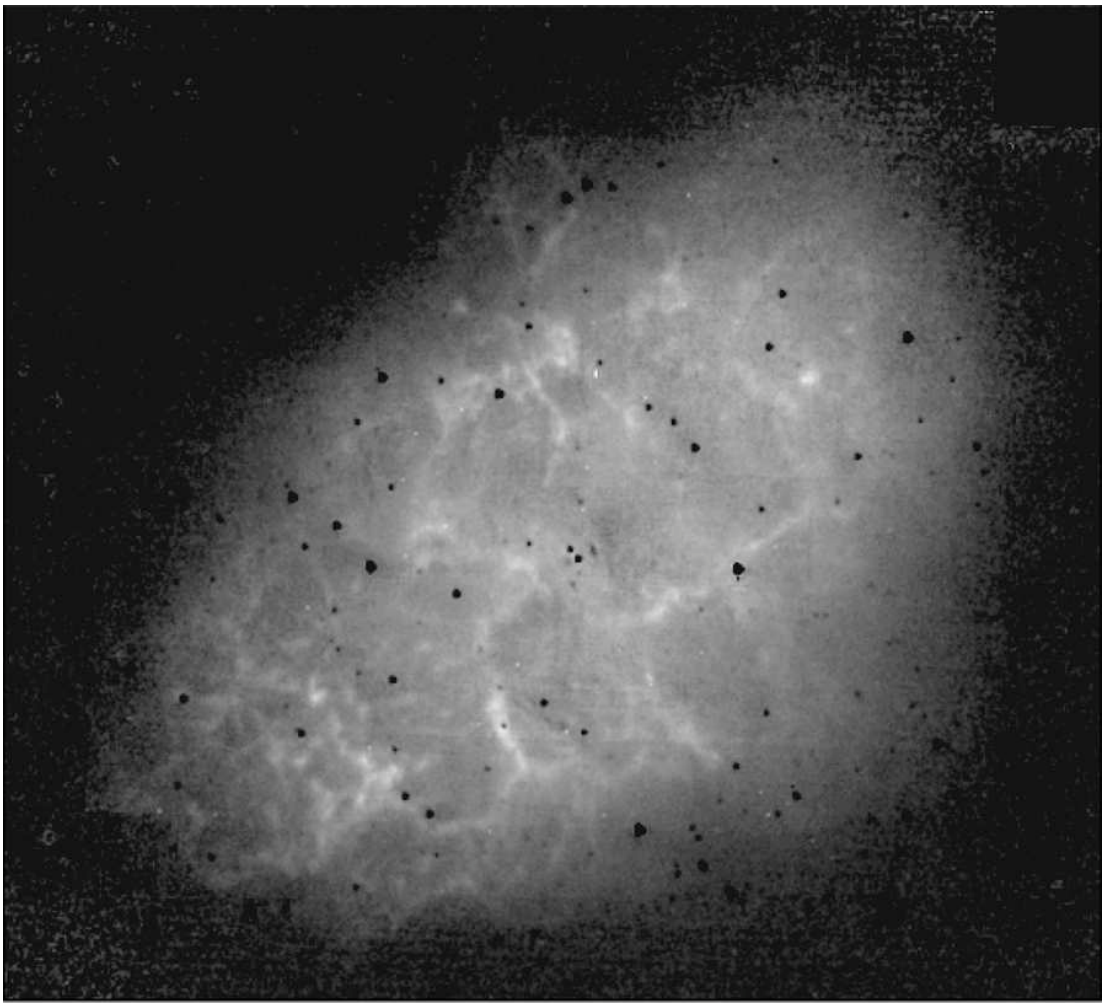

Figure 2.18 This figure shows the difference between IRAC 3.6 μm and 5.8 μm images, where the 3.6 μm image has been scaled by a factor of 1.3. Note that the jet and torus, which are prominent in the original images are gone.

2.7 Conclusions

The following is a brief summary of the main conclusions presented by the *Spitzer* Space Telescope IR imaging and spectroscopic observations of the Crab Nebula:

1. A comparison of the morphology from the x-ray to the radio shows that the synchrotron component and filaments dominate at different wavelengths.

2. A broadband shape to the synchrotron spectrum was derived and it shows evidence for multiple components along the line of sight, likely due to the torus and jet which remain flat to large distances from the pulsar, superposed on the broad nebular emission that steepens with increasing distance. At shorter wavelengths, the derived spectral shape is consistent with the expected pileup of relativistic electrons just below an exponential cutoff in X-rays.

3. The flux density of the nebula and the pulsar was measured. The smooth background of the nebula and the pulsar are dominated by synchrotron emission and a large fraction of the emission from the filaments in the images is due to forbidden line emission from Ar, Ne, O, and Fe.

4. There is a paucity of dust in the Crab Nebula. The small grain component seems to be missing entirely and we see no evidence for silicate emission. The total emission at long wavelengths from large grains implies a total dust mass in the nebula of less than 1% of a solar mass.

5. In the IRS spectra, Doppler shifted emission from both the front and back sides of the expanding shell are seen, and a radial expansion velocity of roughly 1264 km s^{-1} was measured.

Chapter 3

X-ray Observations of G54.1+0.3 and IR Spectroscopy of the Associated Shell

ABSTRACT

Recent *Spitzer* IR observations of G54.1+0.3 revealed an IR shell that contains a dozen point sources arranged in a ring-like structure. An extended knot of emission located in the SW part of the shell appears to be aligned with the pulsar's X-ray jet, suggesting a possible interaction with the shell material. Surprisingly, the IRS spectrum of the knot resembles the spectrum of freshly formed dust in Cas A, and is dominated by an unidentified dust emission feature at 21 μm. The spectra of the shell also contain various emission lines and show that some are significantly broadened, likely due to swept-up SN ejecta. We present the first evidence that the PWN is driving a shock into expanding SN ejecta and we propose an alternative explanation for the origin of the IR emission in which the shell is composed entirely of SN ejecta. In this scenario, the freshly formed SN dust is being heated by early-type stars belonging to a cluster

in which the SN exploded. Simple dust models show that this interpretation can give rise to the observed shell emission and IR point sources.

This work was carried out under the supervision of Patrick Slane (Harvard-Smithsonian Center for Astrophysics),and in collaboration with Stephen Reynolds (North Carolina State University), John C. Raymond (Harvard-Smithsonian Center for Astrophysics), and Kazimierz J. Borkowski (North Carolina State University). The results have been submitted for publication in the Astrophysical Journal.

3.1 Introduction

G54.1+0.3 is a young PWN, closely resembling the Crab, for which no thermal shell emission has been detected in X-rays. It appears to be in the early stages of its evolution in which the nebula sweeps-up the freely expanding SN ejecta, but there have been no previous detections of an interaction of this PWN with the ejecta material. The study described in this chapter provides the first direct evidence that this PWN is driving a shock into the SN ejecta and freshly formed SN dust. In addition, the environment into which the SNR is expanding provides a unique opportunity for the study of SN dust that has not yet been reached by the reverse shock.

The properties of G54.1+0.3 are very similar to those of the Crab Nebula. Radio observations show a nebula with a flat spectrum, approximately $2'$ in extent (Reich et al. 1984; Green 1985; Velusamy & Becker 1988), and no evidence of the SNR shell. While the extent of the X-ray nebula in the Crab is 3 times smaller than in the radio, non-thermal X-ray emission from G54.1+0.1 extends out to the radio boundary (Seward 1989; Lu et al. 2001). *Chandra* observations revealed a point source surrounded by a ring and torus, and a nebula elongated in the E/W direction (Lu et al. 2002). All components have a power-law spectrum with an index steepening with increasing distance from the pulsar. There is no evidence for a thermal component associated with SN ejecta or the

swept-up ISM.

The 137 ms pulsar that powers the nebula was discovered by Camilo et al. (2002), who calculate a characteristic age of 2900 yr. Considering a possible range of braking indices and initial spin periods, Camilo et al. (2002) estimate the age of G54.1+0.3 to be between 1500 and 6000 yr. From the equations describing PWN evolution, Chevalier (2005) calculates an age of 1500 yr and and an initial spin period P_0 of 100 ms. Based on HI line emission and absorption measurements, the distance to G54.1+0.3 is in the 5–9 kpc range (Weisberg et al. 2008; Leahy et al. 2008), while the pulsar's dispersion measure implies a distance less than or equal to 8 kpc (Camilo et al. 2002). Leahy et al. (2008) recently suggest a morphological association between the nebula and a CO molecular cloud at a distance of 6.2±0.1 kpc.

While there has been no previous evidence for an interaction of the PWN with SN ejecta, circumstellar material (CSM), or the ISM in G54.1+0.3, a recent *Spitzer* discovery of an IR shell surrounding the PWN may be the first evidence of such an interaction (Slane 2008; Koo et al. 2008). The first IR detection from G54.1+0.3 was made with the IRAS at 25 μm, 60 μm, and 100 μm, and the emission was consistent with a cold dust component with a temperature of $\sim$ 30 K (Arendt 1989; Saken et al. 1992). *Spitzer* imaging revealed an IR shell surrounding the PWN in which a dozen point sources are arranged in a ring-like structure, suggested to be young stellar objects (YSOs) whose formation was triggered in the late stages of the progenitor's life (Koo et al. 2008). The morphological association between G54.1+0.3 and the shell is evident in the IR images and suggests that the PWN may be interacting with the shell material. The nature of the shell still remains unclear. While the morphology suggests that the shell is SN ejecta and freshly formed dust swept up by the PWN, presence of YSOs would require that it is a preexisting circumstellar shell or a molecular cloud. This chapter presents deep *Chandra* imaging of G54.1+0.3 and *Spitzer* IR imaging and spectroscopy of the associated shell that provide new insight into its origin.

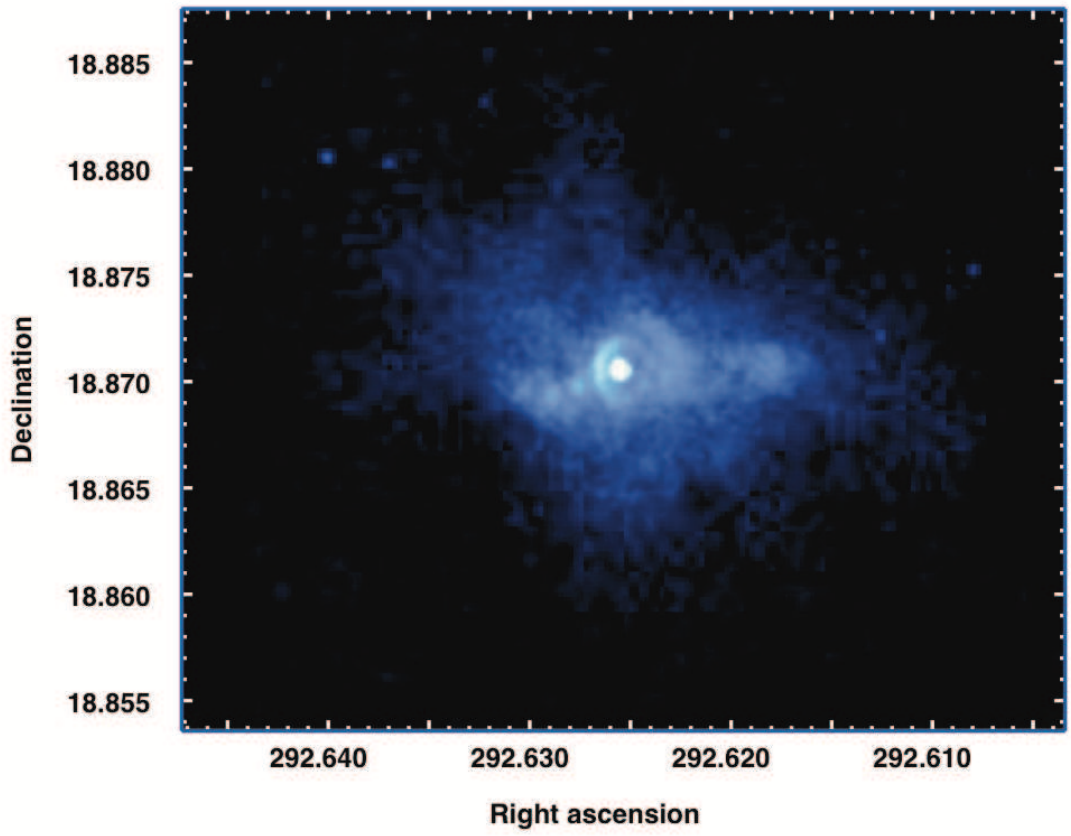

Figure 3.1 Chandra ACIS image of G54.1+0.3 in the 0.3–10.0 keV band.

3.2 Observations and Data Reduction

3.2.1 Chandra

Observations of G54.1+0.3 were taken with the Advanced CCD Imaging Spectrometer, ACIS-S, on board the *Chandra* X-ray observatory on 2008, July 8, 10, 12, and 15, under the observation ID numbers 9886, 9108, 9109, and 9887. The observations were carried out using the FAINT mode and the corresponding exposure times were 66.17, 35.11, 164.33, and 25.16 ks, for a total exposure time of 290.77 ks. The standard data reduction and cleaning were performed using Ciao Version 3.4.

The cleaned *Chandra* datasets were merged into a single event file using the *merge_all* task in *Ciao* version 3.4. The final merged image is shown in Figure 3.1. Spectra were extracted from the merged file from eight different regions covering the PWN and one background region. The extraction regions are similar to those in Lu et al. (2002) for the purpose of comparison, and are shown in Figure 3.2. Because the observations were carried out close in time and have the same chip orientations and positions on the sky, the corresponding effective area and spectral response files were generated from a single observation with ID 9109. Source spectra were background subtracted and grouped to include a minimum of 75 counts in each bin for region 1, 50 counts in each bin for regions 2, 3, 4, 7, and 8, and 20 counts in each bin for regions 5 and 6.

3.2.2 Spitzer

IR spectroscopy was carried out with all modules of the IRS (Houck et al. 2004) aboard *Spitzer* on 2007, Nov. 05, covering the 5-37 μm wavelength range (program ID 40736). The positions of the slits are shown in Figure 3.3. The low resolution spectra were taken at position 19h30m28.0s, $+18^{\circ}52'15.60''$(J2000), centered on the diffuse shell emission, but also covering the bright knot in the northwest with the long-low (LL) module. The low resolution observations had 5 cycles for each module, with an exposure time of 14 s

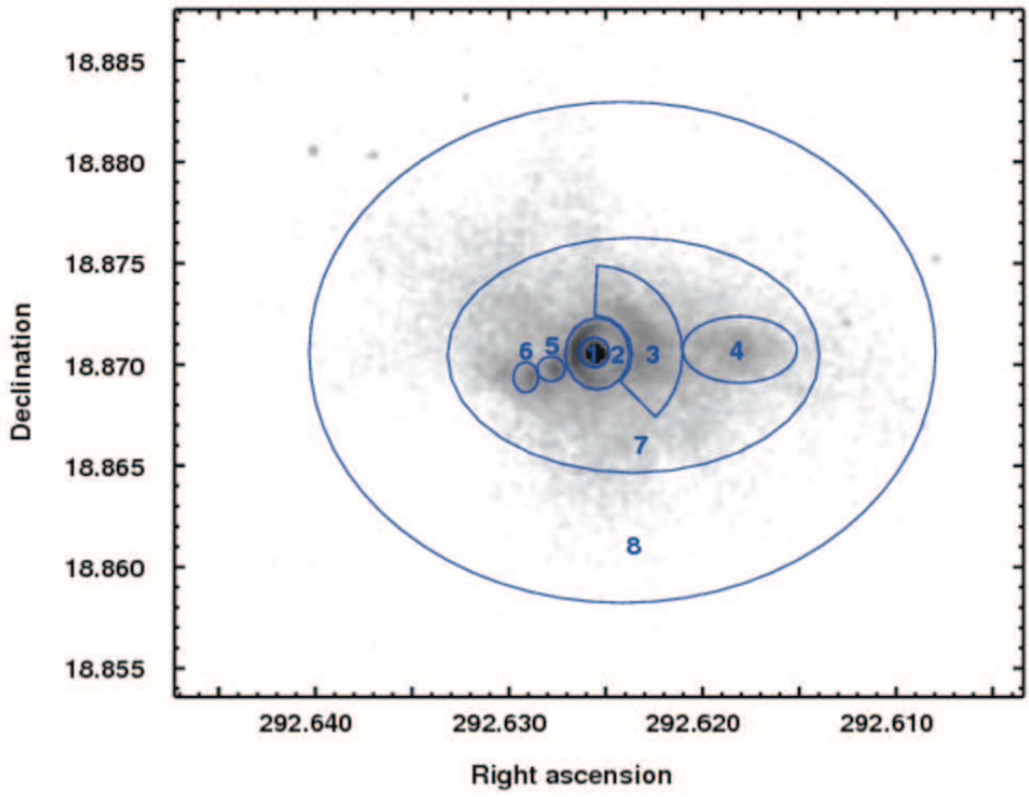

Figure 3.2 Extraction regions for the X-ray spectra, overlaid on the *Chandra* ACIS image of G54.1+0.3 in the 0.3–10.0 keV band. The fitted parameters for each of the numbered regions are summarized in Table 3.1.

Table 3.1. G54.1+0.3: Chandra ACIS Spectral Fitting Results

Region	Area(arcsec^2)	Photon Index	$N_H(10^{22}cm^{-2})$	F_X(total observed)	F_X(unabsorbed)	Reduced χ^2
1	22.03	1.44 ± 0.04	(1.95)	2.10E-12	3.26E-12	1.03
2	90.77	1.86 ± 0.05	1.95 ± 0.04	5.88E-13	1.21E-12	0.66
3	230.9	1.89 ± 0.05	...	6.64E-13	1.40E-12	0.92
4	185.4	1.79 ± 0.06	...	4.06E-13	7.88E-13	1.08
5	16.94	1.90 ± 0.12	...	8.94E-14	1.90E-13	0.63
6	19.12	1.97 ± 0.13	...	7.62E-14	1.73E-13	0.70
7	1586	2.05 ± 0.04	...	1.84E-12	4.45E-12	0.94
8	5559	2.20 ± 0.04	...	1.18E-12	3.34E-12	0.83

Note. — The extraction regions are shown in Figure 3.2. Listed uncertainties are 1.6 σ (90 % confidence) statistical uncertainties from the fit. The fluxes were calculated in the 0.3-10 keV band and are in the units of erg cm^{-2} s^{-1}.

and 6 s each for the short-low (SL) and LL modules, respectively. The high resolution spectra were taken at two different positions; the diffuse shell emission at 19h30m28.0s, $+18°52'15.60''$(J2000), and the bright knot at 19h30m26.40s, $+18°52'07.00''$(J2000). The location of the slits for the background spectrum are also shown in Fig 3.3. The short-high (SH) spectra were obtained using 10 cycles of 120 s, and the long-high (LH) using 5 cycles of 6 s each.

Data were processed with pipeline version S17.0.4 and cleaned using IRS Rogue Pixel Mask Editing and Image Cleaning software (IRSCLEAN1.9). The background was subtracted from the high resolution data, individual BCDs of each nod were median-combined, and spectra were extracted with the the *Spitzer* IRS Custom Extractor (SPICE) using full slit extractions with the extended source calibration for both low and high resolution modules. The subsequent analysis, including averaging of the individual nods, background subtraction for the low resolution modules, trimming of the order edges, and fitting of the emission lines, was carried out using the SMART (Higdon et al. 2004). For the low resolution modules, the spectra extracted from the off-source nods were used for the background. We have also included the imaging data from the IRAC and MIPS aboard *Spitzer*. The IRAC observations at 3.6, 4.5, 5.8, and 8.0 μm were carried out on 2005, Oct. 21, under the program ID 3647, using two 30 s frames. The data were processed with the pipeline version S14.0.0 and reduced with the MOPEX version 18.1.5. The MIPS 24 μm observation was carried out on 2005, May 15, under the program ID 3647, using 20 cycles of 30 s, and was processed with the pipeline version S16.1.0 (Slane 2008). The MIPS 70 μm image of G54.1+0.3 is from the MIPSGAL survey (Carey et al. 2009).

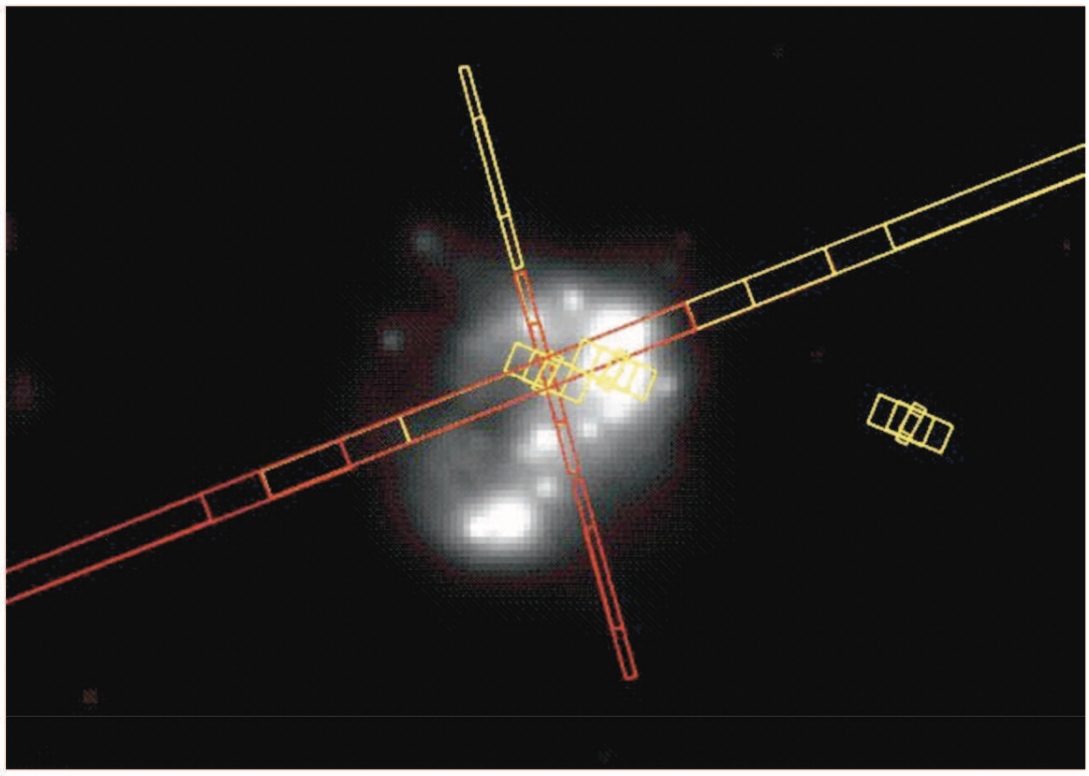

Figure 3.3 Positions of the IRS slits overlaid on the MIPS 24 μm image. The LL slits are the wide slits oriented in the East/West direction. The SL slits are oriented North/South. The LH and SH slits are the smaller slits shown in yellow. The eastern position is referred to as *position 1* in the text, and the western position on the IR knot is *position 2*. The LH and SH slits located off of the shell to the west were used for background subtraction.

3.3 Analysis

3.3.1 X-ray

The deep *Chandra* ACIS image of G54.1+0.3 in the 0.3-10 keV band is shown in Figure 3.1. The central pulsar is surrounded by a 5.″7 by 3.″7 X-ray ring, with the long axis oriented roughly north-south, suggesting an inclination angle of about 40 degrees (Lu et al. 2002). The pulsar and the ring are embedded in a diffuse nebula, 2.′0 by 1.′3 in size, which appears to have a bipolar elongation, running roughly east-west, perpendicular to the apparent plane of the ring. While the outer regions of the diffuse emission in G54.1+0.3 show a softer spectrum than the interior regions, there is no X-ray evidence for a thermal component associated with shock-heated ejecta or ISM.

Spectra were extracted from the *Chandra* data using the apertures shown in Figure 3.2. The regions are similar to those in Lu et al. (2002) and include the pulsar in region 1, the surrounding ring in region 2, the western arc in region 3, the western jet in region 4, two bright knots of emission in the east in regions 5 and 6, and fainter extended emission between these structures and in the outer regions of the PWN in regions 7 and 8, respectively. The background spectrum was extracted from an elliptical region south of the PWN with an area of 7710 square arcseconds. The spectrum for each of the regions was fitted with an absorbed power law model using the *Ciao* 3.4 *Sherpa* software. The fitting of region 1 also included a pileup model, since the point source count rate of 0.077 s^{-1} is expected to cause significant pileup that affects the spectral parameters (Davis 2001). The absorbing column density was fit simultaneously for regions 2–8, and the column density for the region encompassing the point source was then fixed to this value. The fitting results are summarized in Table 3.1. We find an absorption column density of $(1.95 \pm 0.04) \times 10^{22}$ cm^{-2}, somewhat greater than that of Lu et al. (2002), who found $N_H = (1.6 \pm 0.1) \times 10^{22}$ cm^{-2}. We find a similar value to that of Lu et al. (2002) if we include region 1 in the joint fit and do not account

for pileup. When the spectrum of each region is fit separately, the $N_H(10^{22}\ \mathrm{cm}^{-2})$ in regions 2–8 ranges from 1.88–2.19, while the best fit for region 1 gives an $N_H(10^{22}\ \mathrm{cm}^{-2})$ of 1.54. This suggests that a more accurate estimate for N_H is achieved if the piled-up region 1 is excluded from the fit.

The new estimate of the absorbing column density results in a slightly higher photon index for the pulsar, $\Gamma = 1.44 \pm 0.04$. The ring and E/W elongations have similar photon indices, which are harder (smaller) than those in the outer diffuse nebula, suggesting lower synchrotron losses or more particle injection in these regions. There is no evidence for emission lines in any of the spectra. The parameters derived from the initial analysis of the *Chandra* data are used in our analysis of the IR observations. A more detailed study of the X-ray data will be presented in a separate publication.

3.3.2 IR Morphology

The *Spitzer* IRAC and MIPS images of G54.1+0.3 reveal an IR shell south and west of the PWN, with the X-ray nebula filling the cavity of the shell. The shell is detected at 5.8, 8.0, 24, and 70 μm, and is approximately $1\farcm5$ in radius at 70 μm. A shell structure is evident in the 5.8 μm and 8.0 μm IRAC images, shown in Figures 3.4a and 3.4b, along with significant emission that extends far from the PWN to the north that may be associated with Polycyclic Aromatic Hydrocarbon (PAH) emission unrelated to G54.1+0.3. The structure of the shell in the MIPS images appears bipolar (Figure 3.4c and 3.4d), with a brighter western lobe, and a fainter southeastern lobe. The X-ray and radio emission from the PWN fills the cavity of the shell. The western jet structure, in particular, appears to extend directly into a void region in the IR nebula, terminating at the brightest region in the 24 μm MIPS image, i.e. the IR knot. This is best shown in Figure 3.5, where the MIPS 24 μm emission is shown in blue, MIPS 70 μm emission in green, radio emission in red, and *Chandra* X-ray contours in white. The most interesting features of the 24 μm image are 11 point sources embedded in

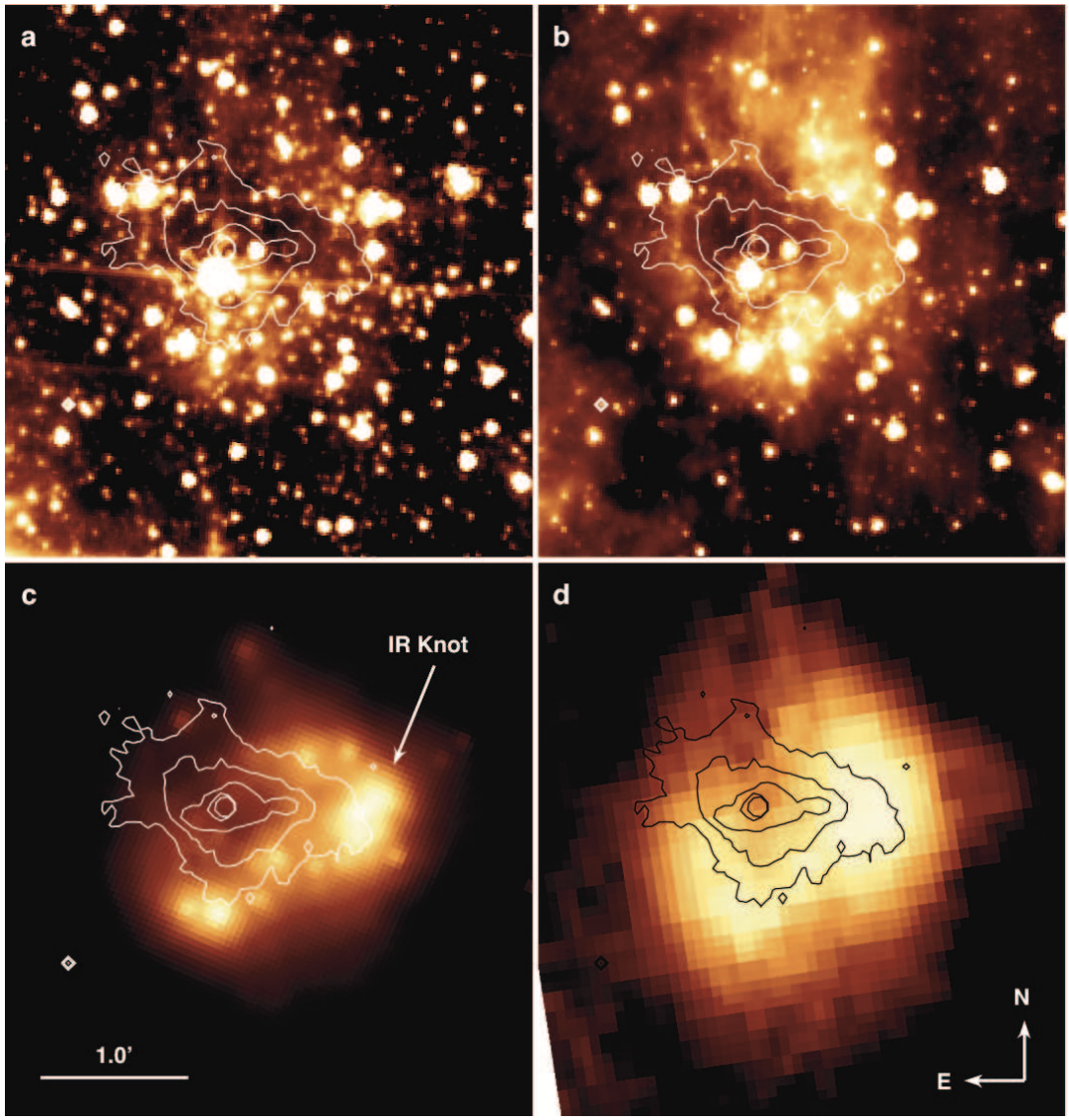

Figure 3.4 *Spitzer* imaging of the shell surrounding the PWN in G54.1+0.3. The shell is detected in the IRAC 5.8 μm (panel a) and 8.0 μm (panel b) bands. The MIPS 24 μm and 70 μm images are shown in panels c and d, respectively. The IR knot is indicated by the white arrow. The overlaid contours represent the Chandra ACIS contour of the PWN.

Table 3.2. G54.1+0.3: IRAC and MIPS Fluxes

Wavelength (μm)	Flux (Jy)	Extinction Corrected Flux (Jy)
5.8	~ 0.2	~ 0.3
8.0	~ 0.6	~ 1.0
24	23.7 ± 2.4	40 ± 4
IR knot	3.8 ± 0.4	6.5 ± 0.7
70	76 ± 15	$\cdots$

Note. — IRAC fluxes were estimated based on the average flux density at selected positions scaled to the size of the shell. The uncertainties include IRAC and MIPS calibration uncertainties, but do not account for the uncertainties in the extinction correction. The extinction correction was applied using the extinction curve of Chiar & Tielens (2006).

the diffuse shell that are arranged in a ring-like structure (Koo et al. 2008). The two northern point sources are outside of the ring structure, but appear to be located at the tips of faint ridges of emission that trace back to the shell structure. The IRAC and MIPS fluxes from the IR shell and the knot are listed in Table 3.2. Since the shell region in the IRAC images is crowded with stars, the fluxes were estimated by scaling the average flux density from several positions on the shell by the total area of 4 square arcminutes. In measuring the flux from the IR knot, we used a background region from the diffuse shell emission east of the knot.

3.3.3 IR Spectroscopy

The high and low resolution IR spectra of G54.1+0.3 are shown in Figures 3.6 and 3.7, and the positions of the IRS slits are shown in Figure 3.3. The low resolution spectrum shows a rising continuum longward of 15 μm, and a broad emission feature peaking at approximately 21 μm. This feature is more pronounced in the high resolution spectrum

of the bright knot, while it is less pronounced in the spectrum from the diffuse shell (Figure 3.6). The high resolution spectra also reveal a broad emission feature around 12 μm, and a narrow emission feature around 11.3 μm that may be associated with PAH emission or other carbonaceous grains. The high resolution slit from which the background spectrum was extracted is located in a region of low background emission, and it underestimates the contribution from the emission in the vicinity of the IR shell that is evident in the IRAC 8 μm image (Figure 3.4b). However, the background regions for the low resolution spectrum are more representative of the local background emission. Since the low resolution spectra were extracted from the entire SL and LL slits, they are not characteristic of the point-to-point spectrum along the slits that varies spatially. The sharp peak around 7.5 μm is an artifact caused by a mismatch between orders, and was trimmed from the residual source spectrum.

There are a total of ten emission lines present in the spectrum of the IR shell; the molecular hydrogen H_2 S(2) (12.3 μm), and H_2 S(1) (17.0 μm) lines, and ionic lines of [ArII] (6.99 μm), [SIV] (10.51 μm), [NeII] (12.81 μm), [ClII] (14.37 μm), [SIII] (18.71 μm), [FeII] (25.99 μm), [SIII] (33.48 μm), and [SiII] (34.82 μm). The line-fitting parameters for the LH and SH modules are listed in Table 3.3, where positions 1 and 2 correspond to spectra from the diffuse shell and the bright IR knot, respectively (see Figure 3.3). Line-fitting parameters from the overlapping region of SL and LL modules are listed in Table 3.4. The extinction correction was applied using the IR extinction curve of Chiar & Tielens (2006), and the relation $N_H/A_K = 1.821 \times 10^{22}$ cm^{-2} (Draine 1989). As shown in Figure 3.7, background emission significantly contributes to the observed lines of Ne, S and Si, implying that the uncertainties on their measured line intensities are probably larger than the statistical uncertainties quoted in Table 3.3. A number of emission lines in the high resolution spectrum show evidence of broadening with respect to the spectral resolution of IRS of $\lambda/\Delta\lambda \sim 600$, including Cl, S, Fe, and Si. The broadened line profiles of the Si and S lines are shown in Figure 3.8.

For the purpose of examining the spatial variation in the emission line intensities across the LL slits, we created 2-dimensional spectral line maps using the CUbe Builder for IRS Spectral Maps (CUBISM) software (Smith et al. 2007). The maps were made by selecting a desired wavelength region for the source flux and subtracting a wavelength-weighted background, averaged across a specified wavelength region. The maps were created by selecting a source flux from 20.9–21.9 μm, with a continuum from 20.5–20.7 μm and 22.3–22.6 μm to show the spatial variation of the 21 μm feature; a source flux between 18.4–18.9 μm with a continuum between 18.0–18.4 μm and 18.9–19.0 μm for the [SIII] line at 18.7 μm; a source flux between 33.1–33.9 μm, with a continuum between 31.9–32.9 μm and 33.9–34.2 μm for the [SIII] line at 33.5 μm; and a source flux from 34.6–35.2 μm, with a continuum from 34.1–34.4 μm for the [SiII] line at 34.8 μm. The narrow wavelength ranges for the backgrounds were chosen to avoid other emission features and large gradients in the continuum slope. We smoothed the spectral line maps by a 2-pixel Gaussian before plotting the intensity profiles as a function of position along the slit. Spectra were also extracted from 7 spatial positions along the LL slit in 3×2 pixel sub-slits. Due to the low extraction area, only the brightest lines of S and Si were measurable in these spectra. Their intensities are listed in Table 3.5, where the position along the LL slit is denoted by the pixel number on the axis in Figure 3.9.

3.4 Line Emission

Spectra of the diffuse shell were obtained with all four modules of the IRS (Figure 3.3). The high resolution SH and LH spectra were taken at two different positions on the shell; at the position of diffuse emission near the interface between the shell and the PWN (position 1), and at the position of the bright IR knot in the northwest (position 2). The LL slit was oriented in the East/West direction and it spans the entire length of the shell, including the IR knot. The SL slits were roughly perpendicular to the LL

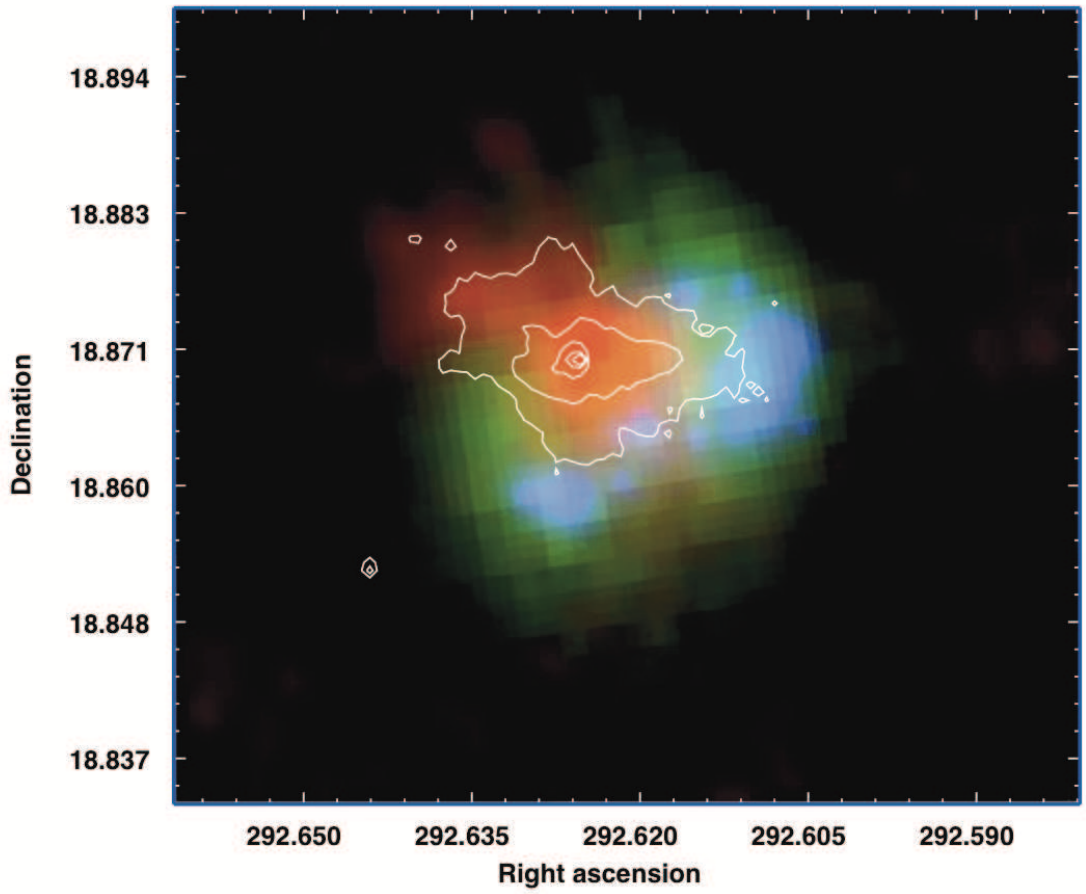

Figure 3.5 Three color image of G54.1+0.3, where the MIPS 24 μm emission is shown in blue, MIPS 70 μm emission in green, and radio emission in red. The *Chandra* X-ray contours are shown in white.

slits, and span the length of the shell in the North/South direction.

3.4.1 Line Profiles and Broadening

The high-resolution spectra at both positions in the IR shell show evidence of spectral line broadening. The fitted line parameters for the two positions are summarized in Table 3.3. The expected resolution of LH and SH is $\lambda/\Delta\lambda \sim 600$, equal to a full-width half-maximum (FWHM) of 500 $\mathrm{km\,s^{-1}}$. The [ClII], [FeII], and [SiII] at position 1 show the largest broadening of over a 1000 $\mathrm{km\,s^{-1}}$. The [SIII] lines at this position are broadened to approximately 700–800 $\mathrm{km\,s^{-1}}$. The [NeII] line at position 2 shows evidence for slight broadening, while the widths of the H_2 lines are approximately equal to the resolution of the IRS. It is likely that inadequate subtraction of the local background from the LH and SH spectra contributes significantly to spectral lines with narrow widths. The true FWHM in Table 3.3 was calculated by subtracting the instrumental FWHM of the IRS from the observed FWHM in quadrature (see Dasyra et al. 2008).

The lines in the spectrum at the position of the IR knot (position 2) are broadened by a lesser amount than at position 1. The [ClII] and [SiII] lines again show the greatest broadening of $\sim$ 800–900 $\mathrm{km\,s^{-1}}$, while the [SIII] lines are only slightly broadened to an average of $\sim$ 600 $\mathrm{km\,s^{-1}}$. We also note that the best-fit centroid of the [SIII] lines at both positions appears to be redshifted by an average of $\sim$ 120 $\mathrm{km\,s^{-1}}$. Although this shift is not very large considering that the uncertainty of the IRS wavelength calibration for the high-resolution modules is on the order of 100 $\mathrm{km\,s^{-1}}$, it is consistently larger than the shift of all the other observed lines. The exception is the [FeII] line with a redshift of 191 ± 97 $\mathrm{km\,s^{-1}}$, but this line is faint and the shift has a high uncertainty. The profiles of the lines with the highest broadening show evidence for structure. The high resolution line profiles of [SiII] 34.8 μm and [SIII] 33.5 μm at both positions are shown in Figure 3.8 for comparison. At position 1, the [SiII] line appears to have

a brighter component that peaks at approximately the same wavelength as [SIII], in addition to a fainter blue shifted wing.

3.4.2 Spatial Variation in Line Intensities

The variation in the surface brightness across the LL slit of the [SIII] 18.7 μm, [SIII] 33.5 μm, and the [SiII] 34.8 μm lines, and the SL spectral line map of the [ArII] 6.99 μm line are shown in Figure 3.9. The peak surface brightness for each line has been normalized to unity, so their relative fluxes are not represented by the plot. The intensities as a function of position for all lines in Figure 3.9 show structure that correlates with the MIPS 24 μm image of the shell. The intensity of the [SIII] 33.5 μm line is well correlated with the 24 μm emission and it appears to stay roughly constant across the western part of the IR shell, with a possible slight rise at the location of the bright IR knot. The spatial intensity profile of the [SIII] 18.7 μm line is similar to the profile of the 21 μm feature and shows a sharp peak at the position of the IR knot, implying an increase in density at this position (see Section 3.4.4).

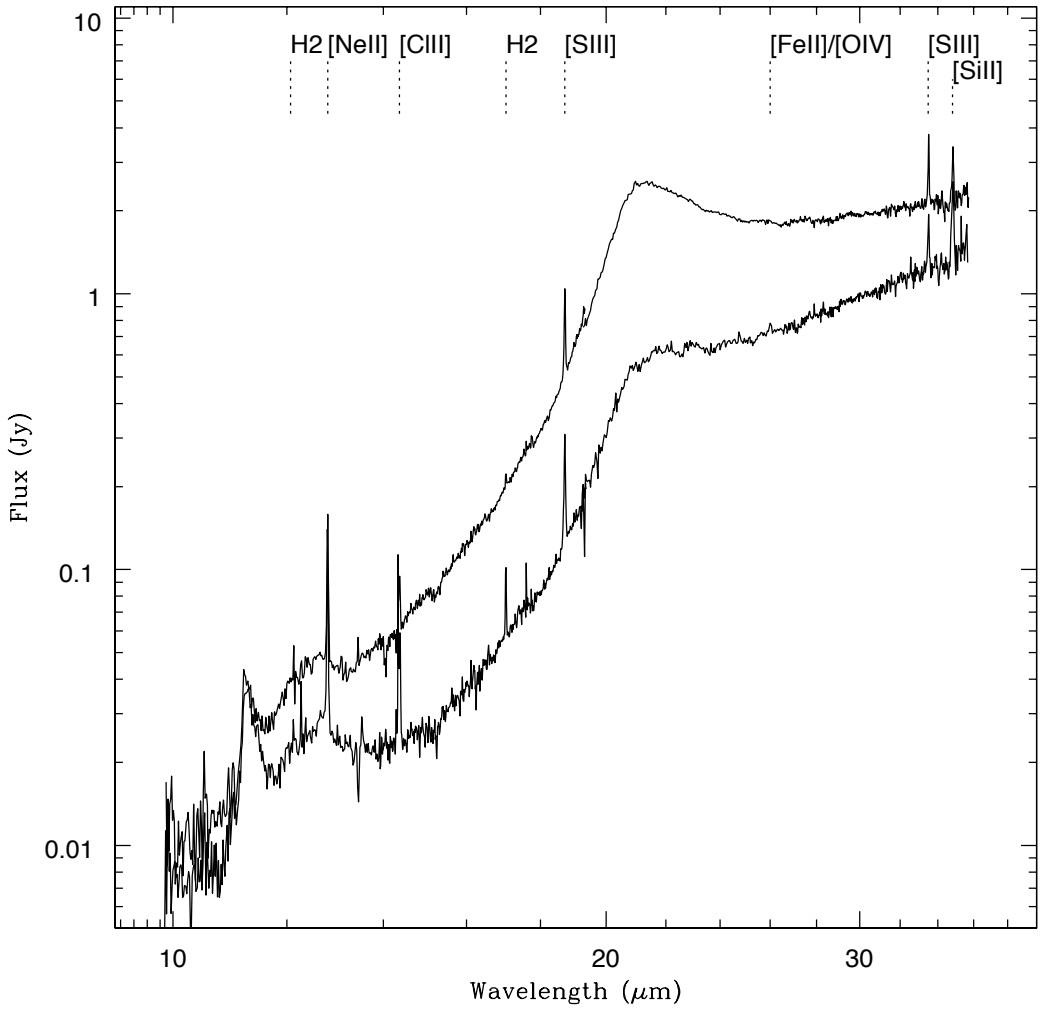

Figure 3.6 High resolution *Spitzer* IRS SH and LH spectra of the IR shell in G54.1+0.3. The fainter spectrum is from position 1, the interface between the PWN and the shell, and the brighter spectrum is from position 2 at the IR knot (see Figure 3.3).

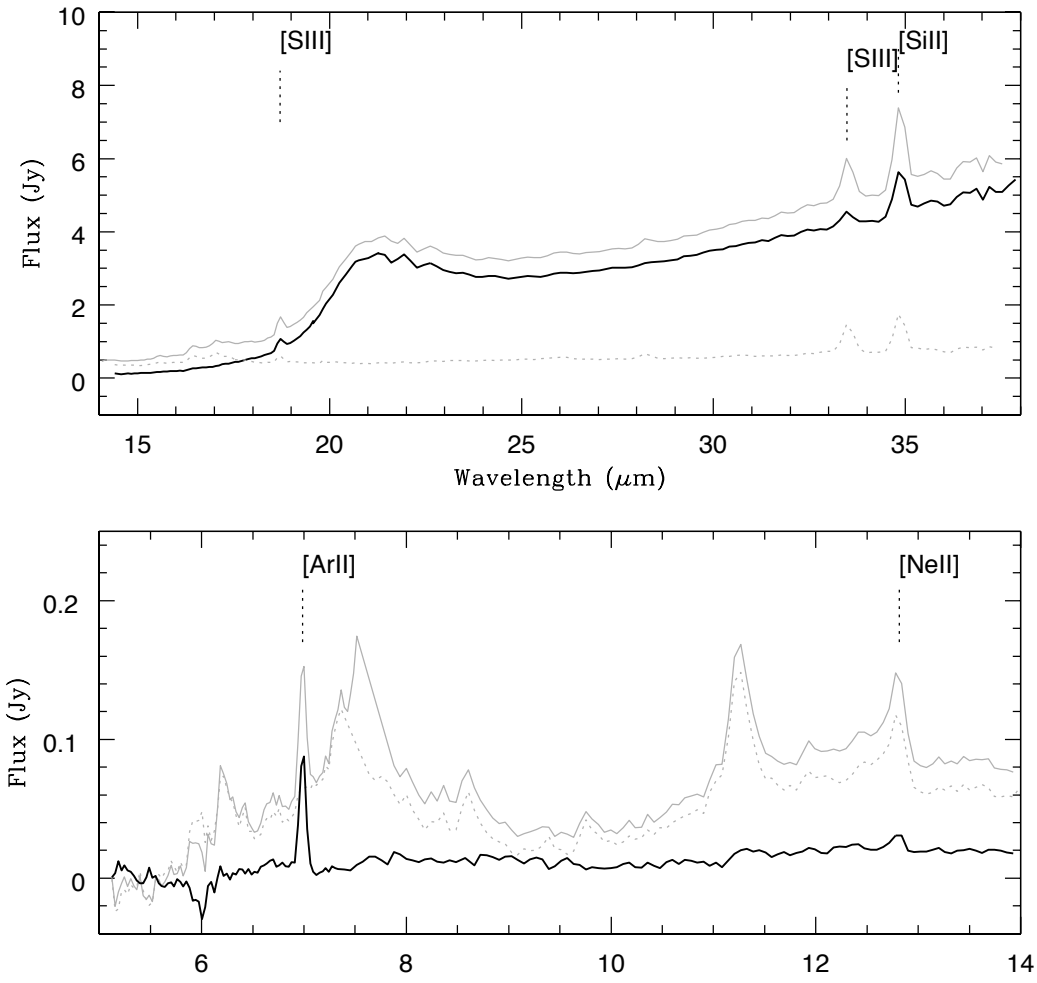

Figure 3.7 Low resolution *Spitzer* IRS spectra extracted from the entire LL slit (top panel) and SL slit (bottom panel). The solid grey spectra represent spectra before background subtraction, dashed grey spectra are from the background extracted from the off-source nod positions, and the black spectra are the background-subtracted source spectra. The peak at around 7.5 μm is due to an order mismatch at the edges, and was trimmed in the final spectrum.

Table 3.3. G54.1+0.3: IRS Line Fits

Line ID	Line Center (μm)	Line Flux	De-reddened	FWHM (μm)	FWHM (km/s)	True FWHM (km/s)	Shift (km/s)
Position 1							
H_2 (12.2786)	12.2775 ± 0.0013	1.24 ± 0.31	2.15 ± 0.54	0.018 ± 0.001	435 ± 24	...	-29 ± 35
[NeII] (12.8135)	12.8138 ± 0.0008	11.15 ± 0.76	18.72 ± 1.28	0.024 ± 0.001	568 ± 24	279 ± 104	5 ± 20
[ClII] (14.3678)	14.3721 ± 0.0005	4.59 ± 0.16	7.79 ± 0.27	0.049 ± 0.001	1029 ± 21	902 ± 32	89 ± 9
H_2 (17.0348)	17.0385 ± 0.0004	2.74 ± 0.10	5.10 ± 0.19	0.030 ± 0.001	525 ± 18	177 ± 165	65 ± 6
[SIII] (18.7130)	18.7195 ± 0.0010	13.51 ± 0.83	26.61 ± 1.64	0.051 ± 0.001	823 ± 16	658 ± 44	104 ± 16
[FeII] (25.9883)	26.0048 ± 0.0084	4.62 ± 1.26	7.33 ± 1.99	0.095 ± 0.008	1089 ± 92	966 ± 33	191 ± 97
[SIII] (33.4810)	33.4890 ± 0.0026	25.28 ± 2.67	35.94 ± 3.79	0.075 ± 0.003	675 ± 27	450 ± 70	72 ± 23
[SiII] (34.8152)	34.8174 ± 0.0040	72.69 ± 6.67	102.76 ± 9.43	0.136 ± 0.004	1172 ± 34	1059 ± 30	19 ± 35
Position 2							
[SIV] (10.5105)	10.5164 ± 0.0019	1.07 ± 0.19	2.47 ± 0.43	0.021 ± 0.001	596 ± 28	334 ± 87	168 ± 55
[NeII] (12.8135)	12.8123 ± 0.0003	9.74 ± 0.30	16.36 ± 0.50	0.029 ± 0.001	675 ± 23	450 ± 70	-28 ± 6
[ClII] (14.3678)	14.3689 ± 0.0011	3.12 ± 0.28	5.28 ± 0.48	0.037 ± 0.001	780 ± 21	604 ± 48	23 ± 21

Table 3.3 (cont'd)

Line ID	Line Center (μm)	Line Flux	De-reddened	FWHM (μm)	FWHM (km/s)	True FWHM (km/s)	Shift (km/s)
H_2 (17.0348)	17.0392 ± 0.0016	1.18 ± 0.22	2.20 ± 0.40	0.028 ± 0.002	490 ± 35	...	77 ± 29
[SIII] (18.7130)	18.7212 ± 0.0006	33.92 ± 1.49	66.81 ± 2.94	0.041 ± 0.001	651 ± 16	424 ± 69	132 ± 9
[SIII] (33.4810)	33.4939 ± 0.0011	48.08 ± 2.68	68.36 ± 3.80	0.059 ± 0.001	528 ± 9	160 ± 198	116 ± 10
[SiII] (34.8152)	34.8229 ± 0.0046	57.30 ± 7.56	81.00 ± 10.68	0.108 ± 0.005	934 ± 43	786 ± 40	66 ± 40

Note. — Listed uncertainties are 1-σ statistical uncertainties from the fit and do not include the IRS wavelength and flux calibration uncertainties. Fluxes are in the units of $10^{-6} erg/cm^2/s/sr$.

Curiously, the intensity of the [SiII] line has a large peak at the apparent interface between the PWN and the IR shell. This peak is a factor of two brighter than the [SiII] emission across the rest of the shell and does not correlate with spatial features shown by the IR continuum emission nor the [SIII] lines. The relative intensities of the [SIII] and [SiII] across the LL slit are also summarized in Table 3.5, where the line fluxes were measured at 7 positions from spectra extracted from 3×2 pixel sub-slits. The highest line broadening is seen at roughly the same position where the [SiII] line peaks, position 1 of the high-resolution spectrum. As shown in Figure 3.9, the intensity of [ArII] as a function of position along the SL slit also peaks near the same position. Figure 3.10 shows the spatial profiles of the 24 μm shell emission and the [ArII] and [NeII] lines across the SL slit. The intensities of 24 μm emission and [ArII] appear to be anti-correlated spatially. The [ArII] and [NeII] lines also appear to be anti-correlated across the SL slit. The Ne line is brightest along the northern part of the IR shell, positions 0–13 in Figure 3.10. Figure 3.11 shows sample spectra from three different positions across the SL slit, extracted from 2 by 6 pixel sub-slits. The three positions show spectra with weak [NeII] emission, strong [NeII] emission, and emission with prominent broad features at 9 and 12 μm. The spectrum with the strong broad features was extracted from the position of an embedded point source, suggesting that these features may be associated with the source, or enhanced in its vicinity.

3.4.3 Evidence of Multiple Components

The spectral line properties discussed above seem to suggest that the observed emission lines arise from multiple, physically distinct components. Neufeld et al. (2007) analyzed IRS spectral line maps from several SNRs interacting with molecular clouds and found that the line emission generally originates from five spatially distinct groups; 1) lines of neutral sulfur and H_2 (J>2); 2) lines of H_2 S(0), 3) lines of ions with low ionization potentials such as [FeII], [SiII], and [PII] , 4) lines of ions with ionization potentials

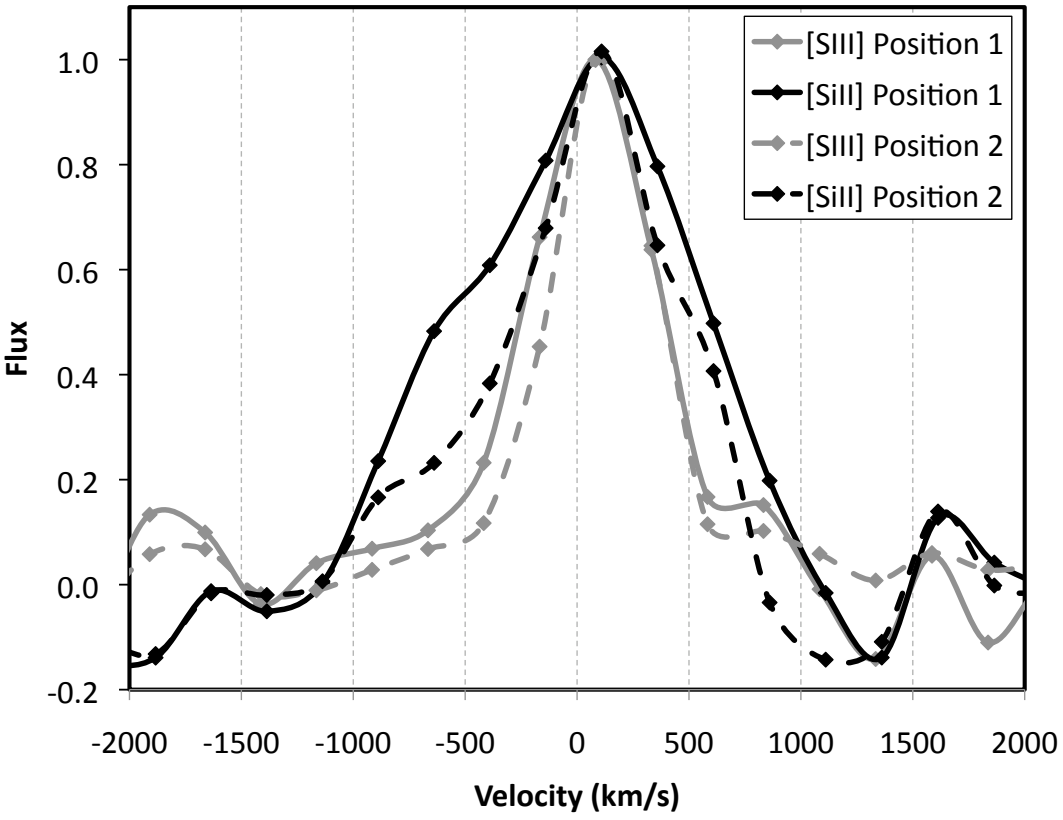

Figure 3.8 High resolution spectral profiles of the [SiII] and [SIII] 33.5 μm lines at two positions in the IR shell. The 1-σ statistical uncertainties on each data point are on the order of 20%.

higher than 13.6 eV, not including [SIII], and 5) line of [SIII]. While the lines in various groups sometimes showed similar spatial distributions, the lines within a group were always strongly correlated (Neufeld et al. 2007).

In the case of G54.1+0.3, the [ClII], [FeII], and [SiII] lines are all broadened by a similar amount at both positions of the high-resolution slits, and all three have low ionization potentials of less than 13.6 eV. The FWHM deconvolved by the instrumental resolution (true FWHM in Table 3.3) is on the order of 1000 km/s. The [SIII] lines show less broadening, have centroids that are slightly redshifted relative to the other observed emission lines, and have a higher ionization potential of 23.34 eV. The intensities of the lines in the proposed components do not appear to correlate spatially. While the Si emission strongly peaks at the position where the PWN appears to encounter the IR shell, the spatial plot of the S and Ne intensities shows no enhancement at this position. We are not able to determine if the S and Ne lines are spatially correlated, since the SL and LL slits sample different regions of the shell. The spatial distribution of the Ar line is anti-correlated with Ne, and it appears to peak at approximately the same region where Si is enhanced. It appears that the spectral line emission from the IR shell arises from distinct components; a component producing the highly broadened lines of ions with low ionization potentials, including Si, Cl, Fe and perhaps Ar, a component from which most of the sulfur emission originates, and a component giving rise to the [NeII] line that may or may not be spatially correlated with S lines.

3.4.4 Electron Density

The electron density of the emitting material can be probed using the temperature-insensitive density diagnostic ratio of the ground state fine structure lines of [SIII] at 18.7 μm and 33.5 μm . Both lines are present in the LL module, and the ratio of their surface brightness maps is shown by the dashed curve in Figure 3.9. Since the spectral maps were used to calculate the [SIII] line ratios across the slit, the absolute values of

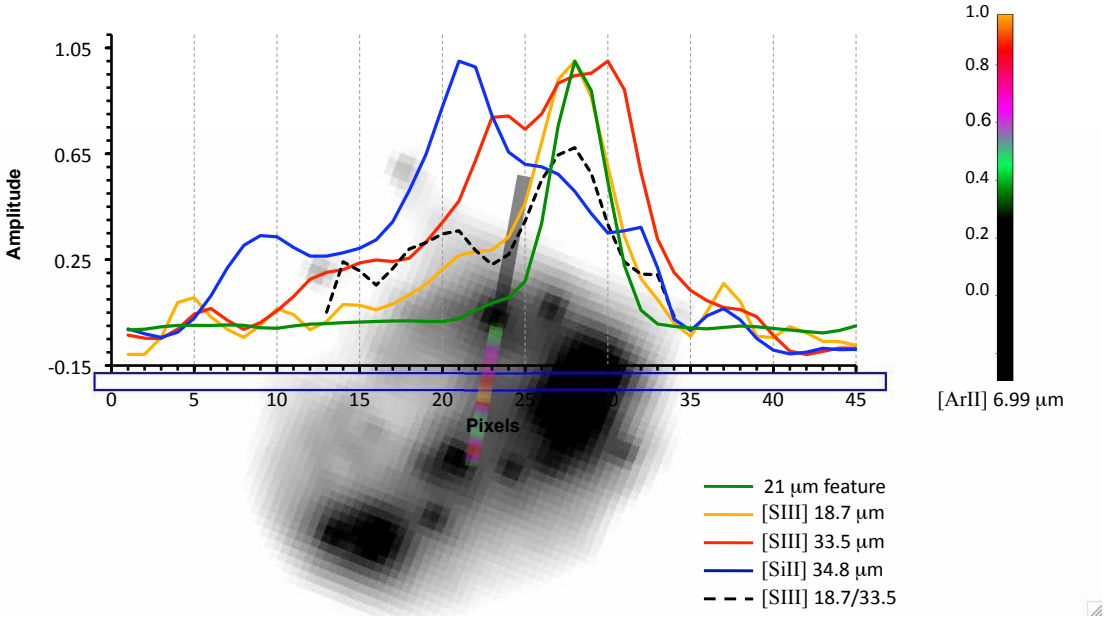

Figure 3.9 Intensity of various emission features in the G54.1+0.3 spectrum as a function of the position across the low-resolution IRS slits. The position of the LL slit, represented by the blue box, is overlaid on the MIPS 24 μm image of G54.1+0.3. The pixel scale is 5.1″/pixel. The curves in the plot show the spatial intensity variation of the 21 μm feature (green), and the [SiII] (blue), [SIII] (red & orange) lines. The peak intensity of each feature has been normalized to unity and the amplitudes do not represent actual flux values. The black dotted line shows the actual ratio of the fluxes of the [SIII] 18.7 μm and 33.5 μm lines. The overlaid slit running N/S represents a normalized surface brightness map of the [ArII] line at 6.99 μm. The statistical 1-σ uncertainties of the intensities at each pixel are approximately 0.05 for the 21 μm feature, 0.09 for [SiII], 0.09 for [ArII], and 0.12 for [SIII] lines.

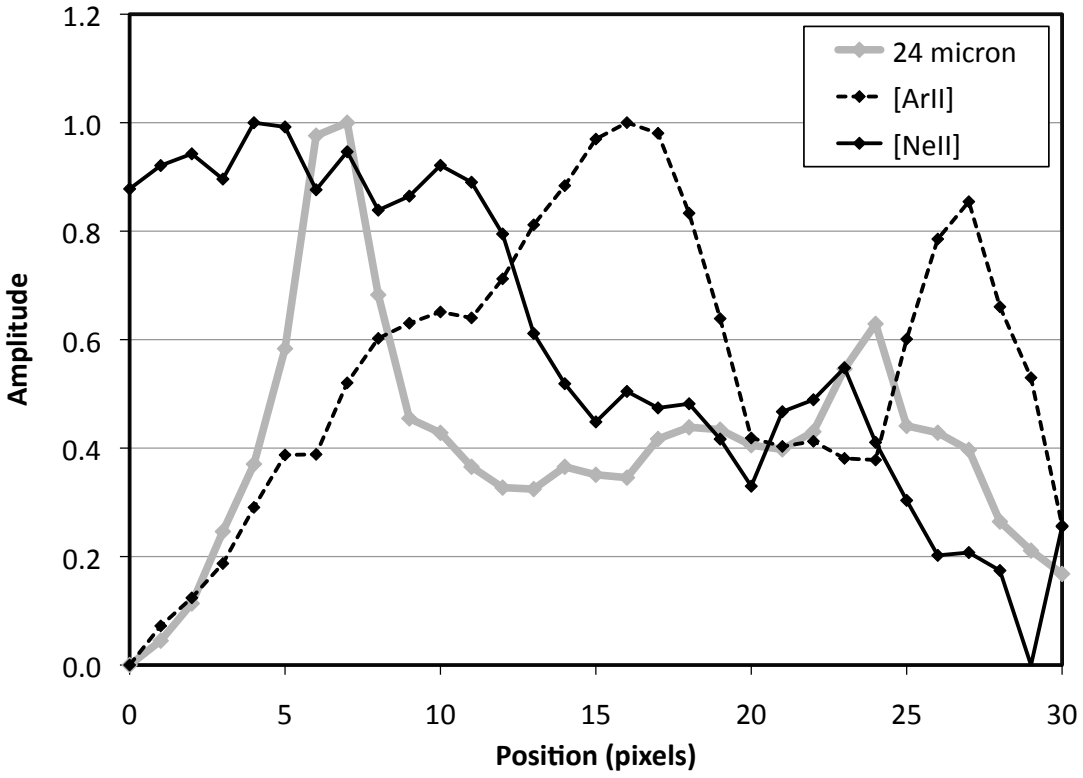

Figure 3.10 Intensity of the [ArII], [NeII], and 24 μm shell emission as a function of position across the SL slit. The slit is shown in Fig. 3.9. Positions 0–30 correspond to positions across the SL slit from northern to southern edge of the IR shell emission. The statistical 1-σ uncertainties on each data point are on the order of 15%. The pixel scale for the SL slit is 1.8″/pixel.

Table 3.4. G54.1+0.3: IRS Line Fits in LL & SL Overlap Region

Line ID	Line Center (μm)	Line Flux	De-reddened
Region 1			
[ArII] (6.9853)	6.993 ± 0.001	84.9 ± 4.9	122.4 ± 7.1
[NeII] (12.8135)	12.813 ± 0.013	6.4 ± 1.9	10.8 ± 3.3
[ClII] (14.3678)	14.401 ± 0.013	3.2 ± 1.3	5.4 ± 2.2
[SIII] (18.7130)	18.733 ± 0.004	11.9 ± 1.1	23.5 ± 2.2
[SIII] (33.4810)	33.539 ± 0.029	33.7 ± 8.4	47.9 ± 11.9
[SiII] (34.8152)	34.889 ± 0.015	79.3 ± 10.6	112.1 ± 14.9

Note. — Fluxes are in units of 10^{-6}erg/cm^2/s/sr. Listed uncertainties are 1-σ statistical uncertainties from the fit and do not include the IRS wavelength and flux calibration uncertainties.

the point-to-point ratios in Figure 3.9 are highly uncertain. Since the line profiles were not fitted in this case, the shape of the underlying continuum and the variation of the [SIII] line strength in the local background all contribute to the uncertainty. However, it is clear that the ratio peaks at the location of the bright IR knot, implying that the electron density here sharply increases. We estimated the electron densities using the extinction corrected intensities of the fitted [SIII] lines in the LH and SH spectra (Table 3.3) and at multiple positions across the LL slit (Table 3.5). The calculation was performed using the IRAF STSDAS *Nebular* package (Shaw & Dufour 1995). The high resolution [SIII] 18.7 μm/33.5 μm line ratios are 0.7 ± 0.1 and 1.0 ± 0.1 for positions 1 and 2, respectively, giving densities of 650 ± 240 cm^{-3}, and 1070 ± 200 cm^{-3} for an assumed temperature of 1000 K. The quoted uncertainties are statistical uncertainties from the fit only. The ratios have additional uncertainties due to the fact that the LH and SH slits have different sizes and orientations, which affects the average surface brightness in the slit. Since the local background also contains [SIII] lines, spatial variations in the background add additional unquantifiable uncertainties

to the line ratios. Table 3.5 shows the [SIII] ratio at six different positions across the LL slit. The ratios for all regions are consistent with being at the low density limit, except for the region corresponding to the IR knot at which the density is obviously higher, in the 900–2400 cm^{-3} range.

3.4.5 Shock Diagnostics

The PWN in G54.1+0.3 appears to fill the cavity of the IR shell, with the pulsar jet terminating at the IR knot (Figure 3.5). Due to morphological correlation between the PWN and the IR shell, it is possible and even likely that the pulsar wind is sweeping through the shell material, and that the jet may be interacting with the dense region of the IR knot. In order to estimate the velocity of the shock propagating into the shell material, we compared the spectral line intensities in Table 3.3 to shock models. Models with cosmic abundances and models with the refractory elements depleted by a factor of 3 were run with the code used by Hartigan et al. (1987) for several shock speeds and pre-shock densities. Electron and ion temperatures were taken to be equal because of the modest shock speed (Ghavamian et al. 2001). Table 3.6 lists the results of shock models with cosmic abundances and abundances with depleted refractory elements for a range of shock velocities. Direct comparison with the observed line intensities is difficult because different lines seem to originate in different places. However, a few general comments can be made. A shock speed of about 100 $\mathrm{km\,s}^{-1}$ is needed to produce SIV, though a slightly lower speed would better match the upper limit to the NeIII/NeII ratio. A shock faster than 110 kms^{-1} would produce too much OIV emission. A pre-shock density of about 10 cm^{-3} gives a reasonable match to the density-sensitive SIII line ratio. The [ArII] intensities are far too large to match any model with normal abundances, so that line must originate in the ejecta. A factor of three depletion of Si and Fe (and presumably other refractory elements) is needed to account for the weakness of the [SiII] and [FeII] lines at position 1, while a larger factor is required at

position 2. The depletion could be more severe if those lines originate from a different emission component. The observed depletion would reflect partial destruction of grains from the more highly depleted pre-shock gas (e.g. Jones et al. 1996).

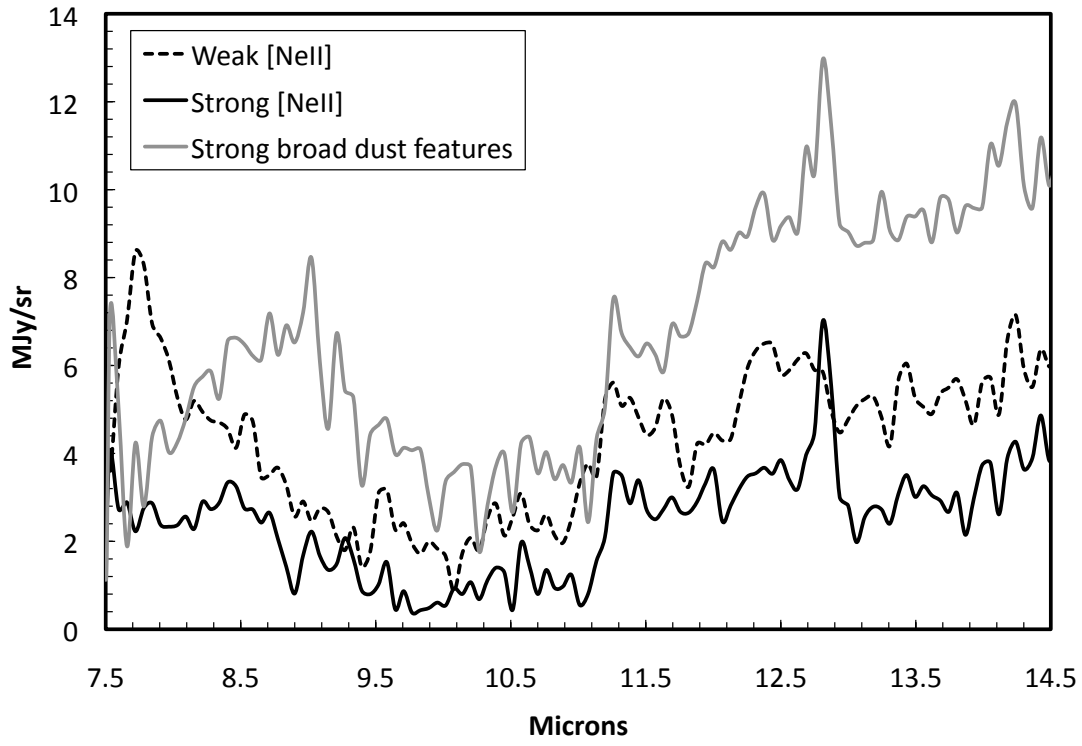

Figure 3.11 Sample spectra from three different positions along the SL slit. The spectra were extracted from 6 pixel long sub-slits at positions showing strong and weak [NeII] emission, and at the position coincident with an embedded point source, where the 9 and 12 μm broad emission features are most prominent. The pixel scale for the SL slit is 1.8″/pixel.

Table 3.5. G54.1+0.3: IRS Line Fits Across the LL Slit

Line ID	Line Center (μm)	Line Flux 10^{-6} erg cm^2 s^{-1} sr^{-1}	De-reddened Flux 10^{-6} erg cm^2 s^{-1} sr^{-1}	SIII Ratio (18.7/33.5μm)	Density (cm^{-3})
Region 1 (Pixel 14)					
[SiII] (34.8152)	35.01 ± 0.02	35.4 ± 4.5	49.9 ± 6.4		
Region 2 (Pixel 17)					
[SIII] (18.7130)	18.76 ± 0.01	4.7 ± 0.8	9.3 ± 1.5		
[SIII] (33.4810)	33.61 ± 0.02	9.5 ± 1.6	13.5 ± 2.3	0.69 ± 0.16	< 800
[SiII] (34.8152)	34.95 ± 0.02	47.6 ± 7.2	67.7 ± 10.1		
Region 3 (Pixel 20)					
[SIII] (18.7130)	18.73 ± 0.01	9.1 ± 2.1	18.0 ± 4.3		
[SIII] (33.4810)	33.57 ± 0.02	15.4 ± 3.8	21.8 ± 5.4	0.83 ± 0.28	< 1300
[SiII] (34.8152)	34.90 ± 0.01	106.3 ± 8.4	149.9 ± 11.9		
Region 4 (Pixel 23)					
[SIII] (18.7130)	18.73 ± 0.01	12.1 ± 1.0	23.8 ± 2.0		
[SIII] (33.4810)	33.52 ± 0.02	28.9 ± 6.7	41.0 ± 9.5	0.58 ± 0.14	< 600

Table 3.5 (cont'd)

Line ID	Line Center (μm)	Line Flux 10^{-6} erg cm^2 s^{-1} sr^{-1}	De-reddened Flux 10^{-6} erg cm^2 s^{-1} sr^{-1}	SIII Ratio (18.7/33.5μm)	Density (cm^{-3})
[SiII] (34.8152)	34.89 ± 0.01	78.2 ± 10.7	110.3 ± 15.1		
Region 5 (Pixel 26)					
[SIII] (18.7130)	18.73 ± 0.01	26.5 ± 2.0	52.1 ± 4.0		
[SIII] (33.4810)	33.44 ± 0.02	29.6 ± 8.1	42.0 ± 11.5	1.24 ± 0.35	900 – 2400
[SiII] (34.8152)	34.89 ± 0.02	64.6 ± 8.6	91.7 ± 12.3		
Region 6 (Pixel 29)					
[SIII] (18.7130)	18.72 ± 0.01	23.9 ± 3.1	47.0 ± 6.0		
[SIII] (33.4810)	33.55 ± 0.01	54.9 ± 7.7	77.9 ± 10.9	0.60 ± 0.11	< 600
[SiII] (34.8152)	34.84 ± 0.01	50.5 ± 7.4	71.6 ± 10.6		
Region 7 (Pixel 32)					
[SIII] (18.7130)	18.71 ± 0.01	11.1 ± 3.7	21.8 ± 7.3		
[SIII] (33.4810)	33.53 ± 0.02	21.1 ± 4.2	30.0 ± 6.0	0.73 ± 0.28	< 1100
[SiII] (34.8152)	34.90 ± 0.03	48.5 ± 7.8	68.8 ± 11.1		

Table 3.6. G54.1+0.3: Shock Model Line Intensities

Shock Speed (km/s)	HI/H	Hβ	S IV	Ar II	Ne II	Ne III	S III	O IV	Fe II	S III	Si II
Cosmic Abundances											
(H:He:C:N:O:Ne:Mg:Si:S:Ar:Ca:Fe =12:10.93:8.52:7.90:8.72:7.90:7.42:7.52:7.20:6.90:6.30:7.50)											
100	0.31	3.96e-06	0.84	9.16	38.9	25.1	12.1	1.32	58.4	21.3	427
Depleted Abundances											
(H:He:C:N:O:Ne:Mg:Si:S:Ar:Ca:Fe =12:10.93:8.02:7.90:8.72:7.90:7.02:7.02:7.20:6.90:5.60:7.0)											
80	0.92	2.87e-06	···	3.95	12.0	0.47	4.45	···	5.82	7.86	42.7
90	0.62	3.59e-06	···	6.33	16.2	3.25	3.42	···	5.22	5.85	39.9
100	0.31	2.78e-06	1.51	7.81	21.3	33.0	11.9	2.10	6.83	20.2	50.9
110	0.00	1.96e-06	3.24	11.9	33.0	66.1	30.3	11.3	10.4	50.8	77.9

Note. — Shock models were run with the code from Hartigan et al. (1987). The preshock density of the models, $n_0 = 10\,\mathrm{cm}^{-3}$ and $B_0 = 30$ μG. Hβ is in the units of erg/s/cm^2/sr, and the intensities of the other lines are relative to Hβ=100. The depleted shock models include a factor of $\sim$3 depletion of refractory elements.

3.5 Dust Emission

IR imaging and spectroscopy of G54.1+0.3 can provide important information about the properties and distribution of dust in the IR shell. The study of ISM dust provides constraints on models describing dust composition and properties. These models are best described by a grain composition that predominantly consist of astronomical silicates and carbonaceous material, such as PAHs, graphite, and amorphous carbon (for a review see Draine 2009). While a large fraction of interstellar dust is grown in the ISM (Draine 2009), the rest is injected by stellar winds, PNe, novae, and SNe. Dust is formed in the cooling gas, where the density is high enough for grain growth, and the dust composition depends on the available gas abundances and environmental conditions in these objects. Models show that SN ejecta can have a range of compositions, with some of the most abundant grains being those of $MgSiO_3$, SiO_2, Mg_2SiO_4, Si, and C (for a review see Kozasa et al. 2009). The shape of the IR spectrum and the presence of various emission features are clues that can help determine the mass and composition of dust in G54.1+0.3.

The IR spectra of dust can be modeled by multiplying the blackbody Planck function B_ν by the absorption coefficient Q_{abs} of various grain compositions. The model flux density is then

$$F_\nu = \sum \frac{C_i B_\nu Q_{abs,i}}{a} \tag{3.1}$$

where C_i is a scaling factor for each grain species and a is the grain size. In the Rayleigh limit, where $2\pi a/\lambda \ll 1$, Q_{abs}/a is independent of the grain size. The absorption coefficient depends on the complex dielectric constant ϵ that is related to the indices of refraction n and k by $\epsilon = (n \pm ik)^2$. The optical properties for various grain compositions can be measured in the laboratory by measuring the transmission of individual grain particles or bulk samples. Measurements of n and k can then be used to calculate Q_{abs}

using the equation (e.g. Allen 1973)

$$\frac{Q_{abs}}{a} = \frac{2\pi}{\lambda} \frac{24nk}{(n^2 - k^2 + 2)^2 + 4n^2k^2}. \tag{3.2}$$

This equation is valid in the Rayleigh limit for a spherical grain geometry. Since the geometry of the grains will affect the shape of their emitted spectrum, these effect can be included in the spectral modeling. A common assumption for grain geometry is to assume that they consist of a continuous distribution of ellipsoids (CDE) (Bohren & Huffman 1983; Huffman 1988). Absorption coefficients for CDE grains can also be calculated from the measured indices of refraction. We have used this method of dust modeling to place rough constraints on the grain composition in G54.1+0.3. The results are described in the next section.

3.5.1 The Unidentified 21 μm Feature

The IR spectrum of the shell (Figure 3.6) shows a sharply rising continuum that flattens out beyond 21 μm. The most obvious difference in the high resolution spectra at the two positions in the shell is the strength of the broad emission feature at 21 μm. The feature is much more pronounced in the IR knot than in the rest of the shell. This is best seen in Figure 3.9, where the relative intensity of the emission in the 20.9–21.9 μm range is shown as a function of the position along the LL slit. The precise shape of the spatial intensity plot is affected by the shape of the underlying continuum, but it is obvious that the peak intensity of the 21 μm feature is an order of magnitude brighter at the IR knot. The feature peaks at approximately 20.8 μm and has a FWHM of $\sim$ 3.7 μm, although this estimate is sensitive to the determination of the underlying continuum emission. The shape is asymmetrical; it rises steeply at shorter wavelengths, and falls off more gradually longward of 20.8 μm. Additional features observed in the IR spectra that may or may not be associated with the IR shell are emission features

at $\sim$ 8.6 μm and $\sim$ 12.4 μm, with a FWHM of approximately 1.4 μm and 2.1 μm, respectively. These features are evident in Figure 3.6 and Figure 3.11.

The 21 μm feature in the IR shell of G54.1+0.3 is remarkably similar to the emission feature observed in the IR spectrum of Cas A (Rho et al. 2008). When we overlay our high-resolution spectrum from position 1 with the IRS spectrum of Cas A shown in Figure 3 of Rho et al. (2008), we find that the features peak at the same wavelength and have the same width, implying that they likely arise from the same dust composition. In addition, the spectrum of Cas A also shows the broad emission features at 9 μm and 12 μm that are also evident in our spectrum, suggesting that these emission features may be correlated with the 21 μm feature and produced by the same grain species. Rho et al. (2008) attributed the dust that produces the 21 μm feature to freshly formed dust in the SN ejecta and fitted the spectrum with multiple grain compositions, with the main contribution from SiO_2, Mg protosilicates, and FeO. While the overall continuum was well fitted by this composition, the fit had significant residuals from the 21 μm feature and from the entire broad emission feature at 12 μm. The SiO_2 CDE grain models provided a somewhat better fit to the 21 μm feature in Cas A, in addition to being able to produce the 9 μm feature when modeled at a higher temperature (Rho et al. 2009). In our attempts to fit the spectrum in the shell of G54.1+0.3, we found that the feature produced by the SiO_2 CDE composition was too narrow and peaked at a slightly lower wavelength. However, if the SiO_2 grains are porous, the feature may be broadened and shifted to better match the observed profile. For this reason, these grains are still a plausible candidate for the production of the 21 μm feature in Cas A and G54.1+0.3.

In order to gain insight into other possible grain species that could give rise to the 21 μm emission, we turned to the extensive work that has been done in identifying the "21" μm feature in carbon-rich protoplanetary nebulae (PPNe). The emission was discovered by Kwok et al. (1989) from IRAS observations of PPNe, and has since been

observed in other dusty environments, including planetary nebulae with Wolf-Rayet progenitors and two extreme carbon stars (for a review see Posch et al. 2004). The emission feature observed in these objects actually peaks at a wavelength of 20.1 μm, somewhat lower than the feature in G54.1+0.3. In a recent *Spitzer* study of carbon-rich PPNe, high resolution spectroscopy reveled that the 21 μm emission is accompanied by a narrow emission feature at 11.3 μm and a broader feature at 12.3 μm (Hrivnak et al. 2009), similar to the feature in Cas A and what we observe in the IR shell. This provides some evidence that the features observed at various bands are related and that perhaps the same species give rise to emission in PPNe and in the IR shell of G54.1+0.3.

While various grain species have been proposed as the carriers of the 21 μm resonance feature, including TiC, SiS_2, SiO_2, SiC, and FeO, all but the latter two have been discarded based on abundance constraints and the presence of other unobserved resonance bands (e.g., Zhang et al. 2009; Speck & Hofmeister 2004). In a recent paper, Zhang et al. (2009) ruled out all the mentioned carrier candidates, except FeO, due to an insufficient abundance of Ti, S, or Si in sixteen PPNe. They found that the FeO nano dust can reproduce the 21 μm feature in these sources without producing unobserved secondary features nor exceeding the Fe budget. While FeO is a good fit to the 21 μm feature in PPNe, the peak wavelength of 19.9 μm falls short of the 20.8 μm peak observed in G54.1+0.3 and Cas A. When modeled with FeO grains with a CDE distribution, the peak wavelength of the feature shifts to 20.7 μm, but the FWHM increases to 6.5 μm, far too broad to fit the feature we observe. FeO also fails to produce the other observed emission features at 9 μm and 12 μm that are likely related to the 21 μm feature.

Speck & Hofmeister (2004) suggested that the 21 μm feature may be produced by SiC grains that contain impurities, and through laboratory experiments showed that doped SiC grains do indeed produce a resonance at 21 μm that matches the shape of the feature in PPNe. They also found that nano-SiC grains produce a peak that is

shifted redward by ~ 1 μm, matching the peak of the feature observed in the IR shell of G54.1+0.3 and Cas A. Speck et al. (2005) found that amorphous and nanocrystalline samples all produce three peak complexes near 9, 11, and 21 μm. The SiC grains seem to be able to produce all dust emission features that we observe in the shell of G54.1+0.3, including the sharp emission feature at 11.3 μm, the broader emission features around 9 and 12 μm, and the 21 μm feature with the same peak wavelength as we observe. The relative strength of these features depends on the grain size and shape, and the temperature of the underlying continuum. The strength of the 21 μm feature in particular, likely depends on the amount of carbon impurities in the SiC sample.

Since strong emission from the 21 μm feature is mostly observed in the PPN phase of stellar evolution, Speck et al. (2005) suggest a scenario in which the appearance of this feature is due to the particular physical conditions in these objects, rather than a production of new dust species. The 21 μm emission would be suppressed in regions where the smallest grains have been destroyed by the central star, and in regions of the dust shell where the temperature and density are too low. In this case, the best candidates for the production of the emission feature would be cool ($\sim$ 100 K), micron sized β–SiC and nano-SiC grains that contain carbon impurities (Speck et al. 2005, and references therein). Here, the α-SiC and β-SiC refer to different polymorphs of silicon carbide grains.

The scenario outlined in Speck et al. (2005) appears to be consistent with our observations of the IR shell in G54.1+0.3. The 21 μm feature is strongly pronounced in the densest region, i.e. the IR knot, while it is suppressed in the diffuse shell emission that has a lower density. Our observations seem to suggest that SiC grains are strong candidates for producing the observed emission features. However, based on the models of Kozasa et al. (2009) that predict relative abundances of grain species formed in SN ejecta, SiO_2 may be a more likely candidate. More detailed modeling of the IR spectrum is required to identify the grain composition that produces the 21 μm feature in

G54.1+0.3.

3.5.2 Extended IR Knot

The bright IR knot located in the eastern part of the IR shell is shown in Figure 3.4c, and in Figure 3.5 where the 24 μm emission is shown in blue. The knot consists of three separate clumps of emission whose spatial profiles are broader than the MIPS 24 μm PSF. The extended clumps do not have counterparts at any of the IRAC wavelengths, nor does their emission correlate with the peak brightness of the MIPS 70 μm image. The high-resolution IRS spectrum of the knot is dominated by a broad emission feature around 21 μm and a rising underlying continuum (Figure 3.6). The plot in Figure 3.9 that depicts the spatial variation of emission features across the LL slit shows that the the emission from the 21 μm feature is an order of magnitude brighter at the IR knot than in the rest of the shell. The [SIII] 18.7 μm emission and the ratio of the [SIII] 18.7 μm to 33.5 μm lines also show a peak along the knot, implying a density enhancement in this region. The density calculated from the line ratios in the LH and SH at this position is 1070 $\pm$ 200 cm^{-3}. The pulsar's X-ray jet appears to terminate at the location of the knot (see Figure 3.5), which may be an indication that it is driving a shock into the IR shell and compressing the dust to produce a small dense region with enhanced 21 μm emission. Alternatively, the jet may be interacting with an already dense region and giving rise to strong 21 μm emission. We also note that the 9 and 12 μm features are enhanced at the position of one of the point sources in the SL spectrum (Figure 3.11). If these features correlate with the 21 μm feature, then the 21 μm feature may also be enhanced in the vicinity of the 11 point sources due to a higher temperature, thus causing the unusual [8]–[24] μm color excess in the color–color plots of Koo et al. (2008).

3.5.3 Dust Mass Estimate

Since the spectrum of the IR shell is dominated by the emission from the 21 μm feature, it was difficult to obtain a satisfactory fit to the spectrum with any single grain composition. In order to make a rough estimate of the dust mass in the IR shell, we fit the spectrum of the underlying continuum with two different grain composition models; astronomical silicates (Laor & Draine 1993) and Mg_2SiO_4 (Jäger et al. 2003). We excluded the spectral region from 18–25 μm where the emission from the 21 μm feature dominates. In the fitting, we used the high-resolution spectrum from the diffuse shell emission, position 1, where the 21 μm feature is somewhat suppressed, as well as the MIPS 70 μm data to help constrain the dust temperature. Before fitting, the spectrum was scaled so that the integrated flux over the MIPS 24 μm bandpass is equal to the total extinction-corrected flux at 24 μm of 40 Jy. The fit was not satisfactory since it left large residuals from the 12 and 21 μm features, but it can still be used to make a rough estimate on the amount of silicates that are present in the IR shell. Grains of astronomical silicates at a temperature of $\sim$ 68 K, and Mg_2SiO_4 at $\sim$ 63 K, can approximately match the continuum and the 70 μm data point, excluding the 18-25 μm region and broad emission features at shorter wavelengths. The total dust mass in the shell is given by

$$M_{dust} = \frac{F_\nu d^2}{B_\nu(T_d)} \frac{4\rho a}{3Q_{abs}}, \tag{3.3}$$

where F_ν is the total IR flux, d is the distance, B_ν is the Planck function evaluated at the grain temperature, ρ and a are grain density and size, and Q_{abs} is the absorption efficiency. Absorption efficiencies for 0.05 μm sized astronomical silicates and forsterite are from Laor & Draine (1993) and Jäger et al. (2003), respectively. The assumed distance is 6 kpc. We find an approximate dust mass of 0.016 $M_\odot$ for astronomical silicates, and 0.04 $M_\odot$ for forsterite. Since the fits were not satisfactory for all of the

observed emission features, these values should only serve as rough estimates. We note that this estimate is in the same range as the dust masses of freshly formed dust that have been estimated for other remnants, such as Cas A and E0102 (Rho et al. 2009).

3.6 Physical Interpretation for the IR Shell

The cartoon in Figure 3.12 summarizes the IRS spectroscopic results for different regions of the IR shell surrounding the PWN in G54.1+0.3. The PWN fills the cavity of the IR shell, with the diffuse X-ray emission extending almost to the outer boundary of the MIPS 24 μm emission (Figure 3.5). The dark grey region in Figure 3.12 represents the location where we observe enhanced Si and Ar abundances, and where the intensity of the silicon line shows a sharp rise (see Figure 3.9.) The highest line broadening is also observed in this region (Table 3.6). The diffuse shell emission, represented by light grey, shows lines that are somewhat less broadened and continuum emission with a weak 21 μm dust feature. The pulsar's jet appears to terminate at the bright IR knot whose spectrum shows strong emission from the 21 μm feature and a higher density, as derived from the SIII 18.7/33.5 μm ratio.

The line intensities seem to suggest that the PWN is driving shocks into two distinct types of material; highly enriched ejecta, possibly like that in Cas A, in regions where we observe bright Si and Ar emission; and relatively normal abundance material in other regions. While we can fit the normal abundance spectra with shock models with a shock velocity of $\sim$100 km s^{-1}, it is still possible that this material is also highly enriched, which would introduce additional free parameters to our shock models. In this case, a range of shock speeds would be required to explain the line intensities of different ionization states, similar to what is found for SNR N132D and 1E 0102.2-7219 (Blair et al. 2000).

In this section, we consider two possible physical scenarios that may explain the

observations of the IR shell. A previous explanation is that the shell formed by the progenitor's wind that compressed the surrounding medium and then fragmented and collapsed to form YSOs, as suggested by Koo et al. (2008). An alternative scenario is that the shell is composed of shocked SN ejecta that is being swept up by the PWN, and that the observed point sources are produced by radiative heating of ejecta dust by early-type stars embedded within the expanding SNR. Based on the IR data, and the lack of thermal X-ray emission from the shell, we find the latter interpretation a more plausible explanation for the origin of IR emission in G54.1+0.3.

3.6.1 Preexisting Shell

The 24 μm MIPS image of the IR shell in G54.1+0.3 clearly shows 11 point sources embedded in the diffuse shell emission that are arranged in a ring like structure (Figure 3.4c). Koo et al. (2008) suggest that these point sources are massive pre-main-sequence stars, larger than 10 $M_{\odot}$, with an age of $\lesssim 2$ Myr. Their formation is suggested to be triggered by the progenitor star of G54.1+0.3 during its post-main-sequence stage of evolution. Most of the point sources are detected in IRAC and in the near-IR 2MASS images, and some even have optical counterparts. Their JHK$_s$ color-color and color-magnitude diagrams indicate that they are young stars with spectral types ranging from B1.5 to O8.

Koo et al. (2008) show that the spectral energy distribution (SED) of the brightest star in the K$_s$ band, the southernmost point source in Figure 3.4c, is similar to the SED of early Herbig Be stars. The IRAC and MIPS 24 μm colors, however, are not consistent with the usual colors of Class 0/I and Class II YSOs. While the stars in the IR loop have a small IRAC [3.6]–[5.8] excess, consistent with Class II sources, the [8]–[24] is much stronger than expected, in the 6 to 8.5 magnitude range (Koo et al. 2008). The IR spectrum in Figure 3.6 shows that there is a broad emission feature peaking around 21 μm. This feature likely dominates the MIPS 24 μm flux throughout

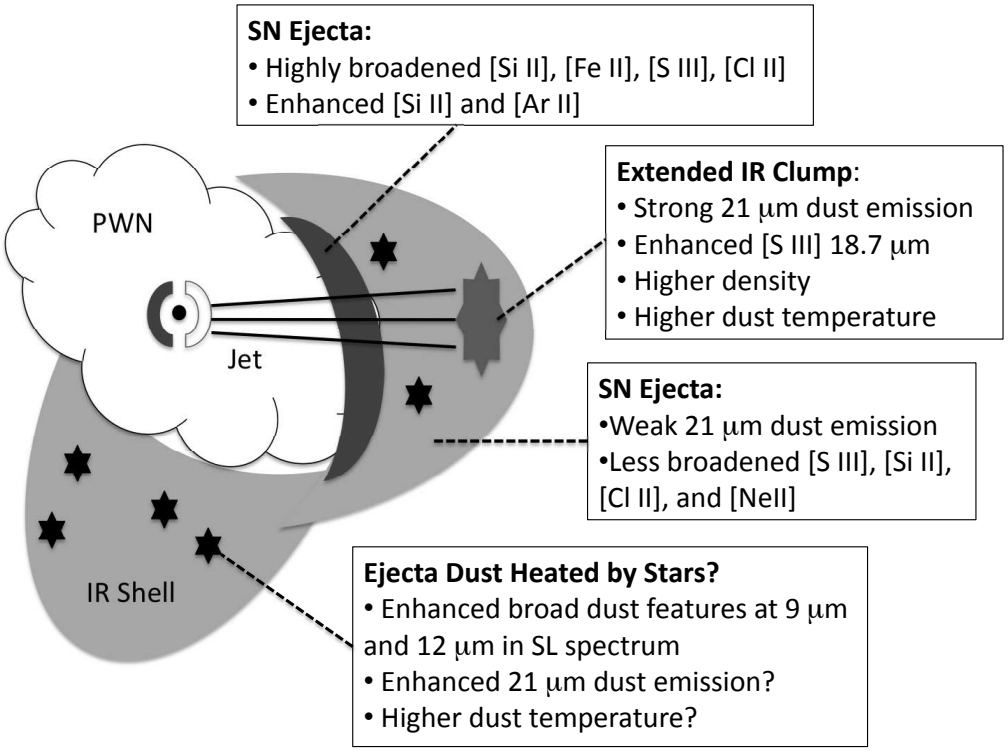

Figure 3.12 Summary of the IRS spectroscopic results for the IR shell in G54.1+0.3.

the diffuse shell, and it may be the cause of the unusually high [8.0]–[24] excess. It may be that the point source photometry is contaminated by the emission from the diffuse shell, but since the observed 24 μm excess is up to 4 magnitudes higher than what is expected for Class II YSOs, it appears more likely that the emission from the 21 μm feature is enhanced in the vicinity of the these sources. A similar enhancement is observed in the IR knot, discussed in Section 3.5.2.

If the point sources in the IR shell are embedded YSOs, their presence would require that the shell was formed prior to the SN explosion. It is possible that the less broadened sulfur and neon lines that correlate with the 24 μm shell emission (Figure 3.9 and Figure 3.10) and a possible narrow component in the profile of the silicon line (Figure 3.8) could originate from such a shell. However, the high expansion velocity of approximately 500 km s^{-1}, as derived from the silicon, iron, and chlorine lines, indicates that these lines have to come from rapidly expanding shocked SN ejecta. The [ArII] 6.99 μm should also originate in the ejecta, since its line intensity is too large to be explained by any shock model with normal abundances (see Section 3.4.5). Another inconsistency with the interpretation of a preexisting shell is the lack of evidence for the interaction with the SN blast wave. If the SNR has encountered the shell, we would expect the reverse shock to have encountered and disrupted the PWN. The structure of the PWN, however, indicates that the reverse shock has not reached its surface, which provides further evidence against this scenario. In the following section, we provide an alternative interpretation for the origin of the IR point sources and the diffuse shell emission, without the need for a preexisting shell.

3.6.2 Swept-up SN Ejecta

Here, we consider a scenario in which the IR shell is composed entirely of SN ejecta. The shock models imply that the PWNe is driving a ~ 100 km s^{-1} shock into expanding SN ejecta, and the broadened line emission suggests an ejecta velocity of ~ 500 km s^{-1}.

The point sources observed at 24 μm can be explained if we consider a scenario in which the SN exploded inside a cluster of young stars. Assuming a distance of 6 kpc, the observed stellar density in the region covering the IR shell is not unusual for a young cluster (e.g. Elmegreen et al. 2000), so such a scenario is not unexpected. In this picture, the SNR blast wave has expanded beyond some of the cluster stars, embedding them within the expanding SN ejecta. The ejecta dust is then blowing by the embedded stars and being radiatively heated. The dust model described in Section 3.6.4 shows that if the dust is heated by a dozen such stars, this can reproduce the observed 24/70 μm ratio and give rise to the IR point sources at 24 μm, without a need for triggered star formation. The fact that the spectrum of the shell closely resembles the spectrum of freshly formed dust in Cas A (Rho et al. 2008) appears to provide additional support for this interpretation.

3.6.3 Origin of Multiple Components

Since the IR spectra show that different emission lines have different spatial and kinematic properties (Section 3.4.2) and that they may arise from distinct components in the shell (Section 3.4.3), it is possible that some of the observed line emission is not produced in shocked ejecta. Intense UV stellar radiation within the stellar cluster may be heating the ejecta gas either by directly ionizing it or by ejecting photoelectrons from grains. Ionization of H and O requires photons with energies greater than 13.6 eV, that may be scarce if only B-type stars were present within the cluster. Abundant, less energetic UV photons that heat the dust also eject photoelectrons. Ejecta gas heated by grain photoelectrons is expected to cool by emission in IR lines of singly ionized species with ionization potentials less than 13.6 eV, including [SiII] 34.8 μm, [FeII] 26.0 μm, and [ClII] 14.4 μm. Heating by grain photoelectrons should be effective both in the ejecta shell swept up by the PWN and in the preshock gas. Since the preshock gas is in free expansion, at sufficiently large distances from the SNR center its

velocity must exceed the shell velocity. If grain heating were still effective there, widths of [SiII], [FeII], and [ClII] lines could be larger than widths of lines such as [SIII] that are produced within the shock-compressed PWN shell. This is what is observed (Table 3.3), suggesting that heating of ejecta gas by grain photoelectrons, and perhaps also by direct photoionization by more energetic photons, occurs in G54.1+0.3.

3.6.4 Origin of IR Point Sources

Here, we describe a model in which the ejecta dust is being heated by stellar sources inside a cluster in which the SN exploded. The stellar radiation field decreases in intensity as r^{-2} with increasing distance r from a star (and steeper still if the dust optical depth τ is non-negligible), so dust is heated to much higher temperatures closer to the star than far away from it. Hotter dust re-radiates the absorbed stellar radiation at shorter wavelengths than the more distant cooler dust, an effect that produces an apparent IR excess in the stellar spectrum. We demonstrate this effect with a simple dust model, which is also used to estimate the total ejecta dust mass in G54.1+0.3.

We consider a B0V star with a luminosity of 25,000 $L_{\odot}$ and temperature of 30,000 K, surrounded by uniformly distributed ejecta dust. There is a central cavity devoid of dust in the immediate vicinity of the star, where dust is cleared either by a stellar wind or by the stellar radiation pressure (Artymowicz & Clampin 1997), but this cavity is expected to be small in view of a large ram pressure exerted by fast-moving SN ejecta. We assume a small cavity radius of 0.003 pc; properties of the mid-IR emission are insensitive to the assumed cavity radius as long as the cavity remains small. Absorption of stellar UV radiation by dust and its re-radiation as thermal dust emission in the IR are modeled as described by Borkowski et al. (1994). These dust models include effects of grain temperature fluctuations that are important for small grains heated by energetic UV photons. Scattering of photons by dust is not included, so these models underestimate absorption if τ is not small. Multiple dust species are predicted to form

in SN ejecta (Kozasa et al. 2009), one of the most abundant being forsterite (Mg_2SiO_4). We considered amorphous forsterite grains in our models, with density of 3.3 g cm^{-3} and optical constants from Scott & Duley (1996). As a single grain size is unlikely, a power law distribution in grain sizes was assumed, with a power-law index of -3.5, ranging in radii from 0.001 μm to 0.25 μm. We chose 0.007 $M_\odot$ pc^{-3} as the grain (mass) density; this corresponds to a dust/gas mass ratio of 0.02 for an ejecta density of 10 cm^{-3} and standard (cosmic) abundances.

Our dust model matches the extinction-corrected 70/24 μm MIPS flux ratio of 1.9 if we choose the radius to which the dust extends to be 0.69 pc. The 70/24 MIPS flux ratio decreases outward, tracing a steep radial dust temperature gradient, so models with a smaller (larger) radius under(over)predict this ratio. We consider only dust within radius of 0.69 pc in our discussion of spatial IR profiles and of dust mass estimates. Within this radius, the IR dust luminosity is 1200 $L_\odot$, comprising of only 4.8% of the stellar luminosity, so the SN ejecta are optically thin to stellar radiation. The predicted surface brightness in the 24 μm and 70 μm MIPS bands is shown in Figure 3.13, without accounting for the limited spatial resolution of *Spitzer*. A sharp, point-like emission enhancement is present at 24 μm, and absent at 70 μm. A comparison with the *Spitzer* PSF (Figure 3.13) reveals that the 24 μm emission enhancement at the center cannot be spatially resolved with *Spitzer*. The uniformly-distributed ejecta dust appears as an unresolved point source, surrounded by a faint extended emission. This is no longer true at 70 μm; emission at this wavelength is predominantly produced far from the star, and the *Spitzer's* spatial resolution becomes adequate for mapping the spatially-extended dust emission. This simple dust model matches well the observed morphology of G54.1+0.3 as seen by the IRAC, MIPS and *Akari* detectors (Koo et al. 2008).

The 70 μm flux, equal to 7.5 Jy in our model with a radius of 0.69 pc, is produced by 0.0097 $M_\odot$ of forsterite dust. Since the total spatially-integrated 70 μm flux is equal

to 76 Jy, the 11 stars with an apparent IR excess identified by Koo et al. (2008) are sufficient to heat ejecta dust with an estimated total mass of 0.1 $M_{\odot}$. This mass dust estimate can be improved once we learn more about these stars from their near IR spectroscopy. In particular, a better understanding of the stellar radiation field in the parent stellar cluster (or association) of the G54.1+0.3 progenitor will allow for a more realistic modeling of dust heating by stellar UV photons than currently possible.

3.7 Conclusions

In this work, we presented deep *Chandra* observations of G54.1+0.3 and *Spitzer* imaging and spectroscopy of the surrounding IR shell. The 300 ks *Chandra* observation was used to derive a new value for the absorbing column density toward G54.1+0.3 that was then used in the IR analysis. We fitted the X-ray spectra from different regions of G54.1+0.3 with an absorbed power-law model and found that a more accurate value of N_H results when the piled-up pulsar region is excluded from the fit. The new value of N_H is $(1.95\pm0.04)\times10^{22}$ cm^{-2}, somewhat larger than the previous estimate by Lu et al. (2002) of $(1.6\pm0.1)\times10^{22}$ cm^{-2}.

The IRAC and MIPS images reveal an IR shell that appears bipolar, a dozen point sources arranged in a ring-like structure, and a dense extended region that is aligned with the pulsar's jet. IRS spectra reveal a number of ionic emission lines, including [ArII], [NeII], [ClII], [SIII], [FeII], and [SiII], and a rising continuum with a broad emission feature at 21 μm. The spectral lines show evidence for broadening with a maximum FWHM of approximately 1100 km s^{-1}, suggesting that these lines arise in SN ejecta shocked by the PWN. Based on shock models of Hartigan et al. (1987), the observed line intensities imply a shock velocity of $\sim$ 100 km s^{-1}, a pre-shock density of 10 cm^{-3}, and a factor of three depletion in refractory elements. The [SIII] 18.7/33.5 μm line ratio is consistent with a low density limit in the IR shell and a higher density in the IR knot of $\sim$ 1000 cm^{-3}. The spatial variations of the line intensities provide

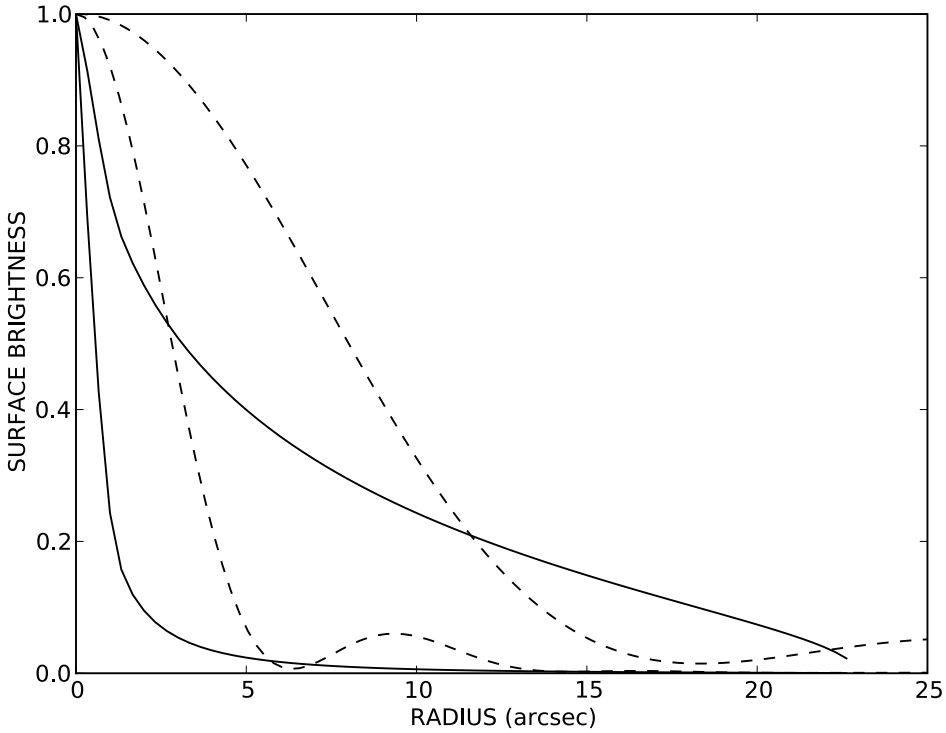

Figure 3.13 Normalized model profiles in the 24 μm and 70 μm MIPS bands (left and right solid lines, respectively). The corresponding *Spitzer's* PSFs are plotted by dashed lines. Because of a large radial gradient in dust temperature, IR emission is spatially extended at 70 μm, but a point-like emission enhancement appears at 24 μm and at shorter IRAC wavelengths.

evidence that the emission originates from physically distinct components. The silicon line shows a sharp peak at the position where the PWN appears to encounter the IR shell, while the sulfur lines correlate with the 24 μm shell emission and do not show any enhancement where the Si line peaks.

The broad 21 μm emission feature is enhanced at the position of the IR knot and weak in the rest of the shell. The profile of the feature is remarkably similar to the spectrum of Cas A (Rho et al. 2008), and is most likely produced by the same dust species. The emission may be caused by SiO_2 grains, as suggested by Rho et al. (2009), but SiC grains are also likely candidates since they are capable of producing the 21 μm feature with a similar profile to what we observe, in addition to other associated emission features around 9 and 12 μm (Speck et al. 2005). We estimate the dust mass in the IR shell to be on the order of 0.1 $M_{\odot}$, assuming a forsterite grain composition. More detailed modeling of the IR spectrum is required to better characterize the properties and composition of the dust.

We find that our observations are best described by a scenario in which the shell emission arises entirely from SN ejecta. In this case, the point sources in the shell would be attributed to radiative heating of ejecta dust by early-type stars that belong to a stellar cluster in which the SN exploded. A simple dust model shows that this scenario can reproduce the observed IR emission, including the IR point sources. If this scenario is correct, the stars are illuminating unshocked dust grains and we are probing freshly formed SN dust before its encounter with the reverse shock. The study of dust production in SNe may prove to be most effective in cases where the SN explosion occurs inside a young stellar cluster.

I would like to thank Alexey Vikhlinin for the ACIS data reduction script, Joe Hora for useful discussion on the 21 μm feature in PPNe, Achim Tappe for tips on CUBISM line intensity maps, Charles Lada for discussion on young stars, Anne Hofmeister for nano-SiC absorbance data, and Jeonghee Rho for the discussion on the 21 μm feature

in Cas A. This work is based in part on observations made with the *Spitzer* Space Telescope, which is operated by the Jet Propulsion Laboratory, California Institute of Technology under a contract with NASA. The IRS was a collaborative venture between Cornell University and Ball Aerospace Corporation funded by NASA through the Jet Propulsion Laboratory and Ames Research Center. SMART was developed by the IRS Team at Cornell University and is available through the *Spitzer* Science Center at Caltech.

Chapter 4

Evolution of PWNe Inside SNRs

4.1 Structure of Composite Supernova Remnants

Composite SNRs are those in which we observe an expanding PWN in addition to surrounding shell-type SNR (Helfand & Becker 1987). The evolution of the PWN in composite remnants is coupled to the evolution of the surrounding SNR, and these systems are perfect laboratories for the study of the interaction between the pulsar wind and the remnant. Examples of composite remnants are shown in Figure 4.1 and a schematic diagram of their structure is shown in Figure 4.2 adopted from Gaensler & Slane (2006). The evolution of PWNe inside SNRs has been studied by several authors and basic picture of the evolutionary stages has been constructed (Reynolds & Chevalier 1984; van der Swaluw et al. 2001; Blondin et al. 2001; Bucciantini et al. 2003; van der Swaluw et al. 2004; Chevalier 2005; Gelfand et al. 2009). Figure 4.2 shows a pulsar in the center of the SNR, surrounded by an expanding pulsar wind with a termination shock radius R_w. The PWN is bounded by a shock driven into the inner SN ejecta at a radius R_{PWN}. In the early stages of PWN evolution, as described in Section 1.3.2, the PWN is expanding supersonically into cold ejecta that is still in free expansion. The Crab Nebula and G54.1+0.3, discussed in detail in Chapters 2 and 3,

are examples of PWNe in this stage of evolution. The outer SNR is still undetected in these cases, presumably because the SN blast wave has not interacted with enough material to produce a detectable SNR and the reverse shock still has not reached the central PWN. The outer SN blast wave sweeps up the surrounding interstellar material, and a reverse shock forms that propagates towards the center, heating the inner SN ejecta. Eventually, the reverse shock reaches the expanding PWN and collides with the nebula, causing a reverberation. After this reverse shock interaction stage, the PWN expands subsonically into SN ejecta, now heated by the reverse shock, and it is no longer bounded by an outer shock. Subsequently, the PWN structure is disrupted and the wind material has mixed with SN ejecta. At this evolutionary stage, we may observe a filamentary morphology and thermal emission from the PWN. If the pulsar has a large space velocity, the late stages of evolution are more complex, as the reverse shock no longer interacts with the PWN symmetrically. The details of this scenario are discussed in Section 4.2.

4.2 Interaction with the Reverse Shock

4.2.1 Symmetric Case

The reverse shock interaction stage of the PWN evolution begins when the SNR reverse shock reaches the surface of the nebula. If the pulsar is not moving with respect to the remnant, the PWN is located at the center of the SNR and the reverse shock collides with the entire surface instantaneously. If the surrounding ISM is inhomogeneous and the SN blast wave encounters denser material on one side, the reverse shock may propagate to the center asymmetrically and crush one side of the PWN first. The asymmetric scenarios will be considered in the next section. When the reverse shock has reached the PWN, it has reheated the inner SN ejecta and the SNR can now be described by the Sedov solution (see Section 5.3). During the reverse shock interaction

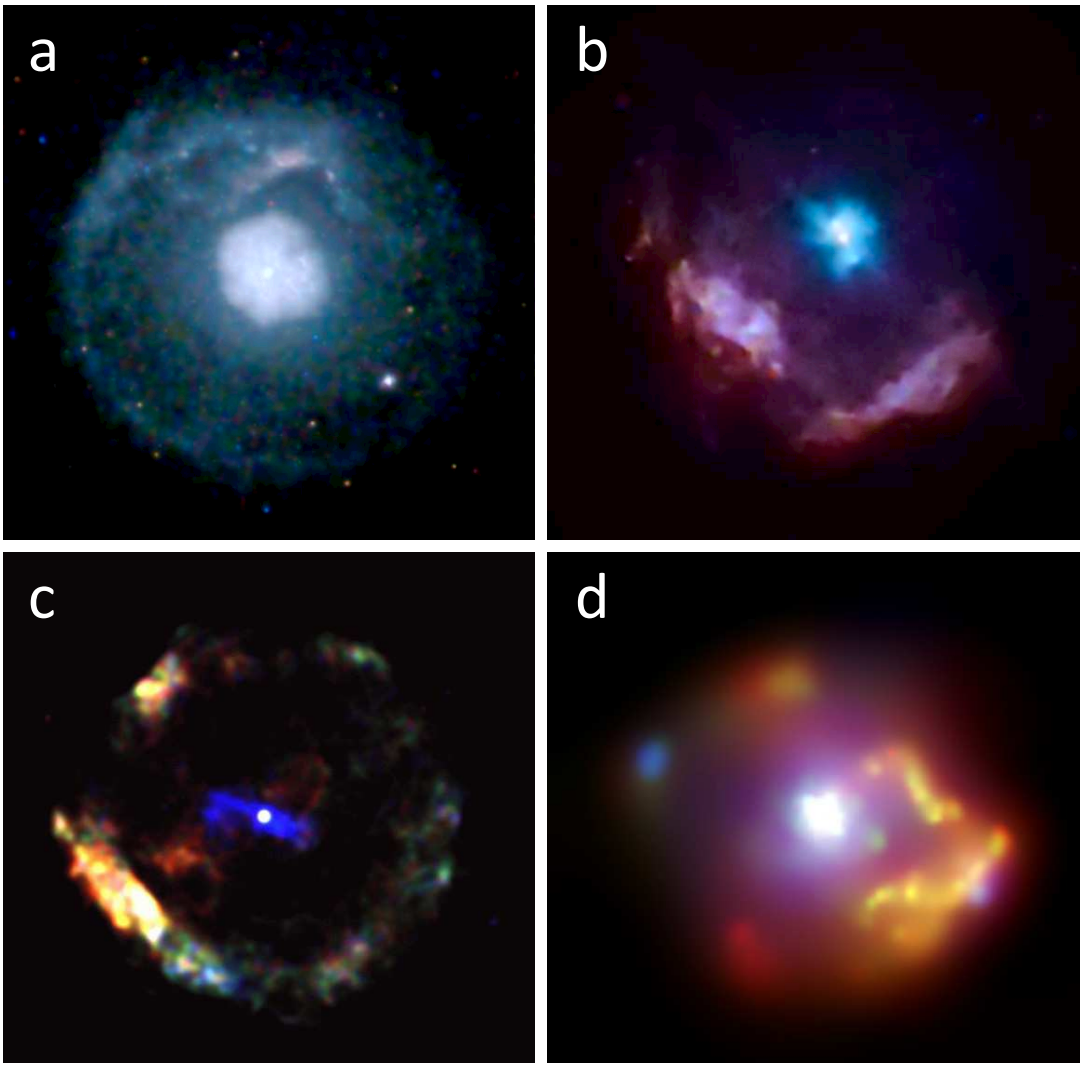

Figure 4.1 Examples of composite SNRs with a central PWN and a shell: a. G21.5-0.9 (NASA/CXC/U.Manitoba/H.Matheson & S.Safi-Harb), b. Kes 75 (NASA/CXC/GSFC/F.P.Gavriil et al.), c. G11.2-0.3 (NASA/McGill/V.Kaspi et al.), and d. SNR 0540-69.3 (NASA/CXC/SAO).

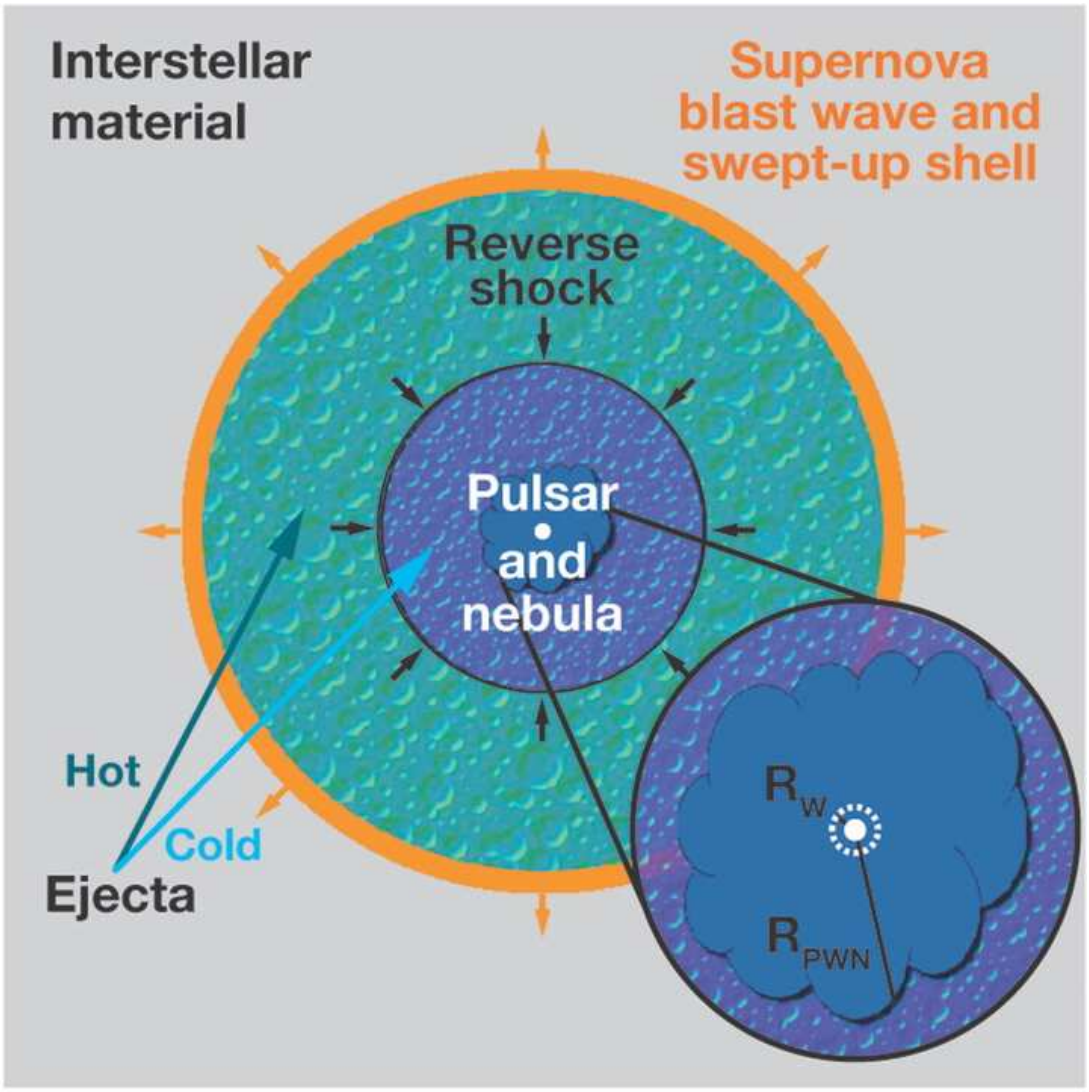

Figure 4.2 Schematic diagram of the basic structure of a composite SNR from Gaensler & Slane (2006). The pulsar and the expanding PWN are located in the center of the SNR. Initially, the PWN expands into cold SN ejecta. The SN blast wave sweeps up the surrounding ISM, forming a reverse shock that heats the inner ejecta. Eventually, the PWN reaches the surface of the PWN and crushes the nebula.

stage, the PWN undergoes reverberations and expands and contracts through adiabatic compression. After the reverberations stop, the PWN expands subsonically into hot ejecta material and there is an approximate pressure equilibrium between the ejecta and the PWN (van der Swaluw et al. 2001). Considering that the interior pressure of the SNR scales as $P_{SNR} \propto E_0/R_{SNR}^3$ and the interior pressure of the PWN scales as $P_{PWN} \propto \dot{E}t/R_{PWN}^3$, van der Swaluw et al. (2001) show that the radius of the PWN expanding in a Sedov-Taylor SNR can be expressed as (van der Swaluw et al. 2001)

$$R_{PWN}(t) = C\left(\frac{\dot{E}t}{E_0}\right)^{1/3} R_{SNR}(t), \tag{4.1}$$

where C is a constant approximately equal to 0.954 for a non-relativistic fluid and 0.851 for a relativistic fluid. Both, R_{PWN} and R_{SNR} are observable quantities in composite remnants and can be used to determine the evolutionary stage of the system and to calculate the age t. We use this approach in the case study presented in Chapter 5.

4.2.2 Moving Pulsar and Asymmetric Reverse Shock

In the case where the pulsar is moving at high space velocity (typically $400-500\mathrm{kms}^{-1}$), the interaction with the reverse shock and the subsequent evolution become more complex. Before the reverse shock interaction, the PWN is centered on the pulsar and becomes displaced from the center of the SNR. As the reverse shock approaches the PWN, it first collides with the side closest to the shock. The collision is not simultaneous across the surface of the nebula, and the collision timescale, t_{col} for the reverse shock to interact with the entire PWN, as derived by van der Swaluw et al. (2004) is

$$t_{col} = 1045 E_0^{-1/2}\left(\frac{M_{ej}}{M_\odot}\right) n_0^{-1/3} \text{ years}. \tag{4.2}$$

This asymmetric interaction significantly alters the morphology of the PWN. van der Swaluw et al. (2004) performed hydrodynamic simulations of this interaction and

described the various observable evolutionary stages, depicted in Figure 4.3. Immediately before the reverse shock interaction, the pulsar and its PWN are off center from the SNR (Figure 4.3a). The reverse shock first collides with the side of the PWN that is closest to it (Figure 4.3b) and it sweeps the nebula to the opposite side of the SNR. What we observe now is a *relic* PWN at the opposite side of the pulsar's motion. This relic nebula has been crushed and mixed with the SN material, so it has a complex filamentary morphology. The relic connects to the moving pulsar that is now forming a new PWN (Figure 4.3c). A similar morphology may be observed with a stationary pulsar and an asymmetric reverse shock. If the pulsar remains in the center of the SNR, and the reverse shock approaches asymmetrically, due to a density gradient in the surrounding ISM, the filamentary morphology is produced. The morphology may become even more complex if both a moving pulsar and density gradient are present. If the velocity of the pulsar that is moving through the SNR becomes supersonic, the newly forming PWN deforms into a bow shock (e.g. van der Swaluw et al. 2004). This scenario is shown in Figure 4.3d and discussed in more detail in the next section.

4.3 Bow Shock Nebulae

As the pulsar moves through the SNR and approaches its edge, the sound speed drops and the pulsar's velocity becomes supersonic. At this point, the PWN around the pulsar deforms into a bow shock. Simulations suggest that the bow-shock formation occurs when the pulsar has reached approximately 2/3 of the SNR's radius (van der Swaluw et al. 2004). In the bow shock stage, the PWN termination shock is shaped by the ram pressure from the pulsar's motion and its radius in the direction of the pulsar's motion is given by

$$r_{w\ forward} = \left(\frac{\dot{E}}{4\pi\omega c \rho_0 V_{PSR}^2} \right)^{\frac{1}{2}}, \tag{4.3}$$

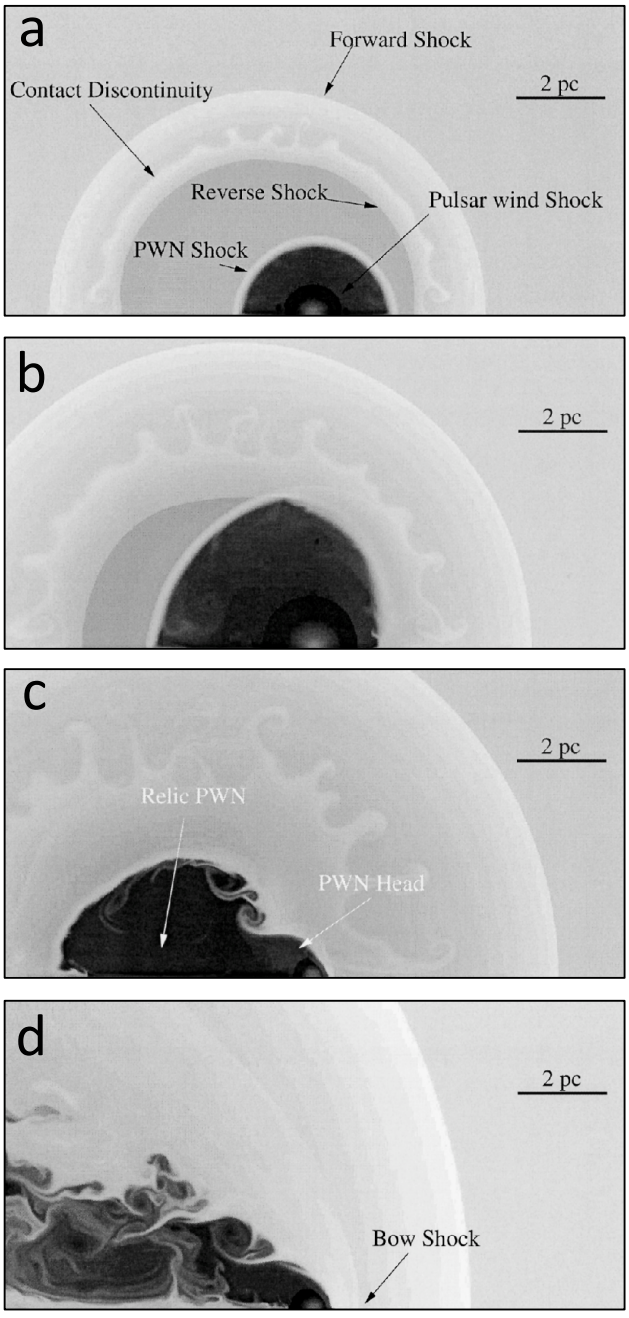

Figure 4.3 Hydrodynamic simulations from van der Swaluw et al. (2004) of an interaction between the reverse shock and the PWN in the case where the pulsar is moving through the SNR at a high velocity.

where ρ_0 is the ambient density (see Gaensler & Slane (2006) for a summary). The termination shock as a function of the forward radius and the polar angle θ is given by (Wilkin 1996)

$$r_w(\theta) = r_{w\ forward} \csc\theta(3 - 3\theta\cot\theta)^{1/2}. \tag{4.4}$$

Simulated bow shock structure is illustrated in Figure 4.4 Gaensler & Slane (adopted from 2006). The bow shock nebula has a cometary morphology; an elongated termination shock region with the shocked pulsar wind trailing behind the moving pulsar. In Chapter 5, a case study of a composite supernova remnant G327.1-1.1 is presented, and the observational properties of bow shock nebulae are discussed in more detail.

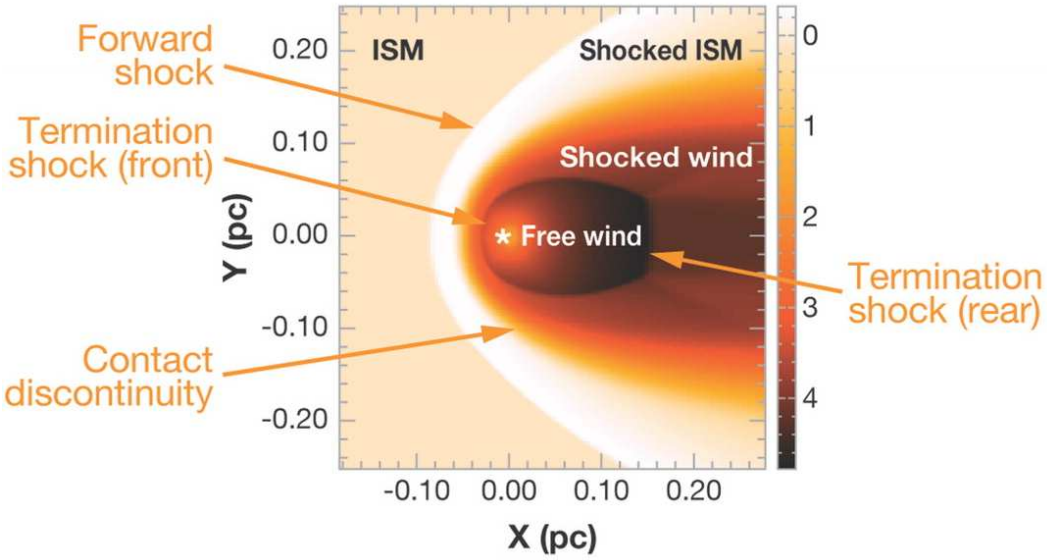

Figure 4.4 Structure of a bow-shock nebula from Gaensler & Slane (2006).

Chapter 5

Chandra and *XMM* Observations of the Composite Supernova Remnant G327.1-1.1

G327.1-1.1 is a composite SNR that is an ideal object for a detailed study of the evolutionary properties discussed in Chapter 4. G327.1-1.1 consists of a thermal SNR shell; a moving pulsar, a relic PWN that was disrupted by the reverse shock, and a newly forming PWN that may have deformed into a bow-shock. In addition to multiple properties that are expected in the evolution of such systems, it also exhibits unusual morphological features that are not easily explained by the current theories and that may provide new details on the evolution of composite SNRs. This chapter describes a study of new high-resolution deep X-ray observations of this unique SNR, obtained with the *Chandra* and *XMM-Newton* observatories.

ABSTRACT

G327.1-1.1 has an unusual morphology consisting of a symmetric radio shell and an off center non-thermal component that indicates the presence of a PWN. Radio observations show a narrow finger of emission extending from the PWN structure towards the northwest. X-ray studies with ASCA, ROSAT, and BeppoSAX revealed elongated extended emission and a compact source at the tip of the finger that may be coincident with the actual pulsar. The high resolution *Chandra* observations provide new insight into the structure of the inner region of the remnant. The images show a compact source embedded in a cometary structure, from which a trail of X-ray emission extends in the southeast direction. The *Chandra* images also reveal two prong-like structures that appear to originate from the vicinity of the compact source and extend into a large bubble that is oriented in the north-west direction, opposite from the bright radio PWN. The emission from the entire radio shell is detected in the XMM data and can be characterized by a thermal plasma model with a temperature of ~ 0.3 keV, which we use to estimate the physical properties of the remnant. The peculiar morphology of G327.1-1.1 may be explained by the emission from a moving pulsar and a relic PWN that has been disrupted by the reverse shock.

This work was carried out under the supervision of Patrick Slane (Harvard-Smithsonian Center for Astrophysics),and in collaboration with B. M. Gaensler (The University of Sydney), John P. Hughes (Rutgers University), and Eric van der Swaluw (Royal Netherlands Meteorological Institute). The results are published in Temim et al. (2009) and have been reproduced here by permission of the AAS.

5.1 Introduction

Composite SNRs are those for which we see distinct evidence of the two fundamental components that characterize the aftermath of massive star collapse. The blast

wave from the explosion sweeps up ISM material and heats it to X-ray emitting temperatures while accelerating electrons that produce radio synchrotron radiation in the compressed magnetic field. The highly magnetic, rapidly rotating neutron star (NS) that is left behind produces a particle wind which sustains an extended broadband synchrotron nebula of magnetic flux and relativistic particles. X-ray observations provide the thermal characteristics of the shell which allow us to constrain the explosion energy, age, and the surrounding ISM density. Simultaneously, the spectral and spatial properties of a PWN allow us to infer the properties of the nebular pressure and magnetic field, and provide constraints on the central pulsar created in the explosion.

G327.1-1.1 is a composite SNR that was originally discovered as a non-thermal radio source by Clark et al. (1973, 1975). It contains a bright central PWN whose structure is complex in both radio and X-ray bands. The radio morphology (Whiteoak & Green 1996) shows a faint shell, 17 arcminutes in diameter, surrounding a bright non-thermal PWN component that is presumably powered by a yet-to-be-discovered pulsar. The bright part of the PWN is located off-center with respect to the SNR shell. A distinct finger-like structure protrudes from the PWN in the northeast direction, possibly suggesting a picture in which a fast-moving pulsar is moving through the SNR, leaving the PWN in its wake. This type of PWN morphology indicates that the reverse shock of the SNR disrupted the PWN (Blondin et al. 2001; van der Swaluw et al. 2004). The X-ray emission from G327.1-1.1 was first detected by Lamb & Markert (1981), who noticed an offset between the peak radio and X-ray emission. The composite nature of G327.1-1.1 was further confirmed by recent X-ray studies, which provide evidence of a compact X-ray source that is the likely counterpart for the pulsar powering the PWN emission (Slane et al. 1998; Sun et al. 1999).

There has been evidence for thermal X-ray emission in G327.1-1.1 in previous studies, but the properties of this component are not well determined. ROSAT PSPC observations by Seward et al. (1996) reveal X-ray emission concentrated at the position

of the PWN with some very faint emission extending outward toward the SNR shell. Using a simple blast-wave interpretation, they conclude that the remnant age is 7000 yr, although this value relies strongly on the inferred temperature of the outer emission component which is not well determined from the ROSAT data. ASCA observations also provide weak evidence for thermal emission with kT $\sim$ 0.4 keV (Sun et al. 1999). Using a Sedov model, the ASCA results imply a remnant age of 11000 yr, a preshock density of $n_0 = 0.1\,\mathrm{cm}^{-3}$, and a swept-up mass of 50 $M_\odot$. BepoSAX observations indicate a temperature of about 0.2 keV, which leads to an age of 29000 yr, $n_0 \sim 0.4\,\mathrm{cm}^{-3}$, and a swept-up mass of 800 $M_\odot$ (Bochinno & Bandiera 2003). In this work, we present *Chandra* and *XMM* X-Ray imaging and spectroscopy of G327.1-1.1, along with the Molonglo Observatory Synthesis Telescope (MOST) 843 MHz observations (Whiteoak & Green 1996) for comparison.

5.2 Observations and Data Reduction

G327.1-1.1 was observed with the Advanced CCD Imaging Spectrometer, ACIS-I, on board the *Chandra* X-ray observatory on 2001 July 15, under the observation ID 1955 and a total exposure time of 50 kiloseconds. The standard data reduction and cleaning were performed in Ciao Version 3.4. The XMM-Newton observations were carried out on 2004 Feb 07 with the MOS1, MOS2, and PN cameras for a total exposure time of 100 ks, under the observation ID 0203820101. The MOS cameras were operated in the Full Frame Mode with a "medium" filter setting, and the PN camera was operated in the Small Window Mode. The standard reduction of the data was performed using the XMM-SAS software, version 7.1.0, and resulted in a final exposure time of 85 ks for each of the MOS detectors, and 82 ks for the PN detector.

5.2.1 Imaging

In order to analyze the X-ray morphology of G327.1-1.1, images in various energy bands were created from the *Chandra* data. Point sources in the field were subtracted from the cleaned event file using the Ciao task *dmfilth*. The missing pixel values for each point source region were replaced by a Poisson distribution whose mean was determined from the pixel values of the background region surrounding each point source. X-ray images and the corresponding exposure maps, were created with a binning factor of 8 and convolved with a Gaussian function with sigma = 3 pixels. Finally, the binned and smoothed images were divided by the exposure maps in order to correct for the differences in the spectral response and effective area across the field.

Images in multiple X-ray energy bands were also created from the cleaned *XMM-Newton* MOS1 and MOS2 event files. Events from the regions that correspond to bright point sources in the field were removed from the data and were not refilled in this case. The images and the exposure maps in the corresponding energy bands were created using the SAS (version 7.1.0) software, with the spatial binning size set to 5″. Since the background in the XMM images includes a non-vignetted component from the internal background and X-ray fluorescence, dividing by the exposure map tends to leave a hollow ring in the images. In order to remove the non-vignetted background component, we used the Filter Wheel Closed (FWC) data provided by the *XMM-Newton* EPIC Background Working Group at the University of Birmingham (http://www.sr.bham.ac.uk/xmm3/BGproducts.html), which are dominated by the internal instrumental background. FWC images of the internal background were created and subtracted from our data, after correcting for the difference in exposure times. Before subtracting the background and dividing by the exposure maps, all the images were smoothed by a Gaussian function with a width of 3 pixels (15″). Finally, the MOS1 and MOS2 images were combined using the SAS task *emosaic* to produce one final MOS image.

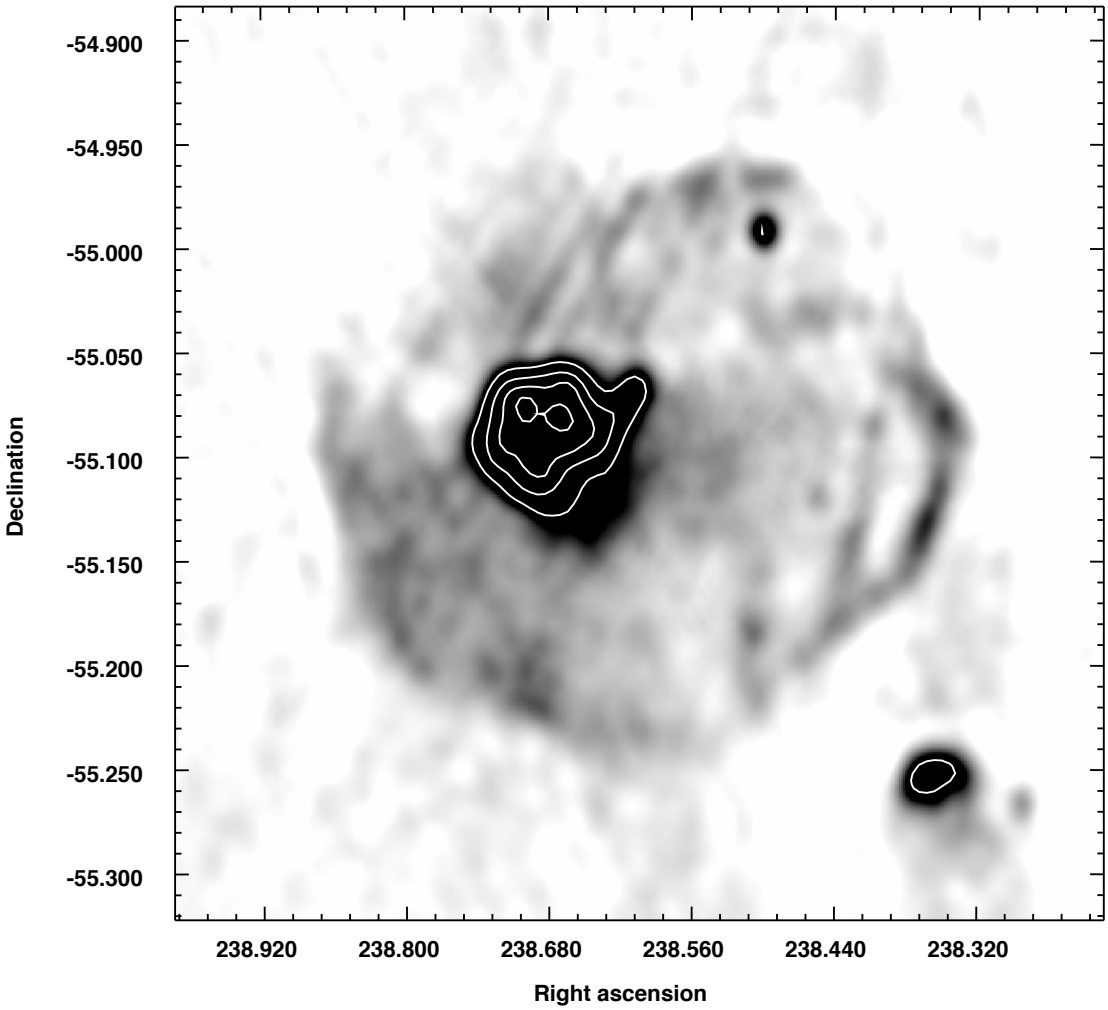

Figure 5.1 MOST 843 MHz radio image of G327.1-1.1 with a resolution of 43″and the PWN region contours overlaid , with levels of 0.05, 0.09, 0.13, and 0.21 Jy/beam Whiteoak & Green (1996). The image shows a faint shell, 17′ in diameter, surrounding a bright non-thermal component, from which a narrow finger of emission extends to the northwest.

5.2.2 Spectroscopy

XMM-Newton MOS spectra were extracted from the cleaned and point source subtracted event files using the SAS (version 7.1.0) *especget* task, which generates spectra and the corresponding effective area and spectral response files. The spectra were extracted from a circular aperture with a radius of 5′.2, centered on the PWN region of G327.1-1.1, and an annulus with an inner radius of 5′.2 and and an outer radius of 11.6 ′ that mostly includes emission from the thermal shell. These regions are shown in Figure 5.4. Since there was no suitable region available for background extraction due to the spatial extent of the source, we used the combination of blank sky background and FWC data to estimate the background. The blank sky background event files were produced by the XMM-Newton EPIC Background Working Group at the University of Birmingham, using observations for many sky positions (Carter & Read 2007). The XMM Newton *Skycast* script was used to project the blank sky and FWC event files into sky coordinates and match it to our dataset. Spectra were then extracted from the same regions as the source spectra and corrected to the same exposure times. The blank sky background data is a combination of the sky background and the internal instrumental background, which can vary as a function of time. In order to determine the possible difference in the internal background levels between our observations and the background datasets, which were taken on different dates, we measured and compared the high energy (10-12 keV) fluxes at the positions of the detector that were out of the field of view. The blank sky high energy flux was found to be lower by 5% and 3% for the MOS1 and MOS2 observations, respectively. The spectra extracted from the FWC data were then multiplied by these factors and added to the blank sky spectra in order to account for the different levels in the internal background and produce a final background spectrum. The final backgrounds were then subtracted from the source spectra and grouped to include a minimum of 100 and 50 counts per bin for the PWN and the shell emission spectrum, respectively.

The *Chandra* ACIS spectra and the corresponding effective area and spectral response files were produced using the *specextract* script in Ciao version 3.4. The spectra were extracted from elliptical apertures shown in Figure 5.3, with each larger aperture excluding the counts from the inner apertures. Since the emission from the remnant covered the majority of the ACIS detector, corresponding background spectra from the same regions were extracted from the ACIS blank sky background files (http://cxc.harvard.edu/ciao/threads/acisbackground/). The blank sky data are produced from observations at various sky positions with high Galactic latitude and have been reprojected to the same sky coordinates as the source event file using the aspect solution for our observation. The background was subtracted and the resulting source spectra were grouped to include 30 counts in each bin for the two smaller apertures and 50 counts in each bin for the two larger apertures. Since G327.1-1.1 is located near the Galactic plane, the blank sky spectra most likely underestimate the background at lower energies, which may result in a residual Galactic background component.

5.3 Analysis

5.3.1 X-ray Morphology

The *Chandra* ACIS raw and smoothed and exposure-corrected X-ray images of G327.1-1.1 in the 0.3-10.0 keV band are shown in Figure 5.2. The MOST radio image is shown in Figure 5.1 for comparison. The radio image shows a symmetric radio shell, 17 arcminutes in diameter, and a bright, off-center non-thermal component from which a narrow finger of emission extends in the northwest direction. The *Chandra* images show a compact source at the tip of this finger and more diffuse X-ray emission elongated in the direction along the finger. The emission from the compact source does not have a profile of a point source, but is slightly extended and may consist of a point source embedded in a more extended region. Figure 5.3 shows the detailed structure of this

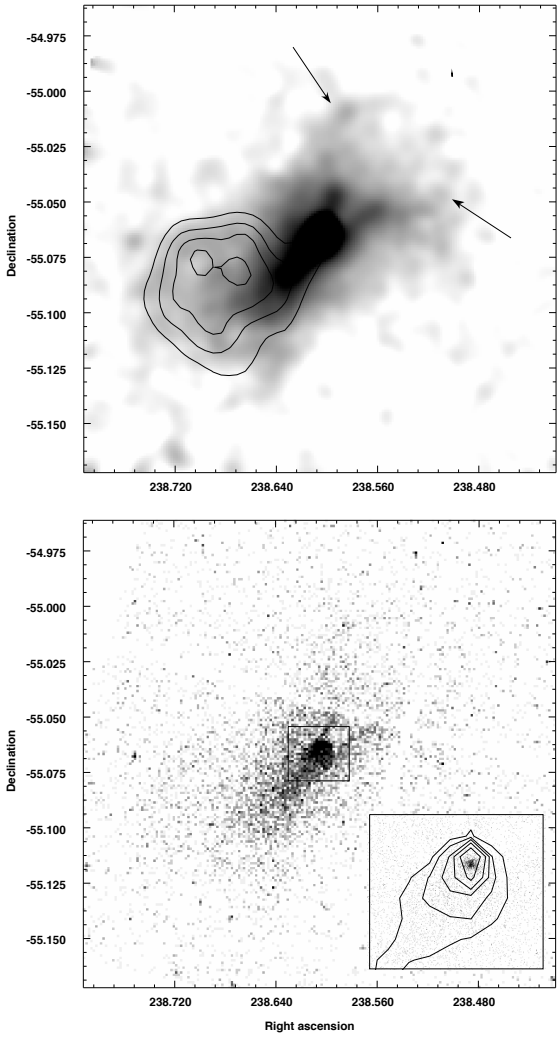

Figure 5.2 The left panel is the exposure corrected and smoothed *Chandra* ACIS image of G327.1-1.1 in the 0.5-10.0 keV band, with the contours of the radio image in Figure 5.1 overlaid. The image reveals a compact source at the tip of the radio finger, from which a trail of X-ray emission extends towards the southeast. A pair of bright prong-like structures originates from the vicinity of the compact source and extends into a large bubble-like structure, indicated by the arrows.The left panel shows the same image, binned by a factor of 8, but unsmoothed. The compact source region in the black box, approximately 1.′5 by 1.′5 in size, is zoomed in at the bottom right corner of the image. The image of the zoomed in region is unbinned and unsmoothed. The contours are the binned and smoothed contours from the same data.

region. The image is binned by a factor of 8, smoothed with a 2 pixel Gaussian, and has not been exposure corrected. The compact source is embedded in a cometary structure from which an X-ray trail extends in the southeast direction. A pair of prong-like structures appears to originate from the vicinity of the compact source and extends out to the northwest. The most unusual feature in the X-ray images is a bubble-like structure that extends out from the prongs. The bubble is approximately 3 arcminutes in diameter and can be seen in both *Chandra* and *XMM* images. The bubble is indicated by the black arrows in Figure 5.2a and is also evident in Figure 5.10, where the unsmoothed *Chandra* image is shown in blue/green and the radio image in red.

In the XMM MOS images, we detect the emission from nearly the entire radio shell. The combined MOS1 and MOS2 image in the 1.0-2.0 keV band, overlaid with the radio contours, is shown in Figure 5.4. The X-ray emission coincides well with the radio contours of the thermal shell. As in the radio image, the non-thermal component in X-rays is displaced from the geometric center of the X-ray shell.

5.3.2 Spectroscopy

In order to determine the general spectral properties of the X-ray emission in G327.1-1.1, spectra were extracted from two different regions in the XMM data, the inner PWN region and the outer shell. A circular aperture 5′.2 in diameter, centered at 15h54m28.2s, -55°03′49.25″ (J2000) was used for the PWN region, and an annulus with the same center coordinates and an inner and outer radii of 5′.2 and 11′.6 was used for the shell region (see Figure 5.4). The spectra were fit with the Ciao 3.4 Sherpa software and are shown in Figure 5.5. The spectra extracted from MOS1 and MOS2 data were fit simultaneously. The absorption column density, photon indices of the power law models, and temperatures of the thermal models were linked for the MOS1 and MOS2 fits, but the normalization parameters of each model were left to vary.

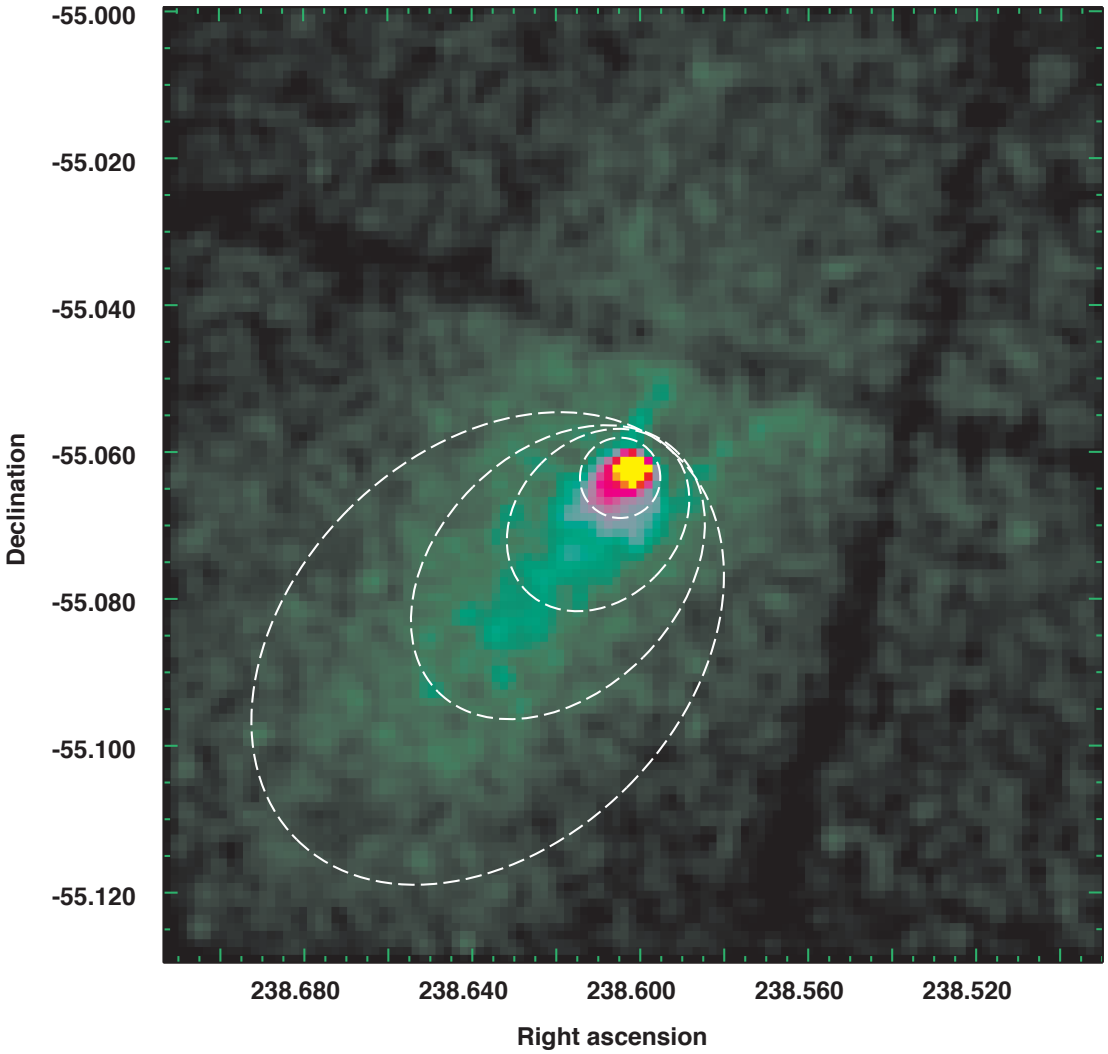

Figure 5.3 *Chandra* ACIS image of the inner region of G327.1-1.1 in the 0.5-10.0 keV energy band. The image was smoothed with a 2 pixel Gaussian function and shows a compact source, embedded in a cometary structure. The white dashed regions are apertures from which spectra were extracted for the *Chandra*-ACIS data (see Section 5.2.2).

The spectrum extracted from the annular aperture and the best fit models are shown in the right panel of Figure 5.5. The emission appears to be thermal in nature and we see evidence of emission lines from NeX, MgXI, and SiXIII. Since we expect most of the emission in the annular aperture to be thermal emission from the shell, we attempted to fit the spectrum with a one component XSPEC Raymond & Smith (1977) thermal plasma model with fixed cosmic abundances. While a one component thermal model can account for most of the emission at lower energies, an additional component is needed in order to account for the excess emission at energies above 2 keV. Due to the high uncertainties in this region of the spectrum, this additional component can be fit equally well with a power law model with a photon index of 2.28 $\pm$ 0.16, or a thermal model with a temperature of 3.3 $\pm$ 0.4 keV. While we cannot rule out the possibility that this residual high energy emission is non-thermal emission from the PWN particles that have diffused out to the outer remnant, in the fitting we assume that this emission is thermal emission from the background. In the final fit, we used a two component thermal model, which resulted in a 0.29 $\pm$ 0.01 keV temperature component that accounts for most of the total observed emission, and a 3.3 $\pm$ 0.4 keV temperature component, most likely due to residual Galactic background emission that was not accounted for by the blank sky background spectra. The summary of the best fit parameters for the shell region is listed in Table 5.1. The listed uncertainties are 90 % confidence, formal statistical uncertainties only.

While the spectrum of the inner PWN region of G327.1-1.1 is dominated by non-thermal emission with a power-law spectrum, it is obvious that an additional component is needed at energies below 2 keV. The spectrum was fit by an absorbed power law plus a thermal model, where the thermal model was the Raymond & Smith (1977) thermal plasma model with fixed cosmic abundances. The 3.3 keV thermal background component, found from the XMM spectral fitting of the shell region, was also added to the fit to account for the residual Galactic background. The temperature and normalization

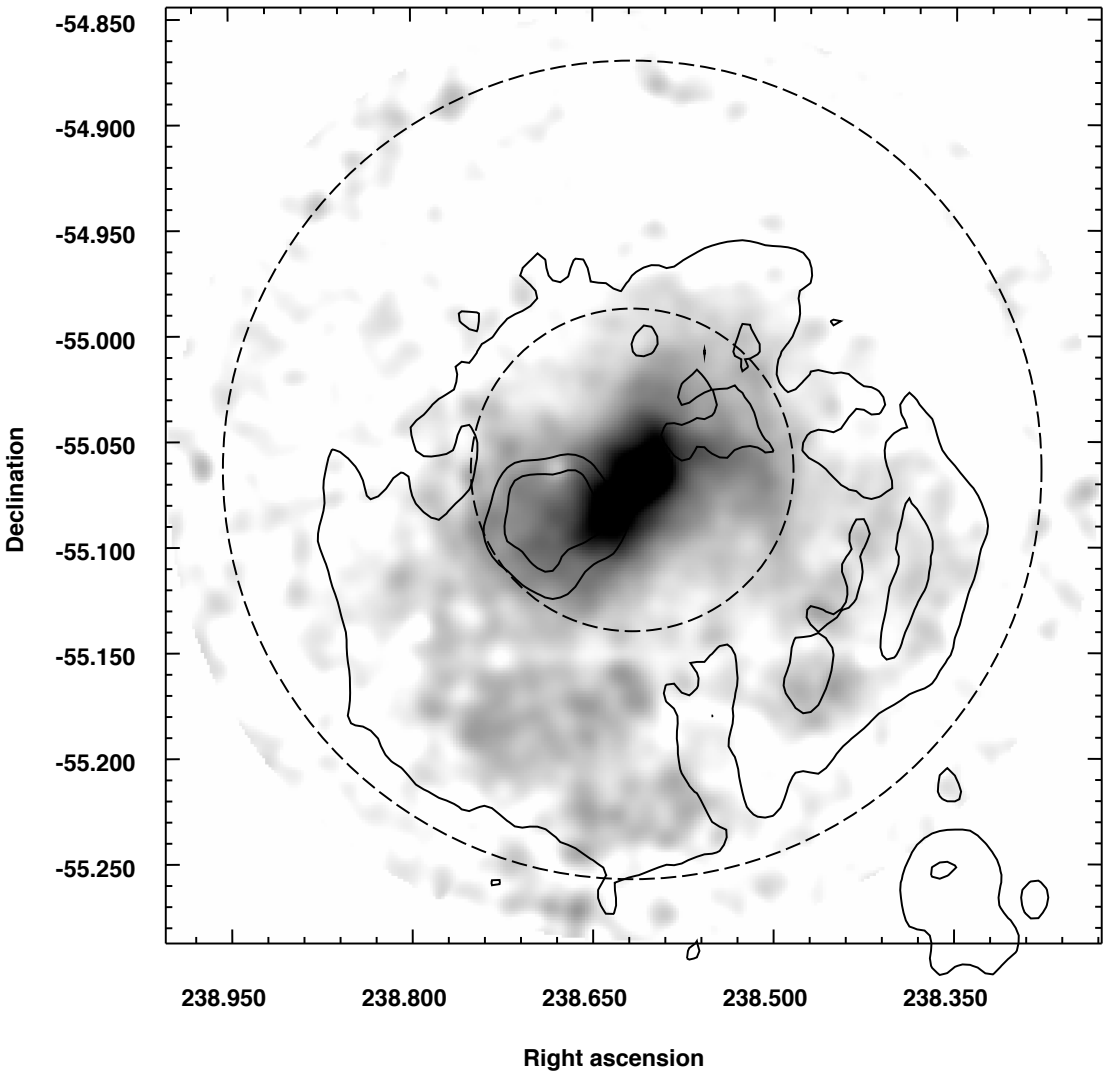

Figure 5.4 XMM-Newton combined MOS1 and MOS2 image of G327.1-1.1, in the 1.0-2.0 energy band, overlaid with the MOST radio contours. X-ray emission from almost the entire shell is detected in the XMM data and coincides well with the radio contours. The dashed circles in black are the spectral extraction regions for the XMM data (see Section 5.2.2).

Table 5.1. G327.1-1.1: XMM Spectral Fitting Results

PARAMETER	PWN	Shell
$N_H(10^{22}cm^{-2})$	1.91 ± 0.07	(1.91)
Photon Index	2.11 ± 0.03	···
kT (keV)	0.29 ± 0.01	0.30 ± 0.01
Residual background temperature (keV)	(3.3)	3.3 ± 0.4
F_X(total observed)$(erg/cm^2/s)$	7.3E-12	4.0E-12
F_X(unabsorbed non-thermal)$(erg/cm^2/s)$	1.7E-11	···
F_X(unabsorbed thermal)$(erg/cm^2/s)$	9.8E-11	2.1E-10
F_X(unabsorbed background)$(erg/cm^2/s)$	1.3E-12	5.1E-12
Reduced χ^2 Statistic	1.08	1.26

Note. — The listed uncertainties are 1.6 sigma (90 % confidence) statistical uncertainties only. The apertures used in the spectral extractions are shown in Figure 5.4, and the spectra and fits are shown in Figure 5.5. The values in parentheses were held fixed. The fluxes were calculated in the 0.3-9.0 keV band and represent the average of the MOS1 and MOS2 flux values.

of the background component, scaled by the difference in extraction areas, were held fixed in the fit. Due do its small contribution, the fit parameters stay roughly the same even if this component is excluded from the fit. The left panel of Figure 5.5 shows the PWN spectrum and the best fit model. The power-law component is shown as the dot-dashed curve, the thermal component as the dashed curve, and the fixed thermal background as the dotted curve. The best fit power-law model has a photon index of 2.11 ± 0.03 and the thermal component has a temperature of 0.29 ± 0.01 keV. The parameters are summarized in Table 5.1.

In order to determine how the spectrum of the non-thermal emission varies with distance from the compact source, spectra were extracted from the *Chandra* ACIS event files using four circular apertures shown in Figure 5.3, where each aperture excludes the counts from the enclosed apertures. For more details about background subtraction, refer to Section 5.2.2. Each of the spectra were fit with an absorbed power law plus

Raymond & Smith (1977) thermal plasma model whose temperature was fixed to 0.29 keV, as determined from the spectral fitting of the XMM-observed shell emission. The contribution from the residual 3.3 keV background component, found in the fitting of the XMM-observed shell emission, is negligible compared to the non-thermal emission inside the ACIS apertures and was not included in the fit. The value of N_H was fixed to 1.91×10^{22} cm^{-2}, the value found from the XMM data. The spectra and best fit models are shown in Figure 5.6 and the best fit parameters are summarized in Table 5.2. As expected, the emission across the PWN is dominated by non-thermal emission, but the spectrum extracted from the larger aperture clearly requires an additional thermal component at energies below 2 keV. The best fit values for the photon indices show that the spectrum is steepening with distance from the compact source. This is consistent with the synchrotron burn-off of high energy electrons at larger distances from the compact source.

5.3.3 Timing Analysis

The *XMM* PN data in the small window mode (6 ms time resolution) was used to search for the pulsed signal from the compact source in G327.1-1.1. Events in the 0.5-10.0 keV and 2.0-7.0 keV bands were extracted from a circular aperture with a radius of 20″, centered on 15h54m24.5s, -55°03′45.1″ (J2000) (see Section 5.6.2). We used the Z_n^2 test (Buccheri et al. 1983) with one harmonic to perform a timing analysis on a total of ∼6900 events between 0.5-10 keV and ∼4000 events between 2.0-7.0 keV, 50% of which can be attributed to the compact source, and the rest to the local background. In Section 5.6.2, we show that the spatial structure of the compact source in the *Chandra* data is composed of a point source embedded in a more extended structure that accounts for the majority the emission. When we fit the extended component with a Gaussian, the point source, assumed to be the pulsar, accounts for less than 10% of the total flux in the compact source. This makes it undetectable above the local background, even

with pulsed fraction of 100 %. It may be possible that the point source contributes a larger fraction to the total flux, since the spatial profile of the underlying extended component is unknown. We searched for periodicity in the 10^{-5} to 83 Hz frequency range, with a step size of 3×10^{-6} Hz, a factor of 3 oversampling compared to 1/T, where T is the duration of the observation. We found no peaks with a probability below 10^{-3}, representing a 3-sigma confidence level.

Table 5.2. G327.1-1.1: *Chandra* ACIS Spectral Fitting Results

PARAMETER	Region 1	Region 2	Region 3	Region 4
Area (arcsec^2)	1216	6124	15395	40105
Photon Index	1.65 ± 0.13	1.80 ± 0.13	2.03 ± 0.12	2.14 ± 0.14
F_X(total observed)($erg/cm^2/s$)	7.8E-13	7.9E-13	9.1E-13	1.0E-12
F_X(unabsorbed non-thermal)($erg/cm^2/s$)	1.4E-12	1.6E-12	2.2E-12	2.7E-12
F_X(unabsorbed thermal)($erg/cm^2/s$)	···	2.1E-12	4.0E-12	1.5E-11
Reduced χ^2 Statistic	0.6	0.7	1.0	0.6

Note. — The extraction regions are shown in Figure 5.3. Listed uncertainties are 1.6 sigma (90 % confidence) statistical uncertainties from the fit. The spectra and fits are shown in Figure 5.6 and the fluxes were calculated in the 0.3-9.0 keV band.

5.4 Thermal Emission

XMM images of G327.1-1.1 reveal emission from the entire shell structure observed in the radio. Figure 5.4 shows the XMM image in the 1-2 keV band overlaid with the MOST radio contours, which coincide extremely well with the X-ray emission. Spectral fitting of the shell region indicates that the emission is thermal and well described by a 0.3 keV thermal plasma. We used the best fit temperature of the thermal shell to estimate the physical properties of the remnant based on the Sedov (1959) simple blast wave model, in which a SN with the explosion energy of E_0 expands into an ISM with a uniform density, n_0. We assume that the ISM is compressed into a shell with four times the initial ambient density, and a thickness of 1/12 of the remnant radius, R. In our calculations, we also assume a complete shell, a remnant radius of $8\farcm5$, as measured from the radio image, and equal ion and electron temperatures. The distance to G327.1-1.1 is not well determined and introduces the greatest uncertainty in the derived parameters. We adopt a distance of 9.0 kpc, which was estimated by Sun et al. (1999) based on the statistical relation between the hydrogen column density in the X-ray band and E(B-V) (Ryter et al. 1975), and the relation between E(B-V) and distance (Lucke 1978).

The following equations were used to calculate the remnant radius, R, shock velocity, v_s, and the ISM density, n_0, where the last equation is based on the fitted intensity of the X-ray spectrum and the assumed geometry. The equations are given as a function of the angular size of the remnant in arcminutes, R_{ang}, the distance in kiloparsecs, D_{kpc}, and the shell temperature, T_{keV}.

$$R(pc) = 0.291 R_{ang} D_{kpc} \tag{5.1}$$

$$v_s(km\ s^{-1}) = 928 T_{keV}^{1/2} \tag{5.2}$$

$$n_0(cm^{-3}) = 9.14 R_{ang}^{-3/2} D_{kpc}^{-1/2} \tag{5.3}$$

The Sedov (1959) model yields the following relations for the remnant age, t, SN explosion energy, E_0, and the swept up mass, M.

$$t(yr) = 124 R_{ang} D_{kpc} T_{keV}^{-1/2} \tag{5.4}$$

$$E_0(10^{51} erg) = 2.87 \times 10^{-4} R_{ang}^{3/2} D_{kpc}^{5/2} T_{keV} \tag{5.5}$$

$$M(M_\odot) = 5.22 \times 10^{-3} R_{ang}^{3/2} D_{kpc}^{5/2} \tag{5.6}$$

The derived values for G327.1-1.1 are listed in Table 5.3 and appear to be reasonable for a remnant in the Sedov-Taylor stage. Since the model assumes a uniform ambient density, and a single average thermal temperature, the derived parameters have unquantifiable uncertainties due to uncertainties in the distance and the likely inhomogeneities in the ambient ISM that would cause variations in density and temperature across the shell.

5.5 Non-thermal Emission

The central part of G327.1-1.1 is dominated by a non-thermal X-ray component whose total emission can be described by a power-law model with a photon index of 2.08 $\pm$ 0.03, typical for a PWN. The X-ray data provide evidence for the existence of a pulsar powering the PWN. Based on the empirical relationship between the pulsar's current spin-down energy loss rate and the luminosity of the non-thermal emission (Seward & Wang 1988), Sun et al. (1999) estimated a pulsar period (P) of 62 ms, period derivative

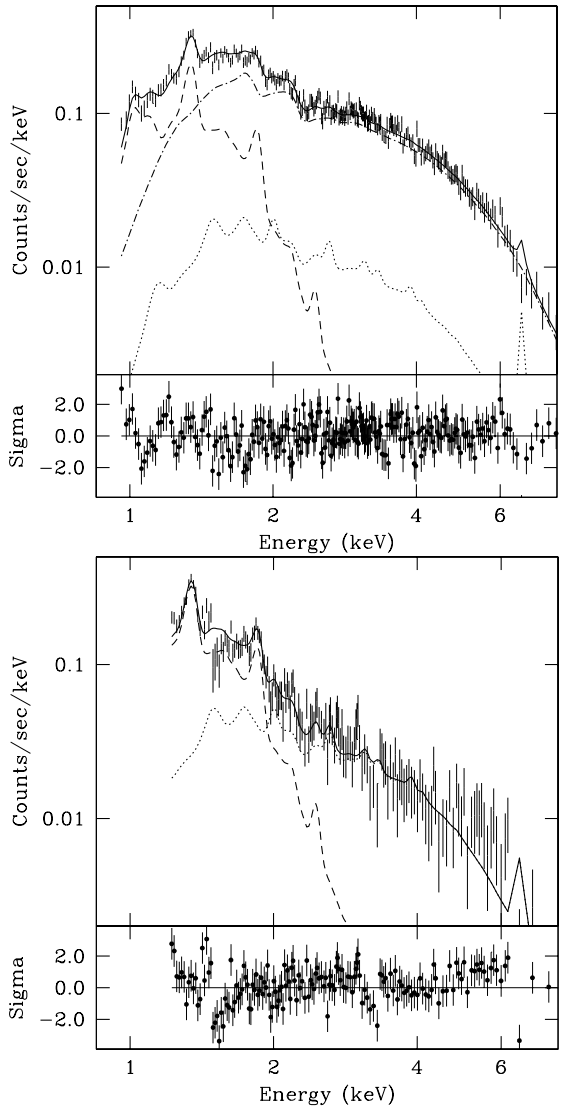

Figure 5.5 Spectra extracted from the XMM MOS1 data of the PWN region (left) and shell region (right). The solid lines represent the two component best fits to the spectra with the individual components shown as dotted and dashed curves. The PWN components are a power-law (dot-dashed curve), 0.3 keV thermal model (dashed curve), and the 3.3 keV thermal model attributed to the residual Galactic background (dotted curve). The shell components are a 0.3 keV thermal model (dashed curve) and the same 3.3 keV thermal residual background (dotted curve). The extraction apertures are shown as dashed circles in Figure 5.4. The PWN spectrum was extracted from the inner circle and the shell spectrum from the annulus defined by the two circles. The best fit parameters are listed in Table 5.1.

Table 5.3. G327.1-1.1: Input and Derived Properties for the Sedov Model

Property	Value
D(kpc)	9.0
T (keV)	0.3
R(pc)	22
v(km/s)	500
t(yr)	18000
$n_0(cm^{-3})$	0.12
M ($M_\odot$)	31
E_{51} ($10^{51} erg$)	0.5

Note. — A distance of 9.0 kpc was assumed in the calculations.

($\dot{P}$) of $8.9 \times 10^{-14}\, s\, s^{-1}$, and a surface magnetic field (B_0) of $2.3 \times 10^{12} G$. In this section, we follow the discussion by Sun et al. (1999) and derive the same pulsar and PWN properties for comparison. We assume the same distance of 9.0 kpc and the remnant properties that we derived in Section 5.4 (Table 5.3).

The unabsorbed flux from the non-thermal component in the XMM data is $8.0 \times 10^{-12}\,\mathrm{erg\,cm^{-2}\,s^{-1}}$ in the 2-10 keV band. Based on a more recent relationship between the pulsar's spin-down energy loss rate and the non-thermal luminosity, $logL_{X,(2-10keV)} = 1.34 log\dot{E} - 15.3$ (Possenti et al. 2002), and a distance of 9.0 kpc, this yields a spin-down energy, $\dot{E}$, of $2.8 \times 10^{37}\,\mathrm{erg\,s^{-1}}$. Using an SNR age of 18000 yr, we derive the following values; $P = 35ms$, $\dot{P} = 3.1 \times 10^{-14}\,\mathrm{s\,s^{-1}}$, and $B_0 = 1.0 \times 10^{12}$ G. Due to the very large uncertainties associated with the distance and age of G327.1-1.1, the calculated values are only rough approximations and are consistent with previous estimates by Sun et al. (1999).

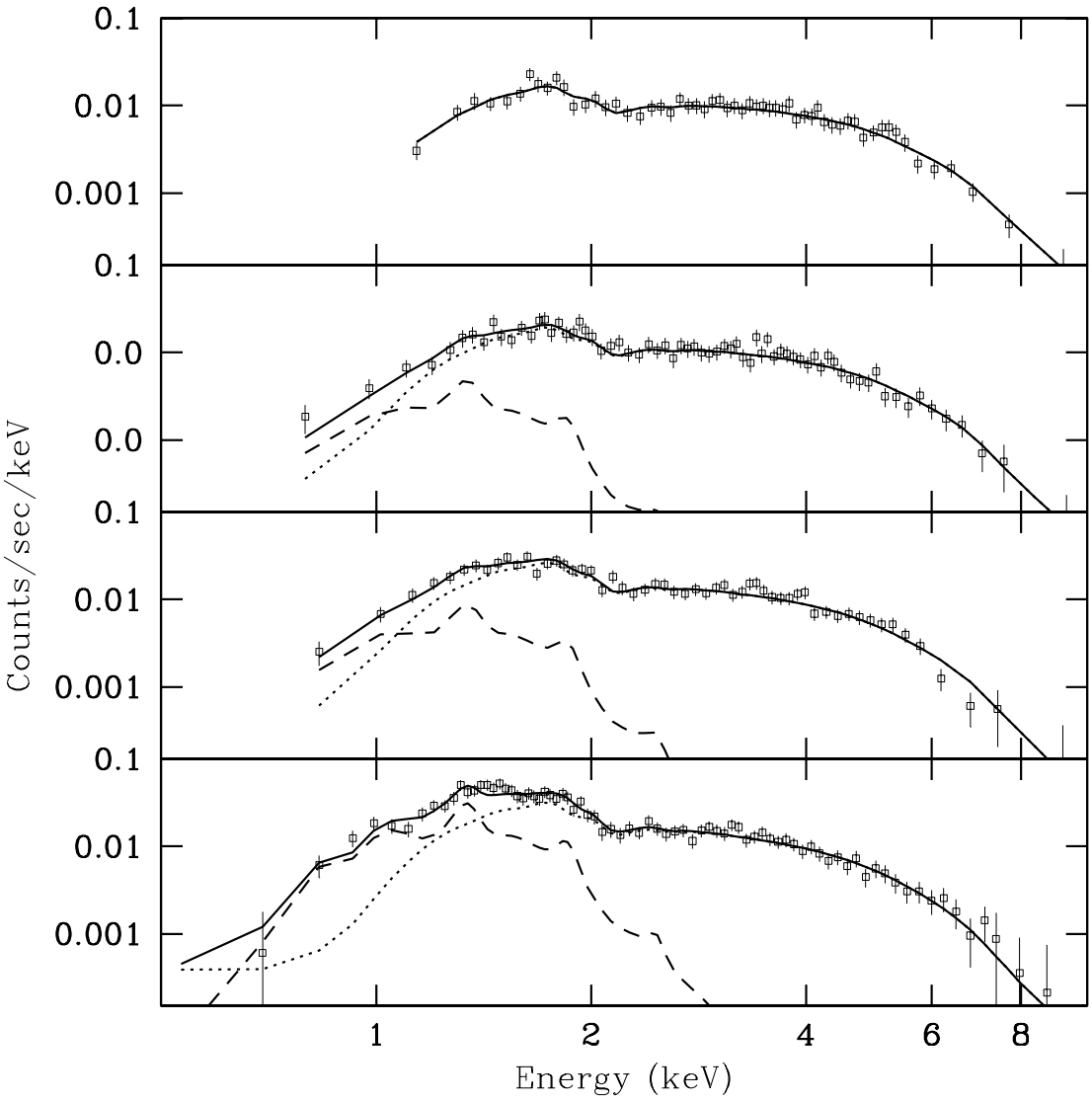

Figure 5.6 Spectra extracted from the *Chandra* ACIS data using the elliptical apertures shown in Figure 5.3. Each of the larger apertures excludes the counts from the inner ones and the spectral plots (top to bottom) are ordered by the aperture size (smallest to largest). The solid line represents the best fit two component model, power-law and thermal. The individual components are represented by dashed curves for the thermal component and dotted curves for the power-law component. The best fit parameters are listed in Table 5.2.

5.6 Evolution and Morphology

The evolution of a PWN inside a composite SNR can be divided into three stages when the pulsar is not moving; the supersonic expansion stage, the reverse shock interaction stage, and the subsonic expansion stage. In the initial supersonic expansion stage, the PWN is bounded by a strong shock as it expands into the surrounding SN ejecta. The reverse shock eventually encounters the PWN surface and crushes the nebula, causing it to reverberate. After the reverse shock interaction stage, the PWN continues to expand subsonically into the SN ejecta that has been heated by the reverse shock (van der Swaluw et al. 2001; Blondin et al. 2001).

In the case where the pulsar is moving through the SNR at a high velocity, as it appears to be the case for G327.1-1.1, the evolution and morphology become much more complex. Initially, the PWN is carried along with the moving pulsar and the reverse shock first interacts with the PWN surface that is closest to the SNR shell. The PWN is swept away from the pulsar, resulting in a relic PWN that is located at a position opposite of the pulsar motion. After the passage of the reverse shock, the moving pulsar continues to generate a PWN that is now expanding subsonically into the reheated SN ejecta and is connected to the old, relic PWN. An additional stage of PWN evolution becomes evident when the pulsar's velocity becomes supersonic and the head of its PWN deforms into a bow shock (van der Swaluw et al. 2004).

In the case of G327.1-1.1, we observe a bright radio PWN, which may be interpreted as the older, relic PWN, left behind after the passage of the reverse shock. van der Swaluw et al. (2004) gives an expression for the timescale, t_{col}, for the reverse shock to collide with the entire PWN surface,

$$t_{col} = 1045 E_{51}^{-1/2} \left(\frac{M_{ej}}{M_{\odot}} \right)^{5/6} n_0^{-1/3} yr, \tag{5.7}$$

where E_{51} is the explosion energy in units of $10^{51}\ erg$, and M_{ej} is the ejected mass.

Assuming an ejected mass of $10M_{\odot}$, and using the derived values from Table 5.3, we find the timescale for the reverse shock collision to be on the same order as the derived SNR age of 18000 yr. This suggests that the PWN is either still in the reverse shock interaction stage, or that the reverberations from the collision between the reverse shock and the PWN have died out and the expansion of the overall PWN structure has become subsonic. The displacement of the relic PWN in G327.1-1.1 cannot be explained by the asymmetries due to the pulsar motion alone. Its displacement is not aligned with the X-ray trail or the radio finger, but is instead located further to the east. In order to explain the displacement of the PWN from the center of the SNR shell, a combination of the pulsar motion and an asymmetric reverse shock may be required.

Chandra observations clearly show that the compact source is surrounded by an extended, cometary structure, with an average radius of approximately half an arcminute (see Figures 5.2,5.3, and 5.8). According to hydrodynamic simulations of van der Swaluw et al. (2004), there are two possible scenarios that may give rise to this type of morphology. The pulsar may be moving at a supersonic velocity with respect to the SNR, causing the PWN to deform into a true bow shock, or the reverse shock has disrupted the PWN from the NW, giving rise to the cometary morphology.

5.6.1 Pulsar Velocity and Bow Shock Formation

The formation of the bow-shock is expected to occur at half the crossing time, t_{cr} (defined as the age of the remnant when the pulsar reaches the SNR shell), assuming that the remnant is in the Sedov-Taylor stage (van der Swaluw et al. 2003);

$$t_{cr} \simeq 1.4 \times 10^4 E_{51}^{1/3} V_{1000}^{-5/3} n_0^{-1/3} yr, \tag{5.8}$$

where V_{1000} is the pulsar velocity in units of $1000\,\mathrm{km\,s^{-1}}$. At this time, the pulsar is positioned at a distance equal to two thirds of the blast wave radius, R (van der Swaluw

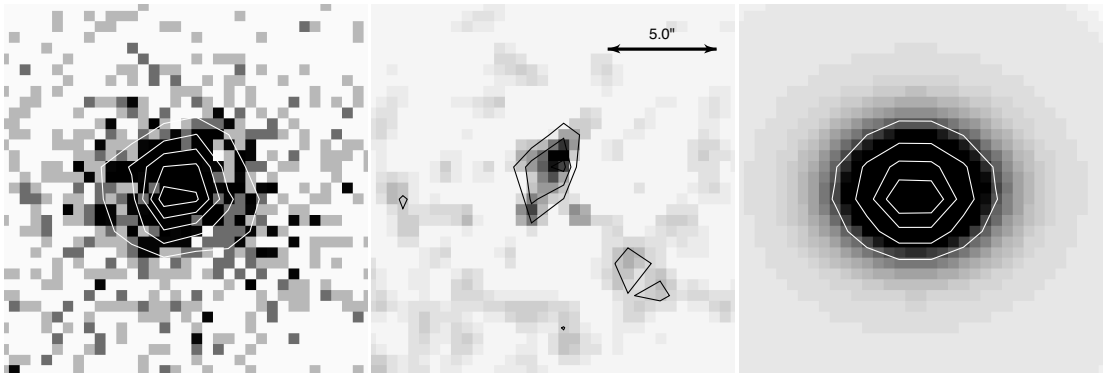

Figure 5.7 The left panel shows the unsmoothed *Chandra* image of the compact source region. The right panel is the image of the best fit model to the compact source emission, consisting of a point source and a more extended Gaussian component. The middle panel is the residual image. All three panels are displayed on the same linear scale from 0-16 counts.

et al. 2004). Using the physical parameters for G327.1-1.1, we find that the pulsar velocity would need to be $\sim$ 770 km s^{-1} in order for the current age of the remnant to be larger than half the crossing time t_{cr}. This is the pulsar velocity required for the bow-shock formation to have already taken place in G327.1-1.1. The approximate displacement of the compact source in G327.1-1.1 from the geometric center of its radio shell is 7.5 parsecs. This is also the approximate length of the radio finger, which is presumably the pulsar trail. Using this projected distance and the derived age, we calculate the tangential pulsar velocity to be on the order of $\sim$ 400 km s^{-1}. This would require a 30 degree angle between the pulsar velocity and the line of sight to achieve a velocity of 770 km s^{-1}, required for bow-shock formation. While the required pulsar velocity is somewhat high for a typical pulsar, it is not entirely unreasonable and cannot discount the possibility that the structure in Figure 5.3 is the head of the PWN that has already been deformed into a bow shock.

5.6.2 Spatial Modeling of the Compact Source

At the tip of the radio finger, the *Chandra* image shows a compact source whose spatial profile is significantly more extended than that of a point source (see Figure 5.2b). Figure 5.9 shows the contours and scales for the three main emission regions in the *Chandra* image, the compact source region in the innermost contour, the cometary region in the middle contour, and the elongated X-ray emission that is coincident with the radio finger in the outer contour. We used Sherpa to spatially fit the unbinned image of the compact source region in the 0.3 to 9.0 keV energy band. The fitting was performed on a circular section of the image, 24 pixels ($\sim$ 12 $''$) in radius, centered on the brightest region of the compact source. A normalized image of a 3 keV point spread function, generated with the Ciao tool *mkpsf*, was used as a convolution kernel in the fitting. We used a model consisting of a delta function plus a Gaussian, and a level offset for the local background surrounding the compact source. The spatial

profile and the best fit model are shown in Figure 5.8a. The best fit model consists of a delta function with an amplitude of 48±19 counts, a Gaussian with a fwhm of $5\farcs5 \pm 0\farcs5$, and an ellipticity of 0.21±0.08, and a background offset of 1.1 counts arcsec^{-2}. The quoted uncertainties represent 1-sigma errors on the fitted parameters. The center coordinates of the delta function and the Gaussian components are 15h54m24.5s, -55°03′45.1″ (J2000), and 15h54m24.4s, -55°03′44.6″ (J2000), respectively. The total fluxes inside the 12 ″radius aperture are 48 counts in the point source component and 749 counts in the extended, Gaussian component. The best-fit values are summarized in Table 5.4. Figure 5.7 shows the *Chandra* image of the compact source region in the left panel, the image of the best fit model in the right panel, and the residual image in the middle panel. We note that the residual image shows a slightly elongated knot of emission, approximately 4″in length, that originates near the peak of the point source and extends to the northwest. The residual emission in the brightest pixels of the knot is approximately 5 sigma above the noise.

The results of the fitting suggest that the emission originates from a point source, assumed to be the pulsar, embedded in a more extended structure which accounts for 94 % of the compact source flux. A similar type of emission was seen in the Mouse (Gaensler et al. 2004) bow shock nebula, where the X-ray emission from its compact source is also composed of a point source embedded in a broader component, $2\farcs4$ in size. In the Mouse, this emission is contained within the termination shock of the pulsar and it was attributed to X-ray knots that are produced in its vicinity (Gaensler et al. 2004). In the case of G327.1-1.1, the size of the extended component is much broader, ∼12″in diameter, and the emission is surprisingly uniform. A possible explanation for the origin of this emission is the shocked pulsar wind downstream of the termination shock, which would require the boundary of the shock to be on a much smaller scale than the spatial extent of the compact source and well within the innermost contour of Figure 5.9.

Table 5.4. G327.1-1.1: Best-fit Parameters for the *Chandra* Spatial Modeling of the Compact Source

PARAMETER	Value
Delta Function	
Center coordinates	15:54:24.5, -55:03:45.1
Amplitude	48 ± 19 *counts*
Total flux	48 *counts*
Gaussian	
Center coordinates	15:54:24.4, -55:03:44.6
FWHM	$5\farcs5 \pm 0\farcs5$
Ellipticity	0.21±0.08
Total flux	749 *counts*
Background level	
Amplitude	1.1 $counts\, arcsec^{-2}$

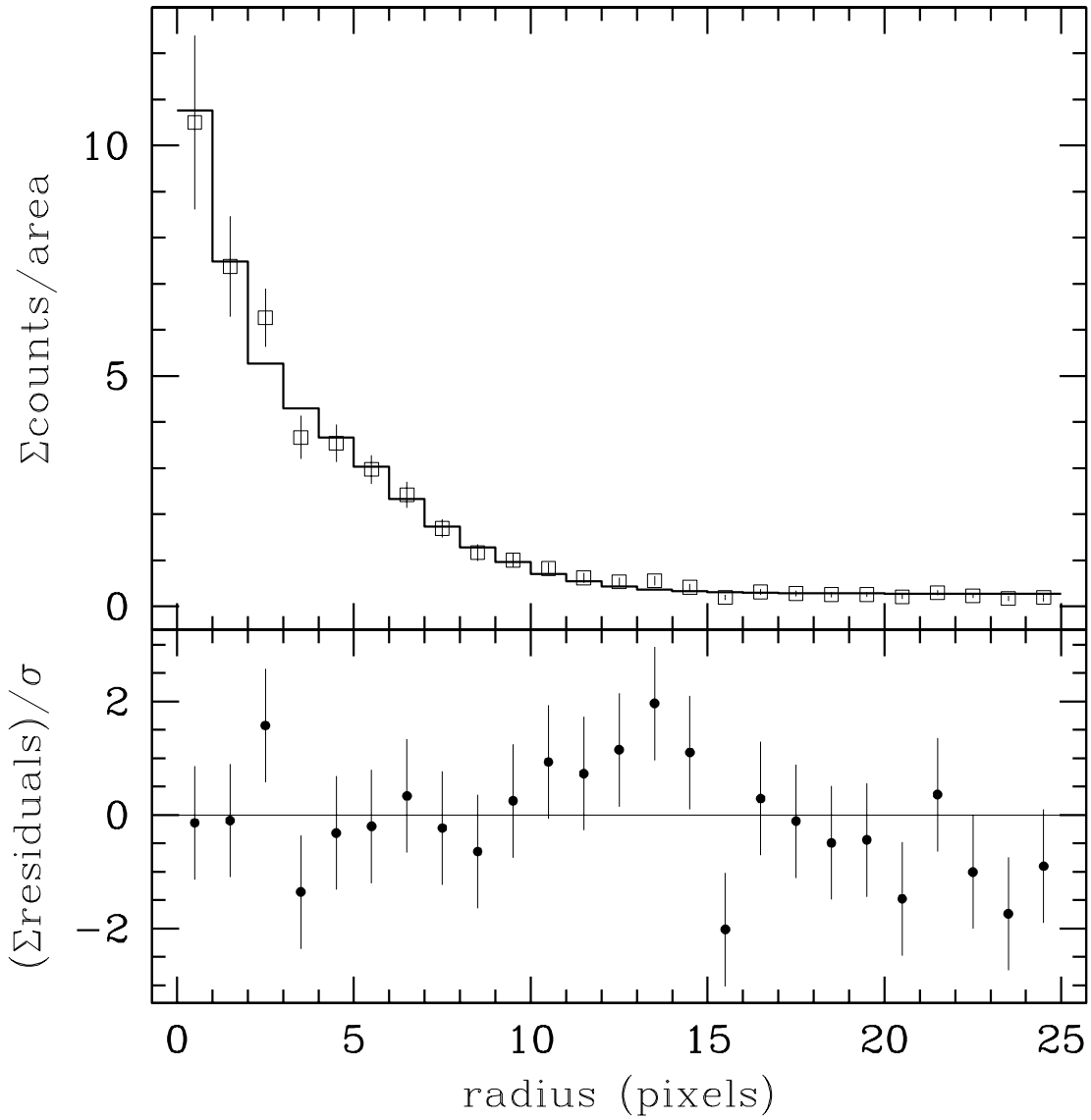

Figure 5.8 *Chandra* emission profile of the compact source region. The curve representing the best fit model composed of a *Chandra* PSF and a more extended Gaussian component. The profile is centered at the coordinates 15h54m24.5s, -55°03′45.1″ (J2000), and each pixel corresponds to a spatial size of 0.″5.

5.6.3 Prong and Bubble Structures

The most unusual feature in the *Chandra* and *XMM* images are two prong-like structures that extend into a faint bubble, approximately 3 arcminutes in diameter (Figures 5.2 and 5.3). The prongs are approximately 1.5 arcminutes in length and their axes are not aligned with the position of the compact source, which is presumably the pulsar. It seems unlikely that the prongs and bubble structures are from the SNR itself and that their position only coincidentally falls along the line of sight to the position of the pulsar and is aligned along the direction of the pulsar motion. The structures may arise from the violent interaction between the reverse shock and the PWN that would cause the pulsar wind material to mix in with the SNR ejecta.

5.6.4 Size of the PWN and Pulsar Wind Cavity

In this section, we estimate the expected sizes of the PWN and the pulsar wind cavity for two scenarios and compare them to the observations; the case where the PWN has reformed and is now expanding subsonically, and the case where the PWN has been deformed into a bow shock, due to the pulsar motion. In Section 5.5 we found that the timescale for the reverse shock to interact with the entire PWN surface of G327.1-1.1 is on the same order as the remnant age. We note that the uncertainty on these estimates is high and that it is possible that the PWN has entered the subsonic stage of expansion. Here we assume that the PWN is expanding subsonically, and has reached a pressure equilibrium with the SNR, after the passage of the reverse shock, in order to make rough estimates of the relative sizes of the SNR radius, (R_{SNR}), the PWN radius (R_{PWN}), and the termination shock radius (R_{ts}). Following van der Swaluw et al. (2001) and setting $P_{\rm pwn}$ equal to $P_{\rm snr}$, the radius of the PWN can be expressed as

$$R_{PWN} \simeq \left(\frac{\dot{E}t}{E_0}\right)^{1/3} R_{SNR}, \tag{5.9}$$

where $\dot{E}$ is the mechanical luminosity driving the pulsar wind, found in Section 5.5, and t is the time passed since the passage of the reverse shock (t_{SNR} minus t_{col}). In Section 5.6, we calculated that t_{SNR} and t_{col} are on the same order of magnitude, but the values are associated with very large uncertainties. For the purpose of our calculation, we set t equal to 5000 yr. Setting the pressure of the relativistic wind terminated at a radius $R_{\rm ts}$ (Kennel & Coroniti 1984) equal to the SNR pressure, we obtain the following expression for $R_{\rm ts}$

$$R_{ts} \simeq \sqrt{\frac{\dot{E}}{cE}} R_{snr}^{3/2}. \tag{5.10}$$

Using the parameters for G327.1-1.1, and our estimate of $\dot{E}$ from Section 5.5, we estimate that $R_{PWN} \simeq 2.7 pc t_{1000}^{1/3}$yr, or $\sim 60'' t_{1000}^{-1/3}$yr. Since the average extent of the X-ray emission observed by *Chandra* is on the order of $60''$(see Figure 5.9), the time since the reverse shock collided with the PWN should be $\sim 1000\,$yr. The prongs and bubble structures ahead of the pulsar may be caused by the turbulent interaction between the reverse shock and the PWN, and may provide further evidence for a somewhat recent reverse shock collision. We calculate a termination shock radius of 0.25 pc, or $6''$, roughly the same size as the extent of the compact source seen in the *Chandra* image (indicated by the innermost contour of Figure 5.9). Even though the estimated values are only first order estimates, the predicted size of R_{ts} indicates that the pulsar wind cavity is too small to be associated with the observed cometary structure. In this scenario, the cometary morphology may be caused by the passage of the reverse shock, which disrupted the reformed PWN from the NW direction.

As an alternative, we consider the case in which the PWN has been deformed into a bow shock and make similar estimates to compare with our observations. We assume a pulsar velocity of 770 km s^{-1}, the minimum required velocity for bow shock formation, found in Section 5.6.1. Following the discussion by van der Swaluw et al. (2003), we

calculate the values of the pressure behind the SNR blast wave, P_{sh}, pulsar mach number, M_{psr}, bow shock pressure, P_{bs}, leading to the the radius of the forward termination shock, R_{ts}^{F} (equations 6, 10, 16, and 21 of van der Swaluw et al. (2003)). Using the parameters for G327.1-1.1 and γ of 5/3, we calculate that $P_{sh} = 5.2 \times 10^{-10}$dyne cm^{-2}, $M_{psr} = 2.8$, $P_{bs} = 4.7 \times 10^{-9}$dyne cm^{-2}, and finally $R_{ts}^{F} = 0.033$ pc, or $0\farcs8$, based on a distance of 9.0 kpc. The radius of the backward termination shock would then be on the order of $2\farcs7$, making the entire extent of the termination shock $\sim 3\farcs5$ (Bucciantini 2002; van der Swaluw et al. 2003). This is somewhat smaller, but on the same order of magnitude as the size of the compact source in G327.1-1.1. The expected size of the contact discontinuity radius is $\approx 1.33 R_{ts}^{F} = 0.04$ pc, or $1''$ (Bucciantini 2002; van der Swaluw et al. 2003; Gaensler et al. 2004). Based on these estimates, the cometary structure in the *Chandra* image appears too large to be attributed to the contact discontinuity, since it extends at least $8''$ beyond the extent of the compact source in the forward direction (see Figure 5.9). The relative sizes of the observed structures are not consistent with estimated sizes from bow shock simulations, but due to the large uncertainties in the derived parameters for G327.1-1.1, we cannot rule out the bow shock scenario on this basis alone. However, we note that the observed X-ray emission ahead of the pulsar in the form of prongs and bubble structures, does suggest that the cometary structure that we are observing is most likely not a bow shock.

5.7 Possible Physical Scenario

There are two possible scenarios that may give rise to the cometary morphology observed in G327.1-1.1; the newly forming PWN may be deformed into a bow shock when the pulsar velocity becomes supersonic, or an asymmetric passage of the reverse shock may disrupt the PWN from one side and give rise to the cometary morphology. While we were not able to rule out either scenario, the latter appears to be a more likely based on the observed X-ray emission ahead of the pulsar (see Section 5.6.4).

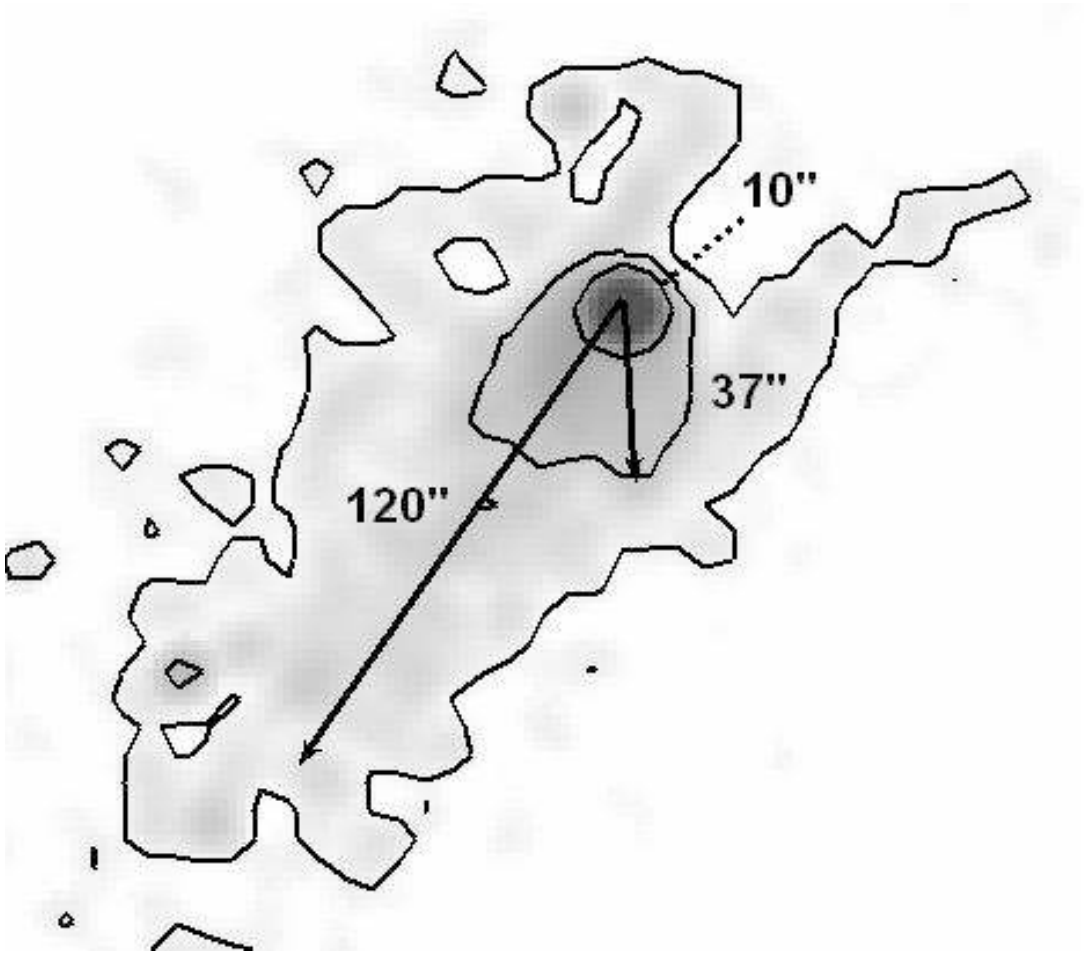

Figure 5.9 The contours and spatial scales for the three main emission regions in the *Chandra* image; the compact source region inside the innermost contour, cometary structure inside the middle contour, and the extended X-ray emission inside the outermost contour.

We suggest that PWN in G327.1-1.1 is in the subsonic stage of expansion, after the passage of the reverse shock. Figure 5.10 illustrates a possible physical scenario that could explain the observed morphology. If we assume that the pulsar was born in the geometric center of the radio shell, indicated by a white dashed circle, its current position suggests that the velocity vector is in the north direction, as indicated by the green arrow. Before the passage of the reverse shock, the PWN was expanding supersonically and was being carried along with the moving pulsar to the north. The position of the PWN immediately before the passage of the reverse shock would therefore be north of the remnant center, as shown by the green circle in Figure 5.10. If inhomogeneities in the ISM caused the reverse shock to reach the PWN from the NW direction first, it would displace the PWN to the location of the radio relic and cause the newly forming PWN to take on the observed cometary morphology (van der Swaluw et al. 2004). Hydrodynamic simulations of van der Swaluw et al. (2004) show the various stages of this process (see Figure 4.3), with the main difference being that an additional asymmetry, besides the pulsar's velocity vector, is required to explain the morphology. In order for the reverse shock to first reach the PWN surface from the northwest direction, a higher ISM density in the West would be required, which cannot be confirmed or ruled out by our data.

5.8 Conclusions

In this paper, we analyzed the *Chandra* and *XMM* imaging and spectroscopy of G327.1-1.1 in order to characterize the nature of the X-ray emission, determine the properties of the SNR and the pulsar progenitor, and understand the evolutionary and physical scenario that would lead to the observed morphology. The X-ray images show an extended compact source that is embedded in a cometary structure, from which a trail of emission extends towards the bright radio PWN. Prong-like structures originate near the compact source and extend into a faint bubble, 3′in diameter. A symmetric shell

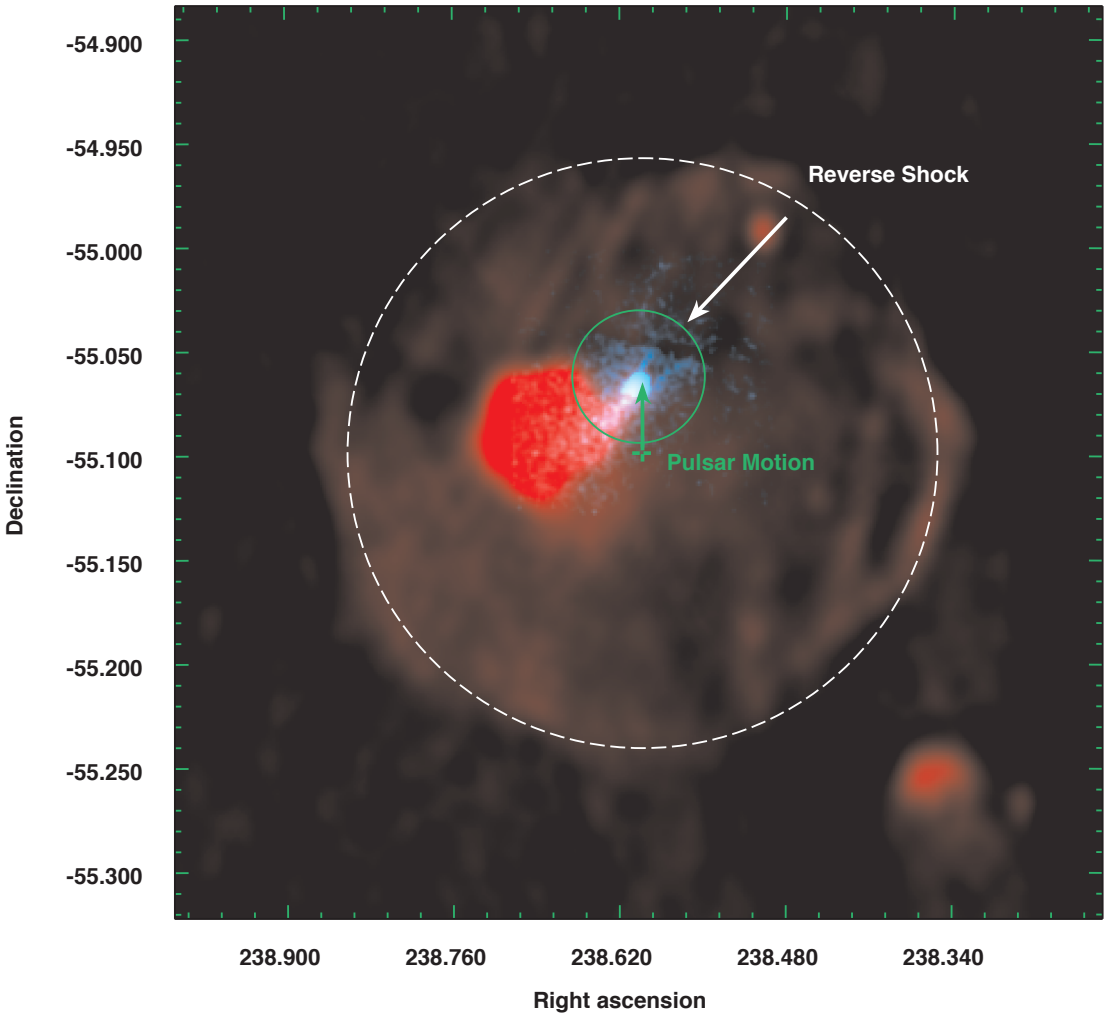

Figure 5.10 The MOST radio image is show in red and *Chandra* ACIS X-ray image in blue/green. The figure illustrates a possible physical scenario that could give rise to the observed radio and X-ray morphology. The white dashed circle is the boundary of the radio shell, the green cross is the geometric center of the shell, the green arrow represents a possible direction of the pulsar motion, the green circle is the position of the PWN immediately before the passage of the reverse shock, and the white arrow indicates the proposed direction of the reverse shock.

coincident with the shell observed in the radio is evident in the 1-2 keV *XMM* image. The X-ray spectrum of the PWN is described by a power-law model with an average photon index of 2.11 $\pm$ 0.03. The shell emission is best described by thermal model with a temperature of 0.30 $\pm$ 0.01 keV. Using the Sedov model and assuming a distance of 9 kpc, we calculate a remnant radius of 22 pc, an age of 18000 years, shock velocity of 500 $\mathrm{km\,s^{-1}}$, $\mathrm{n_0}$ of 0.12 $\mathrm{cm^{-3}}$, a swept-up mass of 31 $M_{\odot}$, and an explosion energy of 0.5×10^{51} ergs. Since the remnant has most likely expanded into a nonuniform medium, the derived dynamical properties are expected to vary.

Based on the timescale for reverse shock interaction and the derived remnant age, it is possible that G327.1-1.1 is in the subsonic expansion stage of its evolution. While we can not discount the possibility of a bow shock formation in G327.1-1.1 based on the calculations of the relative sizes of the PWN and the termination shock radii, the observed X-ray emission ahead of the pulsar makes the bow shock scenario less likely. The cometary morphology may be explained by the passage of the reverse shock from the northwest direction that disrupted the newly forming PWN, which was originally located north of the SNR center.

Chapter 6

Summary of Conclusions and Future Work

This thesis presents multi-wavelength studies of PWNe and composite SNRs with the goal of better understanding their evolutionary development and the impact that they have on their surroundings. When a massive star ($< 8\,M_{\odot}$) collapses and undergoes a SN explosion, it leaves behind a remnant that can be classified as a shell-type SNR, a PWN, or a composite remnant. Shell-type SNRs are composed of an expanding SN blast wave that sweeps the surrounding ISM, and they typically have a symmetric shell morphology. PWNe result from SNe that leave behind a central pulsar that generates a wind of energetic particles that are accelerated in the magnetic field and are producing synchrotron radiation. For these remnants, the rest of the SNR is most likely still undetected, possibly because the SN exploded in a low density medium and the blast wave has not interacted with enough material to produce a detectable shell. Remnants that contain a PWN in addition to an expanding shell are called composite SNRs, and the study of their evolution and morphology can reveal information about the SNR properties that may otherwise be unobservable.

The evolution of PWNe and composite remnants can be divided into several stages;

supersonic PWN expansion into freely expanding ejecta, reverse shock interaction stage, and subsonic expansion into heated ejecta. Initially, the PWN is bounded by a shock driven into the freely expanding SN ejecta. The observational signatures of such an interaction include the detection of thermal emission from heated ejecta in X-rays, line emission in the IR that can be compared to shock models and used to derive shock velocities, spectral line broadening from rapidly moving ejecta, and signatures of processing and destruction of dust in the inner SNR region. When the reverse shock reaches the PWN and crushes the nebula, we expect to observe a disrupted PWN morphology and thermal emission from SN ejecta that has been mixed-in with the PWN material. In the case where the PWN is located off-center due to the pulsar's motion, or when the inhomogeneities in the surrounding ISM density cause the reverse shock to reach the PWN asymmetrically, the reverse shock sweeps the PWN to one side and leaves behind a relic PWN. A new nebula forms around the pulsar and is expected to have a harder spectrum than the relic PWN. If the pulsar's velocity with respect to the surrounding heated ejecta becomes supersonic, the new PWN deforms into a bow shock that appears as a cometary structure. These spectral and morphological signatures can be used to determine the evolutionary stage of the remnant and help develop a more complete understanding of evolutionary process that take place.

This thesis focused on a multi-wavelength study of three different systems that contain PWNe in different stages of their evolution. Each system exhibits unique properties that allowed us to learn about their evolution in greater detail. This chapter summarizes the results for each object, the outstanding questions, and the ongoing and future work that may improve our understanding of the evolution of PWNe and SNRs.

6.1 The Crab Nebula

The Crab Nebula was formed by a SN explosion in 1054 AD. It contains a central pulsar that powers the surrounding PWN that emits synchrotron radiation from the radio to gamma ray wavelengths. The PWN is in the early stage of its evolution, sweeping up the freely-expanding SN ejecta that is observed in the form of filaments of ionized gas that produce emission line spectra. The filaments are photoionized by the high-energy synchrotron emission and they contain traces of dust, seen as absorption features against the nebular background. The Crab Nebula has been extensively studied across the electromagnetic spectrum, but prior to the *Spitzer* Space Telescope, there have been no high resolution IR images at wavelengths longer than 5 μm. The study presented in this thesis is based on the highest quality IR observations available to date. It allowed us to estimate the dust content in the Crab and obtain spatial information about the synchrotron emission in the IR that can be used in combination with the spatial information at other wavelengths to derive a rough, general broadband shape of the Crab's synchrotron spectrum (Temim et al. 2006).

Variations in the slope of the synchrotron spectrum as a function of both frequency and spatial position in the remnant, can be used to derive a general shape of the spectrum over a large frequency range (Katz-Stone et al. 1993). We used the synchrotron dominated 3.6 and 4.5 μm images of the Crab Nebula to create a map of the spectral index. The map shows that there are spatial variations in the index ranging from values of 0.3 to 0.8 across the nebula. Combining this information with optical and X-ray synchrotron images, we derived a broadband spectrum that shows evidence of multiple components along the line of sight. The multiple components are most likely due to the flatter torus and jet and the diffuse emission that steepens with distance. The broadband spectrum also shows evidence for an offset in the spectrum somewhere between the optical and X-ray. This may be an indication of a bump that is expected

from the pileup of relativistic electrons due to energy losses at higher energies.

The evidence for dust in the Crab Nebula was found in the form of optical extinction in the filaments and an infrared excess in the far-IR spectrum (Hester et al. 1990; Fesen & Blair 1990; Green et al. 2004). However, the dust masses estimated in previous IR studies are orders of magnitude smaller than expected, and they indicate that there is a lack of dust in the Crab Nebula. We analyzed *Spitzer* infrared imaging and spectroscopy of the Crab Nebula obtained with the Infrared Array Camera (IRAC) at 3.6, 4.5, 5.8, and 8.0 μm, the Multiband Imaging Photometer (MIPS) at 24 and 70 μm, and three modules of the Infrared Spectrograph (IRS) covering the wavelengths between 5 and 38 μm. The sensitivity of *Spitzer* Space Telescope instruments allowed us to search for dust and forbidden line emission and study the spatial variations of the synchrotron emission across the remnant. The IR spectra of the Crab Nebula show strong forbidden line emission of [Ne II], [Ne III], [O IV], [Fe II], [S III], and [Si II]. We found no evidence for silicate emission, but we observe an infrared excess above the synchrotron continuum at MIPS wavelengths, from which we derived a temperature of ~ 74 K and a dust mass that is on the order of 0.01 $M_{\odot}$. This is still more than an order of magnitude smaller than what theories predict, and the warmer, smaller dust grains appear to be missing entirely.

6.1.1 Future Work

An important question that remains to be answered is where the dust in the Crab Nebula is located and how it is distributed throughout the filaments. Information about the spatial distribution of dust in the Crab has only been obtained through observations of absorption features against the nebular background. The excess of IR emission from dust has been measured from the integrated photometry of the Crab, but there is no spectral or spatial information on IR dust emission. When compared to the [Fe II] 1.644 μm image, the filaments running east to west across the remnant appear much

brighter in the MIPS 24 μm image than the filaments in the north and south. This may be either due to stronger [O IV] 25.89 μm in these filaments or substantially more warm dust. Since our *Spitzer* spectra were obtained from the Crab torus, we were not able to determine the precise contribution of the synchrotron and line emission to the dense filaments in the IR. In order to investigate the distribution and properties of dust in the Crab, IR spectroscopy of the filaments is required. *Spitzer* IRS spectroscopy of five additional positions in the Crab Nebula is available under the Roellig Guaranteed Time Observing Program (Program ID 24), and has yet to be fully analyzed. The new spectroscopy samples different regions of the Crab Nebula that include bright filament cores, synchrotron bays, and outer regions of the remnant. The analysis of the new data will help determine how the infrared spectrum varies spatially across the remnant and whether the enhanced brightness of the filaments in the MIPS images is dominated by line emission or dust. Since the contribution from synchrotron emission is less in some of these regions, it may even be possible to extract spectra of the dust component that can provide information about the composition of dust grains and constrain the dust mass and temperature estimates. Characterizing the properties of dust in the Crab is important in constraining the general properties of dust that condenses directly from SN ejecta.

6.2 Pulsar wind nebula G54.1+0.3 and its IR Shell

G54.1+0.3 is a young PWN closely resembling the Crab for which no thermal emission has been detected in X-rays. As in the Crab Nebula, the larger SNR is presumed to be undetectable because it is expanding into a low density cavity and has not interacted with enough ISM material. The PWN is likely still expanding into the cold SN ejecta that is in free-expansion. However, there have been no previous detections of the thermal emission that would confirm this interaction and the evolutionary stage of the system. In the study described in Chapter 3, we present the first evidence that the

PWN in G54.1+0.3 is interacting with the freely expanding SN ejecta. The *Spitzer* IR images revealed a shell of emission in which a dozen point sources are embedded, along with a more extended clump of emission in the SW, that appears to be aligned with the pulsar's X-ray jet (see Fig. 3.4). A number emission lines are present in the IR spectrum, including [ArII], [NeII], [ClII], [SIII], [FeII], and [SiII], and several of these lines are broadened to velocities of $\sim 1000\,\mathrm{km\,s^{-1}}$, proving the first direct evidence of the expanding SN ejecta swept-up by the PWN. Based on the observed line intensity ratios, the shock velocity is on the order of $\sim 100\,\mathrm{km\,s^{-1}}$.

The spectra also reveal an unidentified dust feature at 21 μm that dominates the emission in the MIPS 24 μm image. It is present in the diffuse shell emission and significantly enhanced at the position of the bright IR clump. The spectrum of G54.1+0.3 is remarkably similar to the spectrum of Cas A Rho et al. (2008), and it is most likely produced by the same dust species. Based on our study of the *Chandra* X-ray and *Spitzer* IR observations of this system, we conclude that the IR emission from the shell mostly originates from the SN ejecta. The line emission is mostly produced in the shocked SN ejecta, while the continuum emission from dust originates from the freshly formed SN dust that is being illuminated by the members of the young stellar cluster in which the SN exploded. The point sources in the IR shell are attributed to radiatively heated dust that is blowing by these stars. Dust models shows that such a scenario can reproduce the observed IR emission from the shell and the embedded point sources, and that approximately $0.1\,\mathrm{M_\odot}$ of dust heated by a dozen young stars is required. The unique environment of G54.1+0.3 and the presence of the stars allowed us to detect and characterize the SN dust that would otherwise be unobservable. The study of unshocked dust may prove to be most effective in systems in which the SN explodes inside a stellar cluster.

6.2.1 Future Work

In Chapter 3, we proposed that the IR point sources embedded in the shell of G54.1+0.3 are early-type stars belonging to a cluster in which the SN exploded. The freshly formed SN dust is being illuminated as it blows past the stellar sources, giving rise to the observed IR emission. In this scenario, the IR shell and the observed emission lines all arise from SN ejecta. This result has important implications since it implies that we are actually probing freshly formed SN dust that has not yet been processed by the reverse shock. In order to confirm this scenario, optical and IR spectroscopy of the embedded point sources is required. A more detailed spectroscopic study of the stellar sources would help verify their spectral types and develop a better understanding of the radiation field in the proposed stellar cluster, allowing for improved modeling of the radiative heating of dust in the shell and better constraints on the dust mass.

More detailed modeling of the IR spectrum of the shell in G54.1+0.3 will provide important constraints on the grain properties and quantity of dust that condenses out of SN ejecta. The spectrum of the dust in G54.1+0.3 exhibits very similar features as the spectrum of the dust in Cas A, and the dust appears to be freshly formed SN dust in both cases. Modeling of the spectral shape with different grain compositions and temperatures is crucial in understanding the dust properties. While attempts to model the dust emission in Cas A provided some estimates of the mass and composition (Rho et al. 2008), the fits to the dominant emission features at 21 and 13 μm have not been satisfactory. Determining the relative ratios of various grain compositions that condense in SN ejecta will significantly improve the available models for dust condensation in SNe (Kozasa et al. 2009).

6.3 Composite Supernova Remnant G327.1-1.1

G327.1-1.1 is a composite supernova remnant that has an unusual morphology consisting of a symmetric radio shell and an off center non-thermal component that indicates the presence of a PWN (Figure 5.1). A narrow ridge of emission extends from the PWN structure toward the northwest. G327.1-1.1 is an ideal object for the study of several aspects of the late stages of PWN evolution. It appears to be comprised of a moving pulsar, an asymmetric reverse shock, a relic PWN swept aside by the reverse shock, and a newly forming PWN that has possibly been deformed into a bow-shock nebula. In addition to these structures, there are additional features whose presence in unexpected. Diffuse emission in the form of prong-like features and a large bubble is not expected ahead of a bow-shock. The various structures in the cometary region itself are not entirely consistent with bow-shock models, and may suggest that we are actually observing a transition phase in which the PWN transforms into a bow-shock.

Previous X-ray studies of G327.1-1.1 have revealed elongated extended emission and a compact source at the tip of the radio ridge that may be coincident with the actual pulsar. There has also been evidence for thermal emission in G327.1-1.1, but the properties of this component are not well determined from previous X-ray data. In the study presented in Chapter 5, we analyzed *Chandra* ACIS 50 ks observations and *XMM-Newton* 100 ks observations of G327.1-1.1. The high resolution *Chandra* observations provide new insight into the structure of the inner region of the remnant, while the sensitivity of the *XMM* data allowed us to image the thermal X-ray shell for the first time and to characterize its properties.

The *Chandra* image (Figure 5.2) of G327.1-1.1 shows a compact source embedded in a cometary structure, from which a trail of X-ray emission extends in the southeast direction, along the radio ridge. A bright prong-like structure appears to originate from the vicinity of the compact source and extend out to the northwest. The most unusual feature in the X-ray images is the bubble-like structure, 3 arcminutes in diameter, that

extends out from the prongs. The compact core itself is similar to compact nebulae observed around many other young neutron stars, and typically associated with inner jet and torus structures. Indeed, simple spatial modeling in which the best fit Gaussian components are removed from the core reveals an asymmetric jet-like structure, $4''$ in length.

The XMM images show emission from the entire radio shell (Figure 5.4). As in the radio image, the plerionic component in X-rays is displaced from the geometric center of the X-ray shell. In order to determine the general spectral properties of the X-ray emission in G327.1-1.1, spectra were extracted from two different regions in the XMM data, the inner PWN region and the outer shell. The PWN emission is well characterized by a power-law model with a photon index of 2.0, while the emission from the shell region can be described by a thermal model with a temperature of approximately 0.3 keV. We used this newly determined temperature to calculate the remnant properties based on the Sedov blast wave model. Assuming a distance of 9 kpc, we calculate a remnant radius of 22 pc, an age of 18000 yr, shock velocity of 500 $\mathrm{km\,s^{-1}}$, n_o of 0.12 $\mathrm{cm^{-3}}$, a swept-up mass of 31 $M_\odot$, and an explosion energy 0.5×10^{51} ergs.

In order to determine how the spectrum of the PWN varies with distance from the compact source, spectra were also extracted from the *Chandra* ACIS data using apertures at various distances from the compact source. Each of the spectra were fit with an absorbed power law plus a thermal plasma model and they show steepening with distance from the compact source, which is consistent with the synchrotron burn-off of high energy electrons injected by a pulsar. The peculiar morphology of G327.1-1.1 may be explained by the emission from a rapidly moving pulsar and a relic PWN that has been disrupted by the reverse shock. A possible scenario is a pulsar moving in the direction opposite of the X-ray trail with the reverse shock disrupting the PWN from the southwest (see Fig. 5.10).

6.3.1 Future Work

The X-ray study of G327.1-1.1 helped characterize the properties and the evolutionary stage of this composite SNR, and it helped shed light on the origin of its complex morphology. The study also led to the discovery of faint structures that may hold the key to understanding the precise geometry of this system and the particular phase of PWN evolution that marks a transitional stage between a static PWN and a bow shock nebula. The morphology of the cometary structure is suggestive of a bow shock nebula, but the the prong, bubble, and jet-like structures do not appear to be consistent with this scenario. Emission beyond the confines of a bow shock is not expected to be present, and the formation of jet and torus structures should not occur in the case of a bow shock. It may be possible that the observed cometary morphology is instead caused by the passage of an asymmetric reverse shock that swept-up the PWN in one direction, giving it a cometary morphology, but even in this case it is difficult to explain all the observed structures and size scale of the PWN.

Deeper high-resolution X-ray observations of G327.1-1.1 are required to investigate the observed structures in G327.1-1.1 and uncover their nature. Their characterization may provide additional constraints for models describing the evolution of composite remnants, particularly in the late phase of evolution when the PWN is reforming after being disrupted by the reverse shock. Deeper imaging of the prong and bubble features would help establish how they are connected to the cometary structure and the rest of the PWN, giving clues about their formation. It is unclear whether these structures are connected to the cometary feature itself, or if they were formed as a result of the passage of the reverse shock. The orientation of these features is aligned with the long axis of the cometary structure and the X-ray tail, but the reason for this alignment still remains unknown. Spectroscopy and improved imaging will help shed light on these outstanding questions.

High-resolution imaging of the extended core region in G327.1-1.1 will help resolve

its structure and determine whether the morphology is consistent with a torus and jet. The detection of such structures will help distinguish whether the cometary structure is caused by the passage of an asymmetric reverse shock, or if it is a bow shock nebula. Deeper imaging will also allow for better constraints on the properties of the thermal shell in G327.1-1.1 and a search for SN ejecta mixed in with the disrupted PWN, as would be expected after a reverse shock interaction. These additional clues will help us confirm the current evolutionary stage of G327.1-1.1 and construct its evolutionary history.

6.4 Dust Properties in SNRs

The questions of what types and quantities of dust are formed in SNe explosions and injected into the ISM are still not very well understood. Only in recent years have the higher resolution IR observations with *Spitzer* allowed for direct detections of dust emission from freshly formed grains in SNRs. IRS spectral maps enabled comparisons between the spatial distribution of dust emission and SN ejecta that confirmed that the dust is indeed SN formed dust, as opposed to the swept-up ISM or circumstellar dust. IR spectroscopy of the dust that condensed out of SN ejecta is available for several SNRs, including G54.1+0.3 (see Chapter 3) and Cas A (Rho et al. 2008). While some work has been done to characterize the shape of the IR spectra and determine the grain properties (e.g. Rho et al. 2008; Kozasa et al. 2009), dominant emission features are still not well described by these models. More detailed modeling of the observed dust emission is required to determine the composition and quantity of freshly formed dust in SNRs. The estimate of dust masses in SNRs, in the range of $0.01 - 0.05\,M_{\odot}$ (e.g. Rho et al. 2009), are still well below the masses predicted by models describing dust production and survival in SNe (Kozasa et al. 2009). It is possible that a large fraction of the dust in SNRs is cold, and therefore does not contribute enough to the *Spitzer* wavebands to be detected. The current estimates are mostly probing warm dust that has

either been collisionally heated by the reverse shock, or heated by synchrotron emission (e.g. Chapter 2) or a stellar radiation field (e.g. Chapter 3). In order to estimate the total mass of dust present in an SNR, longer wavelength observations with Herschel, SCUBA-2, and ALMA will prove to be crucial. The high resolution (down to 0.005″) sub-millimeter observations with ALMA will help map the cold dust distribution in SNRs and significantly improve the total mass estimates. The observations of PWNe that are presumably evolving in SNRs that are expanding in a low density medium, such as the Crab and G54.1+0.3, may prove to be ideal for the study of the cold dust distribution since the dust that surrounds these nebulae has not yet been destroyed and processed by the reverse shock, nor mixed with the ISM material.

6.5 IR Spectroscopy of Kes 75: Constraining the Dust-to-Gas Mass Ratio

The composite SNR Kes 75, recently detected with *Spitzer*, is an excellent candidate for the study of the dust content and processing in composite SNRs. Kes 75 is a Galactic SNR consisting of a PWN and a partial thermal shell. The PWN is powered by a 0.3 s pulsar (PSR J1846-0258) that has a characteristic age of 723 yr, one of the youngest known (Gotthelf et al. 2000). An upper limit on its true age of 884 yr was derived from the measurement of the braking index, $n = 2.65 \pm 0.01$ (Livingstone et al. 2006). The spin-down rate $\dot{P} = 7.1 \times 10^{-12}\,\mathrm{s\,s^{-1}}$ leads to a spin-down luminosity of $\dot{E} = 8.1 \times 10^{36}\,\mathrm{ergs\,s^{-1}}$ and a strong surface magnetic field $B = 5 \times 10^{13}$ G (Gotthelf et al. 2000). The distance to Kes 75 is poorly constrained, with the estimates ranging from 5.1 to 21 kpc (Caswell et al. 1975; Milne 1979; Becker & Helfand 1984; Leahy & Tian 2008). Recent millimeter observations of CO line emission towards Kes 75 provide evidence for an association with an adjacent molecular cloud at a distance of $\sim 10.6\,\mathrm{pc}$ (Su et al. 2009).

Radio observations of Kes 75 show a partial SNR shell , $\sim 1.5'$ in radius, with a spectral index $\alpha = 0.7$, and a flatter PWN component with $\alpha = 0.25$ (Becker & Kundu 1976; Helfand et al. 2003). X-ray observations with *ASCA* and *Chandra* also showed the composite nature of the remnant with a morphology closely resembling the radio (Blanton & Helfand 1996; Helfand et al. 2003). *Chandra* spectroscopy of the PWN shows that the emission softens with distance from the pulsar, with the photon index Γ ranging from 1.1 to 1.9, and a thermal component arising in the outer regions (Morton et al. 2007; Ng et al. 2008). The shell emission in Kes 75 is primarily concentrated in two regions in the southeast (SE) and the southwest (SW). Morton et al. (2007) show that the spectra of the shell can be characterized by a two-component thermal model with temperatures of 0.25 keV and 1.38 keV for the SE region and 0.22 keV and 1.50 keV for the SW region. The hydrogen column density, N_H was fixed to 4.0×10^{22} cm^{-2}, as derived from the spectral fitting of the PWN region. The higher temperature thermal components showed an increased abundance of Si, S, and Ar, and was attributed to SN ejecta material heated by the reverse shock, with the lower temperature component arising from the swept-up ISM/CSM material (Morton et al. 2007).

The first IR detection of the Kes 75 with *Spitzer* revealed a partial IR shell coincident with the shell at radio and X-ray wavelengths. Morton et al. (2007) used Chandra and MIPS 24 μm observations, along with IRAC upper limits, to constrain the dust emission models and obtain a dust-to-gas mass ratio $\mathrm{M_{dust}/M_{gas}} \sim 5 \times 10^{-4}$, more than an order of magnitude lower than that of the Galaxy. This dust-to gas ratio is consistent with the values measured for Large Magellanic Cloud (LMC) SNRs that are 5 times lower than the ratios assumed for the LMC, implying that as much as 40 % of dust is destroyed by the SNR shocks (Borkowski et al. 2006; Williams et al. 2006). Since Kes 75 was only detected in the MIPS 24 μm band, the data were not sufficient to characterization the dust composition and place tighter constraints on the temperature and mass. In order to place better constraints on the observed dust emission, we obtained *Spitzer*

IRS long-wavelength (LH and LL) spectra of Kes 75, at both the SE and SW regions of the shell. The spectroscopy allows us to to characterize the shape of the spectrum, determine what fraction of the IR emission arises from lines, gain information about the grain composition, and better constrain the available dust model. Our preliminary results indicate that the IR emission of the shell is dominated by continuum emission from dust with very little contribution from line emission. The spectrum will be used to test the prediction of the dust emission model from Morton et al. (2007) and further constrain the dust-to-gas ratio in Kes 75.

6.6 Hydrodynamic Modeling of Composite SNRs

Numerical models of PWNe and composite SNRs help us understand the physical processes and evolutionary stages that they go through, their morphological properties, and the interactions between the system's various components. Even more importantly, simulations of these systems produce results and predictions that we can compare with observations at multiple wavelengths and use to constrain the physical properties of the system, determine their current evolutionary phase, and construct their evolutionary history. In turn, the information obtained from multi-wavelength observations of SNRs leads to more sophisticated numerical modeling that better describes the available data. Hydrodynamic models for the evolution of composite remnants, in which the PWN initially expands into the inner SN ejecta and is subsequently crushed by the reverse shock, have been implemented by several authors, including van der Swaluw et al. (1998); Blondin et al. (2001); Bucciantini et al. (2003). All models in which the pulsar and the PWN remain centered in the SNR show that the timescale for the reverse shock interaction stage is comparable to the timescale for the supersonic expansion stage of the PWN evolution. This suggests that many composite SNRs should be observed in this transitional stage of evolution whose signatures include a small PWN to SNR radius ratio, and brightened emission and a low frequency cooling break due to increased

magnetic field strength (van der Swaluw 2005, and references therein). As discussed in Chapter 4, when the pulsar has a high velocity and becomes displaced from the center of the SNR, the reverse shock will disrupted the PWN asymmetrically and sweep it to the opposite side, producing a relic PWN. The system then consists of a relic nebula that is typically bright in the radio, and a newly forming PWN that surrounds the moving pulsar. An example of such a system is G327.1-1.1, discussed in detail in Chapter 5. When the pulsar's velocity becomes supersonic with respect to the surrounding SNR, the PWN deforms into a bow shock and takes on a cometary morphology. A similar morphology can result in a case where the pulsar is static, but the inhomogeneities in the ISM density cause the reverse shock to reach the PWN asymmetrically. Two-dimensional hydrodynamic modeling of these scenarios have been carried out by van der Swaluw et al. (2004) for the case of the moving pulsar, and by Blondin et al. (2001) for a zero velocity pulsar and inhomogeneous ISM density. The models produce the two-component morphology consisting of the relic nebula and the newly forming PWN, and both result in a disrupted PWN that mixes with the surrounding material and has a complex morphology. While the current 2-dimensional models provide important predictions that can be compared with observations of composite remnants, the morphology of the actual systems likely depends on both the pulsar's motion and the density structure of the surrounding ISM. As in the case of G327.1-1.1 (see Chapter 5), it can be difficult to distinguish between the two cases and determine how much each of the factors affects the morphology of the SNR. In order to investigate the effects of the pulsar's motion and inhomogeneities in the ambient density, three-dimensional hydrodynamic simulations of composite SNRs are required. Expanding the existing models into three dimensions is the key to understanding the complex morphology of composite SNRs.

References

Allen, C. W. 1973, London: University of London, Athlone Press, —c1973, 3rd ed.,

Arendt, R. G., Dwek, E., & Moseley, S. H. 1999, ApJ, 521, 234

Arendt, R. G. 1989, ApJS, 70, 181

Arendt, R. G., Dwek, E., & Moseley, S. H. 1999, ApJ, 521, 234

Artymowicz, P., & Clampin, M. 1997, ApJ, 490, 863

Aschenbach, B. 2002, Neutron Stars, Pulsars, and Supernova Remnants, 13

Bandiera, R., Amato, E., & Woltjer, L. 1998, Memorie della Societa Astronomica Italiana, 69, 901

Bandiera, R., Neri, R., & Cesaroni, R. 2002, A&A, 386, 1044

Bandiera, R. 2002, Mem. S.A. It., 73, 1

Bandiera, R. 2002, ASP Con. Ser., Vol. 9999

Becker, R. H., & Kundu, M. R. 1976, ApJ, 204, 427

Becker, R. H., & Helfand, D. J. 1984, ApJ, 283, 154

Begelman, M. C., & Li, Z.-Y. 1992, ApJ, 397, 187

Bietenholz, M. F., Frail, D. A., & Hester, J. J. 2001, ApJ, 560, 254

Bietenholz, M. F., Hester, J. J., Frail, D. A., & Bartel, N. 2004, ApJ, 615, 794

Blair, W. P., Davidson, K., Fesen, R. A., Uomoto, A., MacAlpine, G. M., & Henry, R. B. C. 1997, ApJS, 109, 473

Blair, W. P., et al. 2000, ApJ, 537, 667

Blanton, E. L., & Helfand, D. J. 1996, ApJ, 470, 961

Blondin, J. M., Chevalier, R. A., & Frierson, D. M. 2001, ApJ, 563, 806

Blondin, J. M., Wright, E. B., Borkowski, K. J., & Reynolds, S. P. 1998, ApJ, 500, 342

Bochinno, F. & Bandiera, R. 2003, å, 398, 195

Bohren, C. F., & Huffman, D. R. 1983, New York: Wiley, 1983

Borkowski, K. J., Harrington, J. P., Blair, W. P., & Bregman, J. D. 1994, ApJ, 435, 722

Borkowski, K. J., et al. 2006, ApJL, 642, L141

Bucciantini, N. 2002, A&A, 387, 1066

Bucciantini, N., Blondin, J. M., Del Zanna, L., & Amato, E. 2003, A&A, 405, 617

Buccheri, R., et al. 1983, A&A, 128, 245

Burbidge, E. M., Burbidge, G. R., Fowler, W. A., & Hoyle, F. 1957, Reviews of Modern Physics, 29, 547

Camilo, F., Lorimer, D. R., Bhat, N. D. R., Gotthelf, E. V., Halpern, J. P., Wang, Q. D., Lu, F. J., & Mirabal, N. 2002, ApJL, 574, L71

Carey, S. J., et al. 2009, PASP, 121, 76

Carter, J. A., & Read, A. M. 2007, A&A, 464, 1155

Caswell, J. L., Murray, J. D., Roger, R. S., Cole, D. J., & Cooke, D. J. 1975, A&A, 45, 239

Chan, K.-W., & Onaka, T. 2000, ApJL, 533, L33

Chevalier, R. A. 2005, ApJ, 619, 839

Chevalier, R. A., & Gull, T. R. 1975, ApJ, 200, 399

Chevalier, R. A. 1982, ApJ, 258, 790

Chiar, J. E., & Tielens, A. G. G. M. 2006, ApJ, 637, 774

Clayton, D. D. 1982, QJRAS, 23, 174

Clark, D. H., Caswell, J. L., & Green, A. J. 1973, Nature, 246, 28

Clark, D. H., Caswell, J. L., & Green, A. J. 1975, Australian Journal of Physics Astrophysical Supplement, 1

Dasyra, K. M., et al. 2008, ApJL, 674, L9

Davidson, K., & Fesen, R. A. 1985, ARA&A, 23, 119

Davis, J. E. 2001, ApJ, 562, 575

Dorschner, J., Friedemann, C., Guertler, J., & Duley, W. W. 1980, Ap&SS, 68, 159

Douvion, T., Lagage, P. O., Cesarsky, C. J., & Dwek, E. 2001, A&A, 373, 281

Draine, B. T. 1989, Infrared Spectroscopy in Astronomy, 290, 93

Draine, B. T. 2009, arXiv:0903.1658

Dwek, E. 1988, ApJ, 329, 814

Dwek, E. 2004, ApJ, 607, 848

Dwek, E., et al. 2008, ApJ, 676, 1029

Eikenberry, S. S., Fazio, G. G., Ransom, S. M., Middleditch, J., Kristian, J., & Pennypacker, C. R. 1997, ApJ, 477, 465

Elmegreen, B. G., Efremov, Y., Pudritz, R. E., & Zinnecker, H. 2000, Protostars and Planets IV, 179

Emmering, R. T., & Chevalier, R. A. 1987, ApJ, 321, 334

Fazio, G. G., et al. 2004, ApJS, 154, 10

Fesen, R., & Blair, W. P. 1990, ApJL, 351, L45

Fesen, R. A., & Kirshner, R. P. 1982, ApJ, 258, 1

Fesen, R. A., Martin, C. L., & Shull, J. M. 1992, ApJ, 399, 599

Gaensler, B. M., van der Swaluw, E., Camilo, F., Kaspi, V. M., Baganoff, F. K., Yusef-Zadeh, F., & Manchester, R. N. 2004, ApJ, 616, 383

Gaensler, B. M., & Slane, P. O. 2006, ARA&A, 44, 17

Gehrz, R. D. 1988, Nature, 333, 705

Gehrz, R. D., & Ney, E. P. 1987, Proc. Nat. Acad. Sci. (USA), 84, 6961

Gehrz, R. D., & Ney, E. P. 1990, Proc. Nat. Acad. Sci. (USA), 97, 4354

Gehrz, R. D., Truran, J. W., Williams, R. E., & Starrfield, S. 1998, PASP, 110, 3

Gehrz, R. D., et al. 2007, Review of Scientific Instruments, 78, 011302

Gelfand, J. D., Slane, P. O., & Zhang, W. 2009, arXiv:0904.4053

Ghavamian, P., Raymond, J., Smith, R. C., & Hartigan, P. 2001, ApJ, 547, 995

Goldreich, P., & Julian, W. H. 1969, ApJ, 157, 869

Gotthelf, E. V., Vasisht, G., Boylan-Kolchin, M., & Torii, K. 2000, ApJL, 542, L37

Graham, J. R., Wright, G. S., & Longmore, A. J. 1990, ApJ, 352, 172

Grasdalen, G. L. 1979, PASP, 91, 436

Green, D. A., Tuffs, R. J., & Popescu, C. C. 2004, MNRAS, 355, 1315

Green, D. A. 1985, MNRAS, 216, 691

Gull, T. R., & Fesen, R. A. 1982, ApJL, 260, L75

Hamilton, A. J. S., & Sarazin, C. L. 1984, ApJ, 287, 282

Harkness, R. P., & Wheeler, J. C. 1990, Supernovae, 1

Hartigan, P., Raymond, J., & Pierson, R. 2004, ApJL, 614, L69

Hartigan, P., Raymond, J., & Hartmann, L. 1987, ApJ, 316, 323

Helfand, D. J., Collins, B. F., & Gotthelf, E. V. 2003, ApJ, 582, 783

Helfand, D. J., & Becker, R. H. 1987, ApJ, 314, 203

Hester, J. J., Graham, J. R., Beichman, C. A., & Gautier, T. N. 1990, ApJ, 357, 539

Hester, J. J., et al. 1995, ApJ, 448, 240

Hester, J. J., et al. 2002, ApJL, 577, L49

Hester, J. J. 2008, ARA&A, 46, 127

Higdon, S. J. U., et al. 2004, PASP, 116, 975

Hony, S., Waters, L. B. F. M., & Tielens, A. G. G. M. 2001, A&A, 378, L41

Houck, J. R., et al. 2004, ApJS, 154, 18

Hrivnak, B. J., Volk, K., & Kwok, S. 2009, ApJ, 694, 1147

Hrivnak, B. J., Volk, K., Geballe, T. R., & Kwok, S. 2008, IAU Symposium, 251, 213

Hrivnak, B. J., Volk, K., & Kwok, S. 2000, ApJ, 535, 275

Huffman, D. R. 1988, Experiments on Cosmic Dust Analogues, 149, 25

Rudnick, Lawrence, Tracey, DeLaney, Smith, J. D., Rho, Jeonghee, Reach, William T., Kozasa, Takashi, Gomez, Haley, 2009, submitted to ApJ

Jaffe, W. J., & Perola, G. C. 1973, A&A, 26, 423

Jäger, C., Dorschner, J., Mutschke, H., Posch, T., & Henning, T. 2003, A&A, 408, 193

Jones, A. P., Tielens, A. G. G. M., & Hollenbach, D. J. 1996, ApJ, 469, 740

Kaastra, J. S., Paerels, F. B. S., Durret, F., Schindler, S., & Richter, P. 2008, Space Science Reviews, 134, 155

Kardashev, N. S. 1962, Soviet Astronomy, 6, 317

Kaspi, V. M. et al. 2006, Compact stellar X-ray sources, 279

Kennel, C. F., & Coroniti, F. V. 1984, ApJ, 283, 710

Katz-Stone, D. M., Rudnick, L., & Anderson, M. C. 1993, ApJ, 407, 549

Koo, B.-C., et al. 2008, ApJL, 673, L147

Kozasa, T., Nozawa, T., Tominaga, N., Umeda, H., Maeda, K., & Nomoto, K. 2009, arXiv:0903.0217

Kwok, S., Volk, K. M., & Hrivnak, B. J. 1989, ApJL, 345, L51

Lamb, R. C., & Markert, T. H. 1981, ApJ, 244, 94

Laor, A., & Draine, B. T. 1993, ApJ, 402, 441

Leahy, D. A. 1989, A&A, 216, 193

Leahy, D. A., Tian, W., & Wang, Q. D. 2008, AJ, 136, 1477

Leahy, D. A., & Tian, W. W. 2008, A&A, 480, L25

Livingstone, M. A., Kaspi, V. M., Gotthelf, E. V., & Kuiper, L. 2006, ApJ, 647, 1286

Livingstone, M. A., Kaspi, V. M., Gavriil, F. P., Manchester, R. N., Gotthelf, E. V. G., & Kuiper, L. 2007, Ap&SS, 308, 317

Longair, M. S. 1994, High Energy Astrophysics, Vol. 2, 2nd edition, Cambridge University Press 1981, 1994

Lu, F., Wang, Q. D., Gotthelf, E. V., & Qu, J. 2007, ApJ, 663, 315

Lu, F. J., Wang, Q. D., Aschenbach, B., Durouchoux, P., & Song, L. M. 2002, ApJL, 568, L49

Lu, F. J., Aschenbach, B., & Song, L. M. 2001, A&A, 370, 570

Lucke, P. B. 1978, A&A, 64, 367

Lyubarsky, Y. E. 2002, MNRAS, 329, L34

MacAlpine, G. M., McGaugh, S. S., Mazzarella, J. M., & Uomoto, A. 1989, ApJ, 342, 364

Manchester, R. N., & Taylor, J. H. 1977, Pulsars., by Manchester, R. N.; Taylor, J. H.. San Francisco, CA (USA): W. H. Freeman, 281

Marsden, P. L., Gillett, F. C., Jennings, R. E., Emerson, J. P., de Jong, T., & Olnon, F. M. 1984, ApJL, 278, L29

McKee, C. F. 1974, ApJ, 188, 335

Milne, D. K. 1979, Australian Journal of Physics, 32, 83

Morse, J.A., Smith, N., Blair, W.P., Kirshner, R.P., Winkler, P.F., & Hughes, J.P. 2006, ApJ, in press.

Morton, T. D., Slane, P., Borkowski, K. J., Reynolds, S. P., Helfand, D. J., Gaensler, B. M., & Hughes, J. P. 2007, ApJ, 667, 219

Neufeld, D. A., Hollenbach, D. J., Kaufman, M. J., Snell, R. L., Melnick, G. J., Bergin, E. A., & Sonnentrucker, P. 2007, ApJ, 664, 890

Ng, C.-Y., Slane, P. O., Gaensler, B. M., & Hughes, J. P. 2008, ApJ, 686, 508

Nodes, C., Birk, G. T., Gritschneder, M. & Lesch, H. 2004, A&A 423, 13

O'Connor, P., Golden, A., & Shearer, A. 2005, ApJ, 631, 471

Oliva, E., Moorwood, A. F. M., Drapatz, S., Lutz, D., & Sturm, E. 1999, A&A, 343, 943

Pacini, F. & Salvati, M. 1973, ApJ, 186, 249-265

Percival, J. W., et al. 1993, ApJ, 407, 276

Posch, T., Mutschke, H., & Andersen, A. 2004, ApJ, 616, 1167

Possenti, A., Cerutti, R., Colpi, M., & Mereghetti, S. 2002, A&A, 387, 993

Raymond, J. C., & Smith, B. W. 1977, ApJS, 35, 419

Reach, W. T., et al. 2005, PASP, 117, 978

Reach, W. T., & Rho, J. 2000, ApJ, 544, 843

Rees, M. J., & Gunn, J. E. 1974, MNRAS, 167, 1

Reich, W., Fuerst, E., Haslam, C. G. T., Steffen, P., & Reif, K. 1984, A&AS, 58, 197

Reich, W., Fürst, E., & Kothes, R. 1998, Memorie della Societa Astronomica Italiana, 69, 933

Reynolds, S. P., & Chevalier, R. A. 1984, ApJ, 278, 630

Reynolds, S. astro-ph/0308483

Reynolds, S. P. 2008, ARA&A, 46, 89

Rieke, G. H., et al. 2004, ApJS, 154, 25

Rieke, G. H., & Lebofsky, M. J. 1985, ApJ, 288, 618

Rho, J., et al. 2008, ApJ, 673, 271

Rho, J., et al. 2009, arXiv:0901.1699

Ryter, C., Cesarsky, C. J., & Audouze, J. 1975, ApJ, 198, 103

Sankrit, R., et al. 1998, ApJ, 504, 344

Saken, J. M., Fesen, R. A., & Shull, J. M. 1992, ApJS, 81, 715

Scott, A., & Duley, W. W. 1996, ApJS, 105, 401

Sedov, L. I. 1959, Similarity and Dimensional Methods in Mechanics, New York: Academic Press, 1959

Seward, F. D., Gorenstein, P., & Smith, R. K. 2006, ApJ, 636, 873.

Seward, F. D., & Wang, Z.-R. 1988, ApJ, 332, 199

Seward, F. D., Kearns, K. E., & Rhode, K. L. 1996, ApJ, 471, 887

Skrutskie, M. F., et al. 2006, AJ, 131, 1163

Slane, P. et al. 1998, Memorie della Societa Astronomica Italiana, 69, 945

Slane, P. 2005, NATO ASIB Proc. 210: The Electromagnetic Spectrum of Neutron Stars, 15

Slane, P. 2008, Astrophysics of Compact Objects, 968, 143

Slane, P., Helfand, D. J., van der Swaluw, E., & Murray, S. S. 2004, ApJ, 616, 403

Seward, F. D. 1989, AJ, 97, 481

Shaw, R. A., & Dufour, R. J. 1995, PASP, 107, 896

Smith, J. D. T., et al. 2007, PASP, 119, 1133

Smith, J. D. T., Rudnick, L., Delaney, T., Rho, J., Gomez, H., Kozasa, T., Reach, W., & Isensee, K. 2008, arXiv:0810.3014

Smith, N. 2003, MNRAS, 346, 885

Sollerman, J. 2003, A&A, 406, 639

Speck, A. K., & Hofmeister, A. M. 2004, ApJ, 600, 986

Speck, A. K., Thompson, G. D., & Hofmeister, A. M. 2005, ApJ, 634, 426

Su, Y., Chen, Y., Yang, J., Koo, B.-C., Zhou, X., Jeong, I.-G., & Zhang, C.-G. 2009, ApJ, 694, 376

Sugerman, B. E. K., Lawrence, S. S., Crotts, A. P. S., Bouchet, P., & Heathcote, S. R. 2002, ApJ, 572, 209

Sun, M., Wang, Z., & Chen, Y. 1999, ApJ, 511, 274

Swinbank, E. 1980, MNRAS, 193, 451

Temim, T., et al. 2006, AJ, 132, 1610

Temim, T., Slane, P., Gaensler, B. M., Hughes, J. P., & Van Der Swaluw, E. 2009, ApJ, 691, 895

Truelove, J. K., & McKee, C. F. 1999, ApJS, 120, 299

Uomoto, A., & MacAlpine, G. M. 1987, AJ, 93, 1511

Velusamy, T., & Becker, R. H. 1988, AJ, 95, 1162

Veron-Cetty, M. P., & Woltjer, L. 1993, A&A, 270, 370

Van Der Swaluw, E., Achterberg, A., & Gallant, Y. A. 1998, Memorie della Societa Astronomica Italiana, 69, 1017

van der Swaluw, E., Achterberg, A., Gallant, Y. A., & Tóth, G. 2001, A&A, 380, 309

van der Swaluw, E., Achterberg, A., Gallant, Y. A., Downes, T. P., & Keppens, R. 2003, A&A, 397, 913

van der Swaluw, E., Downes, T. P., & Keegan, R. 2004, å, 420, 937

van der Swaluw, E. 2005, Advances in Space Research, 35, 1123

Volk, K., Kwok, S., & Hrivnak, B. J. 1999, ApJL, 516, L99

Weisberg, J. M., Stanimirović, S., Xilouris, K., Hedden, A., de la Fuente, A., Anderson, S. B., & Jenet, F. A. 2008, ApJ, 674, 286

Werner, M. W., et al. 2004, ApJS, 154, 1

Whiteoak, J. B. Z., & Green, A. J. 1996, A&AS, 118, 329

Wilkin, F. P. 1996, ApJL, 459, L31

Williams, B. J., et al. 2006, ApJL, 652, L33

Williams, B. J., et al. 2008, ApJ, 687, 1054

Willingale, R. et al. 2001, A&A 365, L212

Woltjer, L. 1972, ARA&A, 10, 129

Zhang, K., Jiang, B., & Li, A. 2008, IAU Symposium, 251, 215

Zhang, K., Jiang, B. W., & Li, A. 2009, arXiv:0903.4541

Dear Tea Temim

Thank you very much for your permissions enquiry relating to material published previously in the journals of the American Astronomical Society.

On behalf of AAS, we are pleased to grant the necessary permission for your use of this material and we ask that the Society is acknowledged through the wording: "Reproduced by permission of the AAS". Please could you ensure that the proper bibliographic citation is supplied for each of your papers.

Thank you again for your interest in the AAS journals.

Yours sincerely

Jill Membrey
Managing Editor, Copyright and Permissions

Dr Jill Membrey
Managing Editor, Copyright and Permissions
IOP Publishing
Dirac House, Temple Back,
Bristol BS1 6BE, UK
tel: +44 (0)117 929 7481
fax: +44 (0) 117 920 0814
email: jill.membrey@iop.org
WWW: http://www.iop.org